

Southern Methodist University

SMU Scholar

Mechanical Engineering Research Theses and
Dissertations

Mechanical Engineering

Spring 5-15-2021

Rehology and Electrical Conductivity of Particulate Composites in Additive Manufacturing

Bin Xia

Southern Methodist University, binx@smu.edu

Follow this and additional works at: https://scholar.smu.edu/engineering_mechanical_etds



Part of the [Aerodynamics and Fluid Mechanics Commons](#), [Manufacturing Commons](#), and the [Polymer and Organic Materials Commons](#)

Recommended Citation

Xia, Bin, "Rehology and Electrical Conductivity of Particulate Composites in Additive Manufacturing" (2021). *Mechanical Engineering Research Theses and Dissertations*. 39.

https://scholar.smu.edu/engineering_mechanical_etds/39

This Dissertation is brought to you for free and open access by the Mechanical Engineering at SMU Scholar. It has been accepted for inclusion in Mechanical Engineering Research Theses and Dissertations by an authorized administrator of SMU Scholar. For more information, please visit <http://digitalrepository.smu.edu>.

RHEOLOGY AND ELECTRICAL CONDUCTIVITY OF
PARTICULATE COMPOSITES IN ADDITIVE MANUFACTURING

Approved by:

Prof. Paul Krueger
Professor

Prof. Edmond Richer
Associate Professor

Prof. Peter Raad
Professor

Prof. Xin-Lin Gao
Professor

Prof. David Willis
Associate Professor

RHEOLOGY AND ELECTRICAL CONDUCTIVITY OF
PARTICULATE COMPOSITES IN ADDITIVE MANUFACTURING

A Dissertation Presented to the Graduate Faculty of

Bobby B. Lyle School of Engineering

Southern Methodist University

in

Partial Fulfillment of the Requirements

for the degree of

Doctor of Philosophy

with a

Major in Mechanical Engineering

by

Bin Xia

(B.S., Mechanical Engineering, Dalian University of Technology, 2013)
(M.S., Product Development Engineering, University of Southern California, 2015)

May 15, 2021

Copyright (2021)

Bin Xia

All Rights Reserved

ACKNOWLEDGMENTS

I would like to thank the Department of Mechanical Engineering at Southern Methodist University for their support, the taxpayers, the Moody Dissertation Fellowship, and the National Science Foundation for the National Robotics Initiative Grant No 1317961.

I would like to thank my advisers, especially Dr. Paul S. Kruger, Dr. Edmond Richer, Dr. Xin-Lin Gao, Dr. Peter Raad, and Dr. David Willis.

I would also like to thank the following people who have worked with me on research: Matt Saari, Matthew Galla, Bryan Cox, Daniel Porter, Travis Mayberry, Amir Zamanian, Nicholas Davis, and Adam Cohen.

Bin, Xia

B.S.M.E., Dalian University of Technology, 2013
M.S.P.D.E, University of Southern California, 2015

Rheology and Electrical Conductivity of
Particulate Composites in Additive Manufacturing

Advisor: Professor Paul S. Krueger

Doctor of Philosophy conferred May 15, 2021

Dissertation completed April 28, 2021

Extrusion-based multi-functional additive manufacturing (AM) has been a rapidly developing area in AM recently. Particulate composites are widely used in this area to provide different functionalities with different types of particulate additives. However, there is no systematic understanding of the behavior of particulate composites during extrusion (especially in small nozzles) or of their properties once deposited in the build. This work investigates the properties of the type of particulate composites usually used in additive manufacturing, composed of a polymer matrix material and particulate additives within the micrometer scale. The focus is on the material rheology in the nozzle/capillary (for the particulate suspension in the liquid phase), and its electrical resistivity (at solid phase) when the particles are electrically conductive.

A capillary rheometer with replaceable capillaries of inside diameter (ID) from 0.3302 to 4.572 mm was designed and built to quantify the rheology of materials with different particle sizes (29.9 and 41.9 μm) and volume fractions (10% to 40%). Silicone based material was used as a substitute for melted thermoplastic (as would normally be used for the composite matrix material in AM applications) since both have non-Newtonian shear thinning properties, but the silicone material could be used at room temperature. The experimental measurements for the silicon-particle suspensions showed power law rheological behavior for all suspensions considered. Hence, the flow behavior (n) and consistency (K) indices were used on to describe the materials' rheology.

Particle volume fraction (φ) and the ratio of capillary ID to the particle mean diameter (ω) were found to be the key factors impacting the rheology. The flow behavior index n was found to be only dependent on φ for a suspension with the same suspension fluid and it was modeled as a linear function of φ . The flow consistency index, K , was found to follow similar trends with ω for different φ , with larger φ suspensions showing stronger variations with ω . Based on the K behavior, the rheology was categorized into two regimes: the free flow condition and the particle interaction condition. The value of ω at the boundary between these two conditions was found to decrease with φ . A semi-empirical model of K for the free flow condition was constructed as a function of φ and ω based on a statistical analysis of particle location coupled with the assumption that particles closer to the wall have a stronger influence on the rheology. An model of K for particle interaction condition was also formulated as a function of φ and ω to capture the observed increasing K with decreasing ω . Because of insufficient theoretical foundation and data, the model incorporated an empirical power law behavior to capture the overall trend. Jamming was observed as ω decreased and the ω when jamming occurred was also analyzed and modeled. The influence of particle size distribution was assessed by comparing results for two different particles with different distributions. Particles with a wider size distribution caused a higher K and appeared to have a higher probability of jamming, which was explained by the assumption that larger particles dominate the interactions among particles.

Electrical behavior of composites was investigated using composites made of thermoplastic matrix material and conductive particulate additives. Two matrix materials were used and micrometer-scale silver-coated nickel spheres were used as the particulate additive with particle volume fractions of 20% to 30%. The electrical resistivity of extruded filaments of these materials was investigated under stress relaxation and linear-ramp strain loading conditions. The tested

materials showed stress-strain behavior typical of a Maxwell viscoelastic material. Using the quantum tunneling model to describe conductivity between adjacent particles (which dominate the material resistivity) indicated the composite resistivity was impacted by the matrix material type and the distance between adjacent particles (for a given particle type). Hence, the resistivity was analyzed and modeled by concentrating on these two factors. At a given nominal strain under the same loading conditions, the inter-particle distance was only impacted by particle volume fraction. When mechanical variable loads/strains were applied, resistivity was modeled based on the hypothesis that the change in the mean inter-particle distance was proportional to the cubic root of volume change, which is determined by the strain and Poisson's ratio for the tested material. Different matrix materials were also tested and showed that the resistivity followed the same relationship with particle volume fraction and mechanical load, but with different magnitudes, when different matrix materials were used.

Using the results of this investigation, the manufacturing process of extrusion-based AM can be improved by optimizing the extruder nozzle ID and particulate composite formulation without preliminary tests. Jamming can also be avoided. The composite formulation tuned to achieve the desired electrical behavior with few preliminary tests before utilization in AM and other possible applications.

TABLE OF CONTENTS

LIST OF FIGURES	xi
LIST OF TABLES	xvi
CHAPTER 1 INTRODUCTION AND BACKGROUND	1
1.1 Additive Manufacturing	1
1.2 Particulate Composites and their Application in Additive Manufacturing	3
1.3 Fiber Encapsulation Additive Manufacturing (FEAM).....	5
1.4 Aims and Scope of this Work.....	10
CHAPTER 2 RHEOLOGY OF PARTICULATE COMPOSITES	13
2.1 Current Theories and Models	13
2.2 Rheology Experiment Design and Setup.....	18
2.2.1. Rheometer Design.....	18
2.2.2. Material Selection	24
2.2.3. Experimental procedures.....	27
2.2.4. Testing Conditions	28
2.3 Results	29
2.3.1. Particulate Suspension Rheology General Behavior.....	29
2.3.2. Flow Conditions as a function of ω	31
2.4 Modeling Particulate Suspension Rheology.....	32
2.4.1. Flow Behavior Index (n).....	32

2.4.2.	Conceptual Model for Flow Consistency Index (K)	33
2.4.3.	Model of the Free Flow Condition	39
2.4.4.	Semi-empirical Models for the Particle Interaction Condition	58
2.5	Rheology Conclusion	65
3.	CHAPTER 3 ELECTRICAL RESISTIVITY OF PARTICULATE COMPOSITES	67
3.1	Introduction to Quantum Tunneling Composite.....	67
3.1.1	Uniform junction distance distribution	71
3.1.2	Non-uniform junction distance distribution	75
3.1.3	Empirical models.....	77
3.2	Experiment Design and Setup for Electrical Resistivity Measurements	77
3.2.1	Material Selection and Testing Conditions	77
3.2.2	Experimental Procedure	80
3.2.3	Resistivity Calculation	81
3.3	Electrical Conductivity/Mechanical Experiment Results.....	82
3.4	Electrical Conductivity Data Analysis and Modeling	85
3.4.1	Particle volume fraction and matrix material	85
3.4.2	Influence of Mechanical Loading	88
3.5	Electrical Conductivity Experiment Results.....	94
	CHAPTER 4 SUMMARY AND RECOMMENDATIONS	96
4.1	Conclusion.....	96

4.2	Recommendation and Future Work.....	101
	APPENDIX.....	105
A.1	Steady state, repeatability and accuracy in rheology experiments	105
A.2	Power-law Applicability.....	105
A.3	Determination of rheology constants.....	107
	BIBLIOGRAPHY.....	109

LIST OF FIGURES

Figure 1.1 Prototype FEAM machine (a) and Isometric view of the FEAM kinematic mount and build platform (b).....	5
Figure 1.2 FEAM products: capacitor force sensor (a) and solenoid actuator (b).....	6
Figure 1.3 FEAM wire feeder and cutter: concept design (a) and bottom view (b).....	7
Figure 1.4 Fibers in FEAM: diagram of fiber and extrudate (a) and copper wires printed in the same layer (b).....	7
Figure 1.5 Helical coils printed with continuous fiber on the FEAM printer in round (a) and rectangular (b) geometries.	8
Figure 1.6 Electrical junctions: printed sample (a), inter-layer design diagram (b), and intra-layer design diagram (c).....	9
Figure 1.7 Particulate composites in FEAM: ECPC (a) and SMC (b)	10
Figure 2.1 Schematic diagram of rotational rheometers with the geometries of two plates (a), a cone and a plate (b), and concentric cylinders (c)	19
Figure 2.2 Schematic diagram of capillary rheometer.....	20
Figure 2.3 Rheometer schematic (a) and the actual system (b)	21
Figure 2.4 Schematic diagram (a) and actual parts (b) of the capillaries	23
Figure 2.5 Particles (A3000) under microscope (OLYMPUS BX60F-3 10 × 20) (a) and sphere recognition via MATLAB visualization of particles (b).....	26
Figure 2.6 Particle size distributions for FG 22 (a) and A3000 (b).....	26

Figure 2.7 Flow consistency index K ($\text{Pa}^n \cdot \text{s}$) (a) and flow behavior index n (b) vs. ratio of capillary ID to particle mean size ω (experimental results for Groups 1, 2 and 4)	30
Figure 2.8 Flow consistency index K ($\text{Pa}^n \cdot \text{s}$) (a) and flow behavior index n (b) vs. ratio of capillary ID to particle mean size ω (experimental results for Group 3)	31
Figure 2.9 Flow consistency index K (a) and flow behavior index n (b) vs. ratio of capillary ID to particle mean size ω	31
Figure 2.10 Flow behavior index n vs. particle volume fraction φ (experimental results for Group 1 and 2).	33
Figure 2.11 Categorization of flow conditions based on the hypothetical relationship between ω and K	35
Figure 2.12 Particulate composite made of UV 225-1 and 30% FG 22 under microscope with a 10×4.5 lens before (a) and after UV-light solidification (b)	36
Figure 2.13 Cross sections of micro-CT scans of a particulate suspension ($\omega = 43.01, \varphi = 30\%$) in the axial (a) and radial (b) directions.....	37
Figure 2.14 Average gray scale of all micro-CT scan vs. position in the radial direction inside the particulate composite cylinder sample.....	37
Figure 2.15 Categorization of different flow conditions based on the statistical relationship between K and ω	38
Figure 2.16 Schematic diagram of particulate suspension flow in the capillary for the fully-developed region.....	39
Figure 2.17 Schematic diagram of particles inside (a) and outside (b) the region where the particles may influence the wall shear rate.	41

Figure 2.18 Schematic diagram of the i^{th} wall particle and its geometrical relation with the capillary and impacted area in the axial direction (a) and radial direction (b)	45
Figure 2.19 Schematic diagram of particles randomly distributed in a ring area and dimensions related to different regions that may contain particles.....	47
Figure 2.20 Schematic diagram of particles and their interaction spheres under dense packing .	49
Figure 2.21 ω_{pic} obtained from K ($\text{Pa}^n \cdot \text{s}$) and ω trendlines (when $\varphi = 10\%$ for Group 1 and 2 experiments).....	51
Figure 2.22 ω_{pic} vs. φ for experimental results for Group 1 and 2.....	51
Figure 2.23 Schematic diagram of a wall particle with largest r_{p-p} at $\omega = \omega_{pic}$	52
Figure 2.24 K_{inf} ($\text{Pa}^n \cdot \text{s}$) vs. φ for experimental results for Group 1 and 2.....	53
Figure 2.25 ϵ vs. φ (from experimental results for Group 1 and 2).	55
Figure 2.26 Free flow condition particle volume fraction dependence of G vs. φ (experimental results for Group 1 and 2).....	56
Figure 2.27 Flow consistency index K ($\text{Pa}^n \cdot \text{s}$) vs. ratio of capillary and particle mean radius ω (experimental results for Groups 1 and 2) under the free flow condition.....	57
Figure 2.28 Sketches of possible particle situations not considered in the model: adjacent particles (a), sheltered particles (b), and polydisperse particles (c).....	58
Figure 2.29 Illustration of obtaining approximate ω_{jc} (experimental results for Group 1 and 2)..	59
.....	
Figure 2.30 ω_{jc} vs. φ (experimental results for Group 1 and 2).....	61
Figure 2.31 A ($\text{Pa}^n \cdot \text{s}$) vs. φ (experimental results for Group 1 and 2).....	62
Figure 2.32 Flow consistency index K ($\text{Pa}^n \cdot \text{s}$) vs. ω (experimental results for Group 1 and 2) under the particle interaction condition.	63

Figure 2.33 Flow consistency index K ($\text{Pa}^n \cdot \text{s}$) vs. ω (experimental results for Group 1 and 2) under both flow conditions.	66
Figure 3.1 Schematic diagram of particles in the composite (a) and its resistor model (b).....	68
Figure 3.2 Schematic diagram of quantum tunneling variables for adjacent particles.....	71
Figure 3.3 Schematic diagram of particle and imaginary contacting spheres inside sample	73
Figure 3.4 Schematic diagram of uniform junction distance distribution under tensile loading ..	75
Figure 3.5 Schematic diagram of Relative position of two adjacent particles with tensile loading	76
Figure 3.6 Schematic diagram of standard linear viscoelastic model.....	79
Figure 3.7 Schematic diagram of experimental setup.....	81
Figure 3.8 Sample electrical resistivity ρ vs. particle volume fraction φ at an applied strain of 0.05.....	83
Figure 3.9 Sample strain ε (mm/mm) and stress σ (kPa) (a) and electrical resistivity ρ ($\Omega \cdot \text{cm}$) (b) vs. time t (s).....	84
Figure 3.10 Sample electrical resistivity ρ ($\Omega \cdot \text{cm}$) vs. particle volume fraction φ (T 7718 based ECPC) with applied strain ε	87
Figure 3.11 Schematic diagram of random junction distances without (a) and with (b) tensile loading.....	88
Figure 3.12 Resistivity ρ vs. strain ε and Poisson's ratio μ (a) Resistivity ρ vs. strain ε with Poisson's ratio as a constant (b) and Resistivity ρ vs. Poisson's ratio μ with strain ε as a constant (c)	90
Figure 3.13 stress σ (kPa) vs. strain ε (mm/mm) with linear-ramp strain.....	92
Figure 3.14 Tested/modeled resistivity ρ and strain ε vs. Time t (s)	93

Figure 3.15 Resistivity ρ vs. strain ε when pre-strain was not applied (or too small)..... 94

Figure A.1 Shear stress τ_w vs. shear rate $\dot{\gamma}$ for the experiment of Table A.1..... 107

LIST OF TABLES

Table 2.1 Significant relative viscosity models for particulate suspensions.	14
Table 2.2 Rheometer Capillaries Used (values given in mm)	24
Table 2.3 Rheology Experiment Materials	25
Table 2.4 Particle size distribution summary	26
Table 2.5 Configurations of tested suspensions.....	29
Table 2.6 Approximate ω_{pic} and K_{min} for Group 1 and 2 experiments.....	51
Table 2.7 Approximate K_{inf} for Group 1 and 2 experiments.....	53
Table 2.8 Approximate $\bar{\epsilon}$ vs. φ for experimental results for Group 1 and 2	54
Table 2.9 f_s and G vs. φ for experimental results for Group 1 and 2.....	56
Table 2.10 Semi-empirical values of ω_{jc} (for experimental results for Group 1 and 2)	60
Table 2.11 Semi-empirical values of A (for experimental results for Group 1 and 2)	62
Table 3.1 ECPC material option	78
Table 3.2 ECPC mechanical loading conditions.....	79
Table 3.3 Constant values in Equation 3.25 for different matrix materials	86
Table A.1 Tested and calculated data of experiment example	106

CHAPTER 1 INTRODUCTION AND BACKGROUND

1.1 Additive Manufacturing

Additive manufacturing (AM), colloquially known as 3-D printing, was first invented in 1980's [1]. Ever since then, it has been developing quickly and playing an increasingly vital role in manufacturing technologies [1]. Presently, it is a progressively more popular topic in the media and the public, mainly resulting from three reasons. First, its special features and advantages over traditional manufacturing technologies intrigues the public as well as industry and academia. Second, the main patent for AM has recently expired and companies are flooding into this area resulting in more rapid innovation. Third, due to recent technological developments, many of these methods can be utilized at reasonable costs [2,3].

As its name suggests, AM produces products by adding material(s). In the most prevalent approach, AM builds up parts one layer at a time based on a 3-D model developed in computer aided design software or produced by 3-D scanning. AM can be divided into several types based on how the solid layers are generated. Fused deposition modeling (FDM) extrudes a thermoplastic from a nozzle and deposits it at an elevated temperature, after which it solidifies to form a solid layer. Stereo lithography (SLA) uses a vat of photopolymer resin. A light source (laser) is used to cure selected regions of each layer into a solid so that successive solid layers form the desired shape. Selective laser sintering (SLS) uses metal or ceramic powders to form layers via powder bed fusion, with the fusion accomplished using a laser as a localized heating source. Finally, there is binder jetting, in which the powders are connected by the injected binder to form a layer [2, 3].

Additional methods exist and are being developed, but they generally draw from the foundation laid by those noted here.

Though the layer forming methods are different, the main principle of all AM technologies is the same, decomposing the 3-D object to 2-D layers or paths and building up the layers one on another to attain the final object/component. Based this principle, AM has already made important contributions to manufacturing capabilities in terms of the design, fabrication, and distribution of the manufactured products [3]. Designs previously regarded as impossible or too difficult to manufacture with traditional methods may be readily manufactured by AM. The process planning is simplified as parts can be directly built from the data of the 3-D models. Products including wearable devices and personal medical devices, such as hearing aids, neck braces, etc., may be customized by AM with a lower acceptable price, making mass customization feasible in many cases. Additionally, products demanding high-stability, high-cost, and long-duration transportation can be transported as design data and fabricating material, and then fabricated at the location by AM, which decreases the cost and time, and changes the supply chain.

Benefitting from these advantages, the AM marketplace has already increased from \$3.07 billion in 2013 to \$11.58 billion in 2019. What's more, studies suggest the future revenue will be increased at a compound annual growth rate exceeding 14% from 2020 to 2027 [4, 5, 97]. Some researchers even predict that it is possible that in 2030, the market share of additive manufacturing-produced articles (products, components) versus conventionally produced articles will be significant (10%) across all industries [6].

However, to really achieve the goals of simplifying increasingly complex designs, allowing active component fabrication (instead of passive, static components), and finally reshaping the

manufacturing world, there are still many challenges to overcome [3, 7]. A brief overview of key existing challenges is presented below:

- 1) The competition between printing time and accuracy. The height of one layer in AM has one of the highest impacts on both the accuracy and manufacturing time of the product, namely, decreasing the layer height can improve accuracy, but at the cost of significantly increasing the manufacturing time. No universally applicable solution has been developed for this challenge.
- 2) The limited types of printable materials. The number of materials readily usable in AM is continuously increasing but remains limited. Many functional materials are not available or matured in AM. For example, magnetic and thermo-conductive materials are available in polymer AM, however, their property range is very limited.
- 3) Size limitation. The size range of products fabricated by AM is limited. Although progress is being made, AM of very large or Nano scale products is still an active research area.
- 4) Cost of manufacturing. The costs of products are still higher than those from conventional methods in most areas.
- 5) Software versatility. Working with multiple materials or other non-standard approaches requires flexible software to interface between the design and AM system. Some companies such as Autodesk and Microsoft and some other open source researchers have started to work on this area but the software is not mature.

1.2 Particulate Composites and their Application in Additive Manufacturing

Among the challenges existing in AM, one of the most meaningful is finding the materials to satisfy different functional requirements. For example, for additive manufacturing of electrical systems, electrically conductive materials must be investigated, but they must be produced with dielectric materials to allow for electrical isolation of the conductive pathways. For

electromagnetic actuators, both electrically conductive, and magnetic materials are required. Additionally, biocompatibility of materials is relevant for implantable components and prosthetics. Given the importance of material variety to AM, researchers have investigated different materials to contribute to AM, including metal, ceramic, polymer resins, composite materials, etc. [9]

A popular way to manipulate material properties of common materials is to formulate particulate composites. These composites are made of at least two kinds of materials. One material is used as the binder to provide structural support and the other one or more materials can be used as filler to provide required properties such as electrical conductivity, thermal resistivity, magnetic permeability, etc. The combination of different materials can be used to optimize the properties of the composite and attain the required function, typically with greater ease than inventing a totally new material.

There has been a lot of recent activity with composite materials in AM. For example, Miriyev et al. [13] printed a soft actuator working like natural muscle with stretchable piezo electric composites. Wehner et al. [14] printed a robot octopus with moving limbs made from particulate composites (silicone matrix material with different nanoparticle additives) that were hydraulically controlled by fugitive and catalytic fluids. Sun et al. [15] printed a Li-ion battery. Coronel et al. [16] printed some circuit boards with conductive composites using a system of printing methods integrated with a robot arm. Tibbits et al. [17] printed shape-morphing structures with cellulose composites, which is also described as 4-D printing. Leigh et al. [18] printed the gaming die with an embedded processor and accelerometer. Ding et al. [60] printed multiple 3-D transforming structures with a ferromagnetic material. The LAMRA lab (author's group) at SMU has also printed many items with composite materials in the Fiber Encapsulation Additive Manufacturing (FEAM) Project [19-22], which will be discussed next.

1.3 Fiber Encapsulation Additive Manufacturing (FEAM)

FEAM is a novel AM process that permits the printing of electromechanical and electronic devices within a single affordable machine. To realize the full capabilities of FEAM, three types of materials are necessary in the printing process: matrix materials to provide basic structure and serve as dielectric encapsulation, fibers (a typical copper wire in FEAM) to provide electricity and electrical signal transmission, and functional materials to provide desired functionalities. A prototype FEAM machine to print these types of materials is shown in Figure 1.1. With this approach, some interesting active components have been printed as shown in Figure 1. 2 [18].

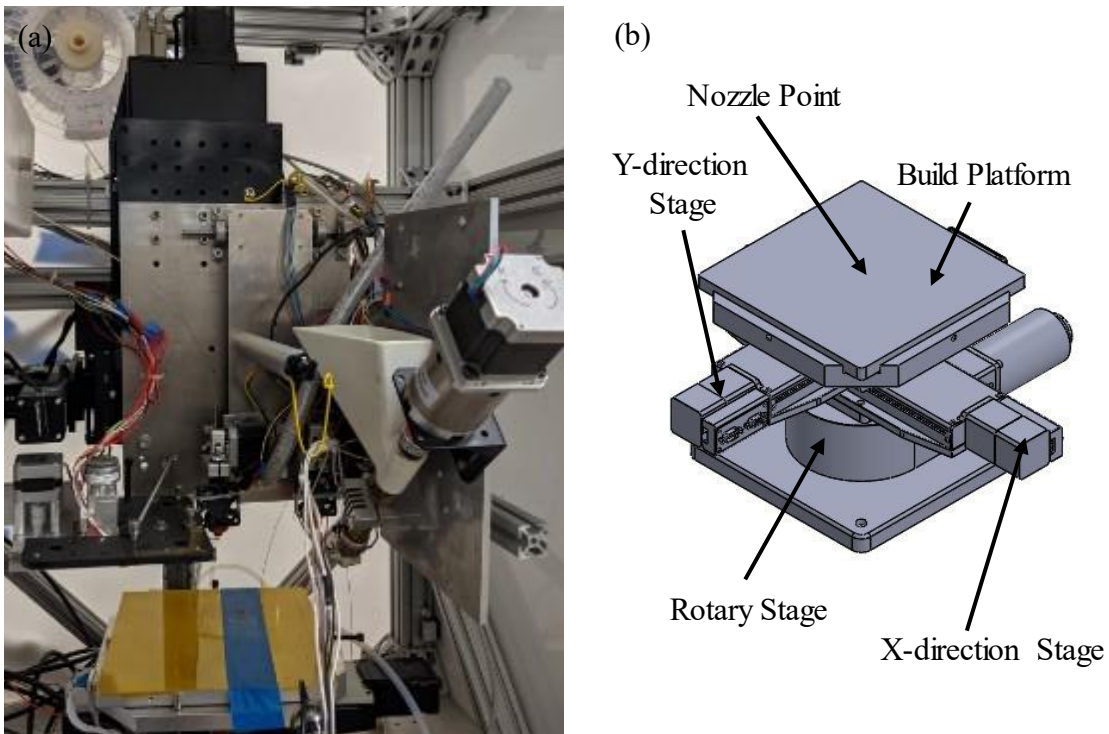


Figure 1.1 Prototype FEAM machine (a) and Isometric view of the FEAM kinematic mount and build platform (b)

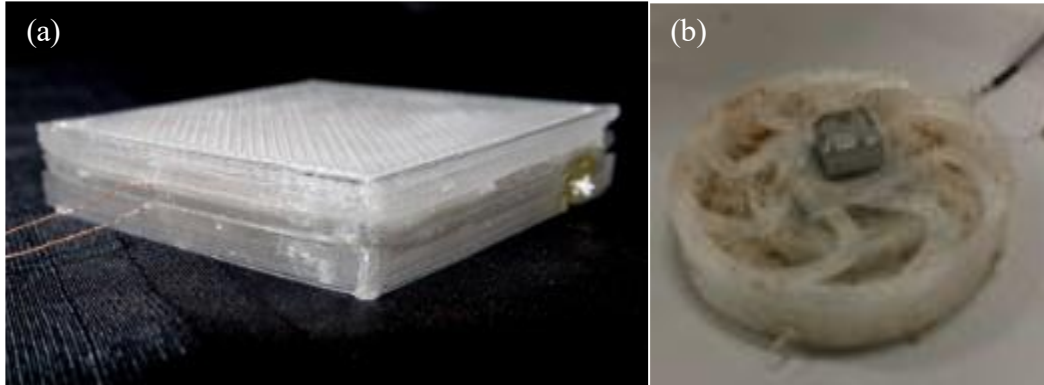


Figure 1.2 FEAM products: capacitor force sensor (a) and solenoid actuator (b)

In FEAM, matrix materials are printed via the traditional FDM method. Hence, materials such as polylactic acid (PLA), polyvinyl ether (PVE), and acrylonitrile butadiene styrene (ABS) can be used as matrix materials. Also, to fabricate some soft components, a special mini-screw extruder [91,92] was developed to print stretchable materials such as thermoplastic elastomer (TPE).

Within the matrix material(s), FEAM enables fibers to be printed simultaneously. A feeder and cutter, as shown in Figure 1.3, are used to achieve this goal. Fiber is fed into the hypodermic tube from a spool using the roller system. The drive roller is driven by a stepper motor. The idler roller is spring-loaded with adjustable tension to prevent the slippage and deformation. A razor blade between two tubes near the end of the feeder and cutter is used to cut the fiber. The cutting is actuated by a solenoid. To position the fiber in the printing part accurately, the sharp angle on the end of the feeder and cutter is used to keep the hypodermic tube in close proximity to the nozzle orifice. Due to the small inner diameter of the hypodermic tubes ($207\ \mu\text{m}$) compared with the fiber diameter ($127\ \mu\text{m}$), a cut wire segment will push the segment in front until it finally exits the final hypodermic tube [20, 93].

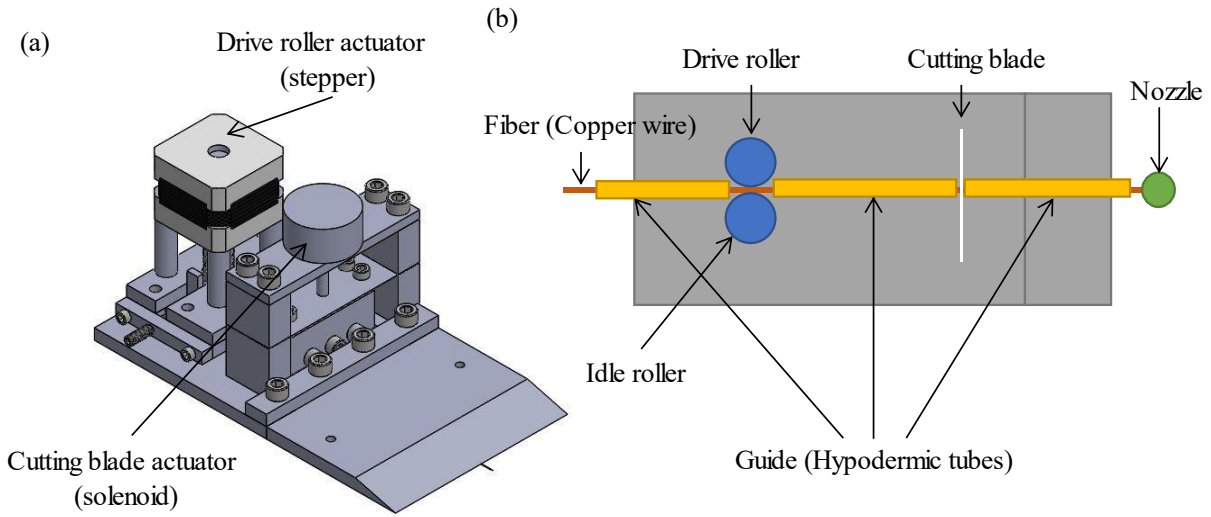


Figure 1.3 FEAM wire feeder and cutter: concept design (a) and bottom view (b)

During the extrusion of the fiber, the extrudate of the matrix material from the nozzle solidifies over the fiber and locks the fiber in place as Figure 1.4. This allows for fiber traces to be insulated and placed in arbitrary directions. To enhance printing speed, compressed air was delivered for cooling and solidifying the matrix material quickly after extrusion.

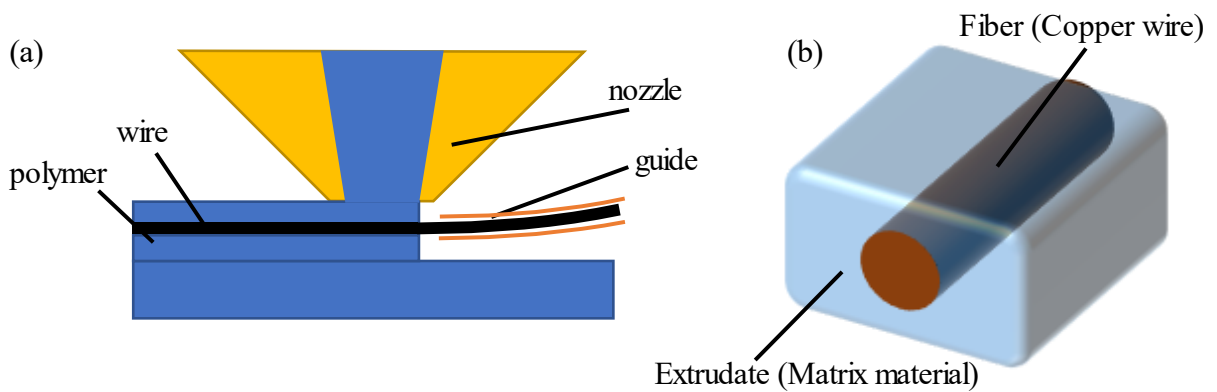


Figure 1.4 Fibers in FEAM: diagram of fiber and extrudate (a) and copper wires printed in the same layer (b)

Additionally, to accurately position the fiber within the extruded material, different open loop control algorithms were compared for a range of printing conditions [93]. Using the FEAM method, a variety of embedded continuous fibers were printed, as shown in Figure 1.5.

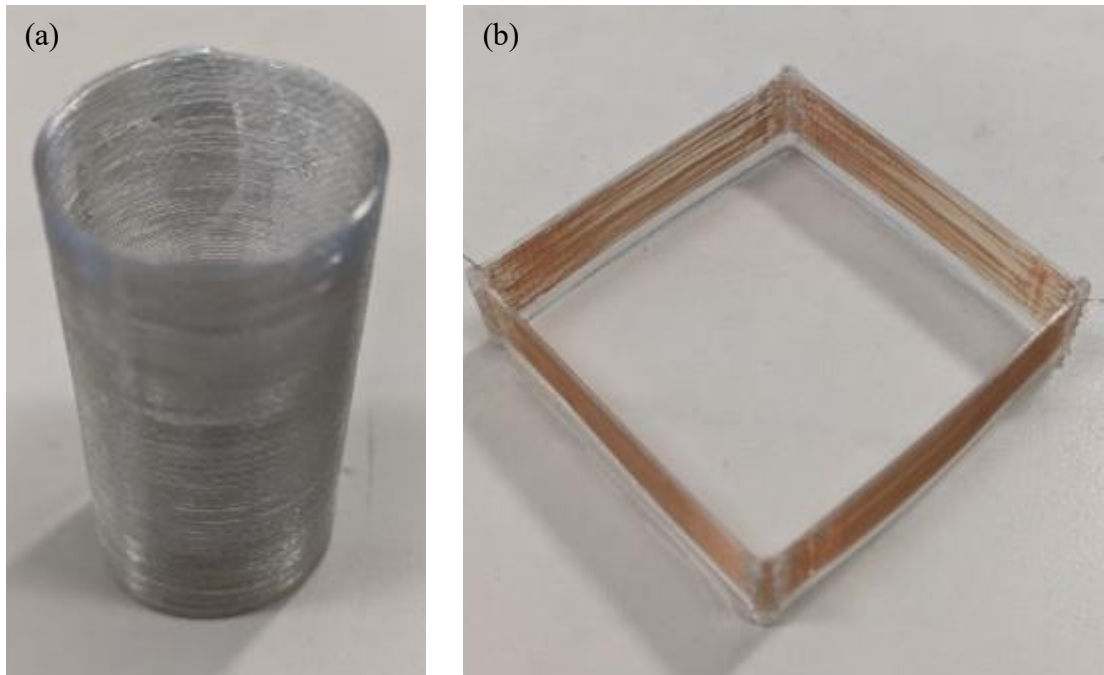


Figure 1.5 Helical coils printed with continuous fiber on the FEAM printer in round (a) and rectangular (b) geometries.

To enable more complex devices and circuits to be fabricated, one of key requirements is creating robust and reliable electrical junctions between encapsulated wires (and electrical components), as shown in Figure 1.6 (a). The wires or the wire and electrical elements to be connected may lie in the same layer or in adjacent layers. Hence, the junctions can be categorized into two types, inter-layer and intra-layer junctions. An inter-layer junction is where wires lie in neighboring layers as shown in Figure 1.6 (b). An intra-layer junction is one in which two or more wires lie in the same layer as shown in Figure 1.6 (c).

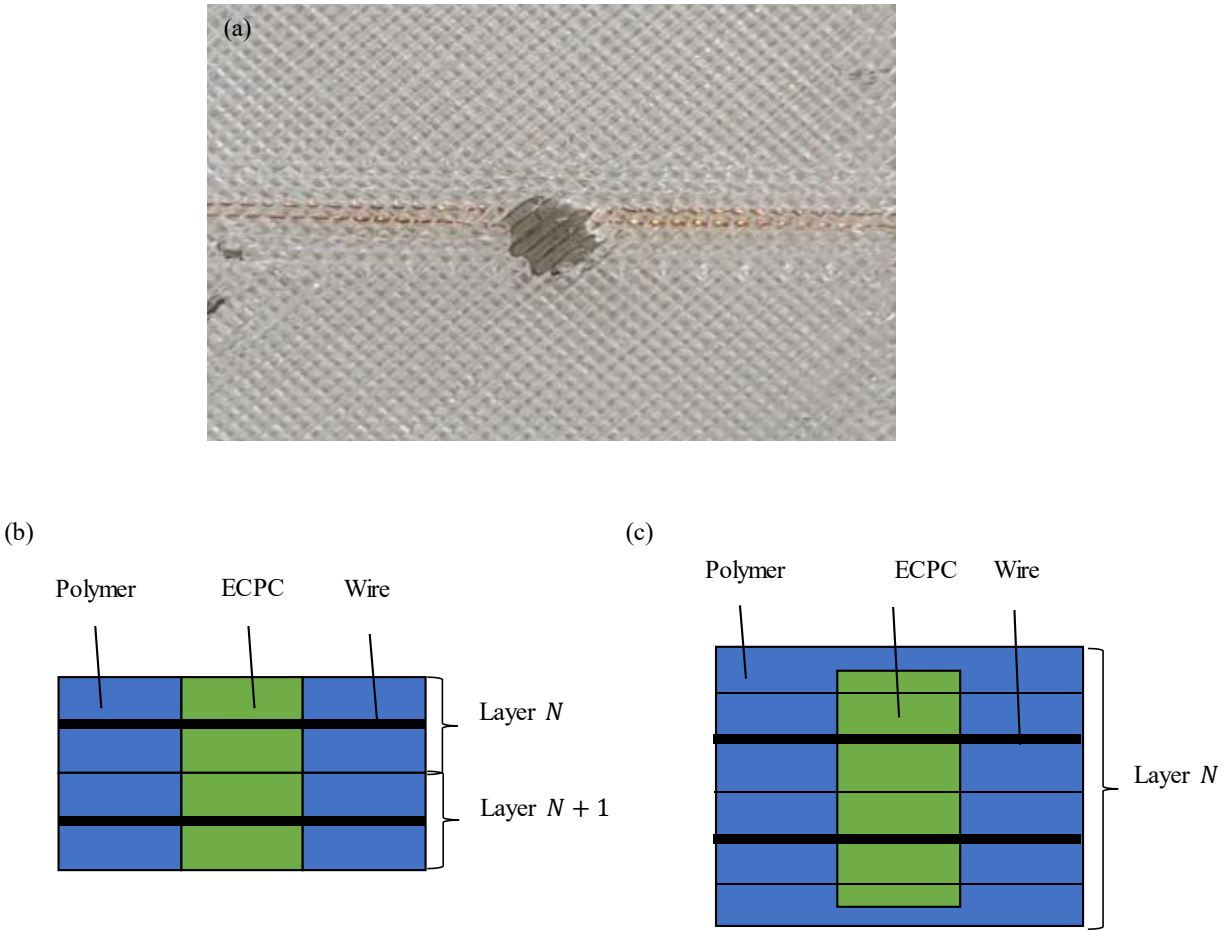


Figure 1.6 Electrical junctions: printed sample (a), inter-layer design diagram (b), and intra-layer design diagram (c)

Several different types of materials for creating junctions were tested and analyzed, including solder, solder paste, and different kinds of custom-formulated electrically conductive polymer composite (ECPC, a type of particulate composite), illustrated in Figure 1.7 (a) [22]. ECPC formulated using TPE, hot glue, and hard wax binder materials were investigated and compared. The electrical resistivity of ECPC varied dramatically with different particle volume fraction, with resistivity dropping rapidly beyond a specific volume fraction corresponding to the percolation

threshold. Some theories and models based on quantum tunneling impacts have been proposed to describe and explain the conductive behavior. Variable electrical resistivity was also observed under mechanical loading (details are presented in section 3.1).

Another goal of FEAM is to print reliable actuators. To achieve this, custom-formulated soft magnetic composite (SMC, a type of particulate composite) as shown in Figure 1.7 (b) was created with iron particles and wax to provide magnetic permeability.



Figure 1.7 Particulate composites in FEAM: ECPC (a) and SMC (b)

1.4 Aims and Scope of this Work

During development of methods for printing ECPC and SMC with FEAM, a range of interesting behaviors were revealed during extrusion:

- 1) The behavior of the material extrusion varied dramatically when the material type or the volume fraction of the materials varied;

- 2) Separation of the matrix and powder material occurred during extrusion under some processing conditions;
- 3) Strong variation of the required properties with different volume fraction of particles;
- 4) The extruder could be blocked and the device might be damaged when some combination of composites were used at some extrusion speeds.

Looking deeper into these behaviors and the available literature, it was apparent that particulate composites are mostly tested by direct experiments, and extruded based on experience. Little theoretical or systematic research has been done on the behavior of the composite flow inside the extruder (details are presented in section 2.1), indicating that further understanding of this process would be valuable for effective utilization of ECPC and SCM in AM.

Concerning the electrical properties, unstable/variable electrical conductivity was discovered for the parts printed with ECPC. Following some initial tests with ECPC it was found that, besides the impact of particle volume fraction, similarities between resistivity and strain, stress, and rate of strain were also observed when the ECPC was subjected to dynamic loading conditions. The behavior could not be fully explained based on available models. Some models even give a trend opposite to the test results (details are presented in section 3.1). Circuits and electronic components may be damaged if the electrical power is chosen and applied from the inaccurate models and reliability is also a concern. Alternatively, the dynamic material variations can allow the material to be used as a sensor if the relation between the electrical conductivity and dynamic motion are modeled accurately. Hence, further investigation of the electrical conductivity of ECPC under different dynamic conditions is warranted.

In summary, the purpose of the work is to investigate the physics of particulate composite flow in a nozzle and assess the quality of the resulting particulate composites with regard to electrical

properties and their relationship with mechanical behavior. Using this background, the printing process for particulate composites can be better optimized to avoid defects such as clogging and the part quality and properties can be better controlled to satisfy the design requirements.

In this work, the investigation of particulate composite flow rheology is presented in Chapter 2. Current theories and models in related areas are presented in section 2.1. Design and setup of the experiments to mimic and investigate the working conditions of AM are presented in section 2.2. Experimental results are presented in section 2.3. Parameters impacting the rheology are analyzed in section 2.4. Models are also discussed and presented in this section. Based on those work, a conclusion of the rheology of the type of material is presented in section 2.5.

The investigation of ECPC electrical conductivity is presented in Chapter 3. Background and introduction of materials similar to ECPC are presented in section 3.1. Design and setup of the experiments to investigate ECPC electrical conductivity on different static/dynamic conditions are presented in section 3.2. Experimental results are presented in section 3.3. Parameters impacting the electrical conductivity are analyzed in section 3.4. Models are also discussed and presented in this section. Conclusions regarding the behavior of the electrical conductivity of ECPC is presented in section 3.5.

An overall conclusion and assessment of future work of both the material rheology and electrical conductivity is presented in Chapter 4. The applications of the models in AM and other possible use scenarios are also discussed and presented.

Experimental data and related calculations are also provided in the appendices.

CHAPTER 2 RHEOLOGY OF PARTICULATE COMPOSITES

An essential element of particulate composites for additive manufacturing is their flow behavior (rheology), as this directly impacts the printing process as well as the solidification and the final part quality. Once the particulate composite rheology is understood and can be tailored/controlled, the other aspects can be more easily controlled and optimized.

Flow of polymers such as thermoplastic melts and resins are generally non-Newtonian. The rheology of the pure non-Newtonian flow (without particles) is mainly influenced by the type of material, shear rate, and temperature. When particles are added, the situation is even more complex. The new factors may include particle mean size and size distribution, particle volume fraction, and particle shape. Additionally, for extrusion processes the nozzle/capillary ID also has an impact on the apparent rheology as particles can induce dramatic resistance (e.g., jamming) as tube diameter decreases.

To assess the impact of particles on rheology in particle laden flows of non-Newtonian fluids, the present chapter reviews existing models for particle laden Newtonian fluids and experiments with non-Newtonian particle laden fluids are presented and discussed.

2.1 Current Theories and Models

Though particulate composites have been utilized in AM for many years without thorough investigation (as described in Chapter 1.2), related investigations for particle laden flows and suspensions in Newtonian fluids have been conducted for over 100 years as flow properties of suspensions are also an important topic in chemical reactions, the mining industry, and slurry transport [27, 101, 102, 103, 104]. Those investigations considered many factors including different types of particles and a range of Reynolds' number. Though the applications are generally

different, there are still many similarities between the existing investigations and this work. It is worthwhile to review the existing theories and models.

Available literature [such as 24-39] presents hundreds of equations trying to express relative viscosity of different types of suspensions in Newtonian fluids. Most of them are focused on the impact of particle volume fraction, with different kinds of considerations and limitations. To simplify the discussion, the equations are categorized into four types of equations and combinations of these based on their functional form(s): linear models, polynomial models, power law models, and exponential models. Several representative models are listed in Table 2.1 and discussed as examples below. In Table 2.1, φ is the volume fraction, d and d_{mol} are the particle and molecule diameters, L_{char} is the characteristic length of the system such as tube diameter for a pipe flow ($d_{mol} \ll d \ll L_{char}$).

Table 2.1 Significant relative viscosity models for particulate suspensions.

Author(s)/Time	Type	Equation
Einstein [24] 1906	linear	$\mu = \mu_0(1 + 2.5\varphi)$
Jeffrey [25] 1922	linear	$\mu = \mu_0(1 + A\varphi)$
Guth, Eugene, & Simha [26] 1936	polynomial	$\mu = \mu_0(1 + 2.5\varphi + 14.1\varphi^2)$
Vand [27] 1948	exponential	$\mu = \mu_0 \exp\left(\frac{2.5\varphi + 2.7\varphi^2}{1 - 0.609\varphi}\right)$
Mooney [28] 1951	exponential	$\mu = \mu_0 \exp\left(\frac{2.5\varphi}{1 + k\varphi}\right)$
Simha [29] 1952	polynomial	$\mu = \mu_0(1 + 1.5\varphi(1 + (1 + (25\varphi/4f^3) \dots)))$
Brinkman [30] 1952	power law	$\mu = \mu_0 \frac{1}{(1 - \varphi)^{[\mu]}}$
Krieger & Dougherty [31] 1959	power law	$\mu = \mu_0 \frac{1}{\left(1 - \frac{\varphi}{\varphi_M}\right)^{[\mu]\varphi_M}}$

Ford [32] 1960	polynomial	$\mu = \mu_0(1 + 2.5\varphi + 11\varphi^5 - 11.5\varphi^7)$
Thomas [33] 1965	mixed	$\mu = \mu_0(1 + 2.5\varphi + 10.5\varphi^2 + 0.00273\exp(16.6\varphi))$
Bournonville & Nzihou [37] 2002	power law	$\mu = \mu_0 \left[1 + \frac{D}{\dot{\gamma}^E} \frac{\frac{\varphi_v}{\varphi_M}}{\left(1 - \frac{\varphi}{\varphi_M}\right)} \right]^G$
Snapati [38] 2009	power law	$\mu = \mu_0 \frac{10C_U}{d_{50}} \left[1 + \frac{[\mu]}{\dot{\gamma}^{0.4}} \left(\frac{\varphi}{\varphi_m - \varphi} \right) \right]^{3.5}$
Blissett [39] 2013	mixed	$\mu = \mu_0 \left(1 - \frac{\varphi}{\varphi_M} \right)^{-[\mu]\varphi_M} + m(\varphi)\gamma^{n(\varphi)-1}$

The first relative viscosity equation was developed by Einstein in 1906 [24] and has a linear dependence on the particle volume fraction. The linear equation only considers the no-slip boundary condition over the particle sphere in purely laminar flow and the allowable particle size and volume fraction range are very limited. Building on this result, Jeffrey considered the shape of the particles, including a variable multiplier A that is 2.5 when the particles are spherical (to match Einstein's result) and increases to as large as 10 when the particles are more ellipsoidal [25]. To increase the accuracy of these models, researchers utilized three methods: adding polynomial terms, changing the model into exponential functions, or using power law functions.

Considering polynomial expressions, in 1936 Guth, Eugene, and Simha [26] increased the polynomial order to second-order allowing for an increased range of applicability up to $\varphi = 0.2$. The coefficient of the second-order term, 14.1, was determined from a method of successive reflection, which assumes that the disturbance of flow around a first sphere is compensated by an additional flow around a second sphere in order to fulfill the continuity equation and nonslip boundary condition at the sphere's surface.. Simha [29] increased the accuracy further in 1952 by including more terms and adding the semi-empirical parameter f to fit dilute suspensions. Ford

[32] worked on low/moderate concentration suspensions and increased the accuracy to the seventh order in 1960.

Taking a different approach, in 1948 Vand [27] derived an exponential function from the Navier-Stokes' equations considering the effect of adding an incremental volume fraction of spheres, $d\phi$, and accounting for the interactions of particles using the same method of successive reflection as Guth, Eugene, and Simha [26]. In 1951, Mooney [28] developed a similar model by considering two successive additions of monodisperse spheres to a pure fluid, accounting for possible hydrodynamic interactions and the mutual crowding effects of the two sphere populations on each other with an experimentally attained parameter k ("crowding factor") where $1.35 < k < 1.91$.

In 1952, Brinkman [30] developed a power law model for relative viscosity, however, the original model is limited to the special case of infinite polydispersity (meaning the maximum particle volume fraction, ϕ_M , is equal to 1). Krieger & Dougherty [31] improved this model by considering the maximum fraction of the particles by introducing Mooney's concept of "crowding factor". In 1984, Wildemuth [36] introduced a parameter considering shear rate dependent maximum volume fraction. (When the particles are not spherical, the particle orientation is impacted by the shear, resulting in a different maximum volume fraction.) In 2002, Bournonville & Nzihou [37] introduced three adjustable parameters to allow for the applicability at very high ($\sim 10^6 s^{-1}$) and low ($\sim 0.01 s^{-1}$) shear rate. In 2009, Snapati [38] introduced two adjustable parameters considering the effects of median particle size and particle size distribution.

In addition, some researchers tried to use mixed expressions to determine the relative viscosity. Thomas [33] introduced an empirical exponential term to a second-order polynomial model to fit the tested data. However, no theoretical explanations were provided for the exponential term, and

the model still has a 13% error when the particle volume fraction is 0.5. Blissett [39] introduced two adjustable parameters to allow for a wider range for φ (from 0.1 to 0.7) and shear rate (from 2 to 200 s^{-1}). However, the two adjustable parameters are correlated with four other suspension dependent constants that must be obtained through curve fitting.

All models described in Table 2.1 are based on suspensions in Newtonian fluids, which means the adjustable parameters are determined by the particles. However, when the fluid used in the suspension is non-Newtonian, the relative viscosity can be affected by both the fluid properties and the particles and these may interact with each other. The coupled factors can make the viscosity model more complex.

There are some investigations on polymer melt (shear thinning) suspensions [40-45]. Kataoka, Kitano, Sasahara, & Nishijima [42-44] applied Mooney's model to polymer melt suspensions to calculate relative viscosity of the suspension and suspension fluid under the same shear stress and improved it with another adjustable parameter to apply to polymer melts containing a suspension of short fibers [45]. The applicable range of φ in their model was limited (only $\varphi = 10\%$ was investigated). The model was compared with data obtained using a rotational rheometer, which made it unreliable (as will be discussed in Section 2.2.1).

The models of suspensions in both Newtonian and non-Newtonian fluids relate that with higher particle volume fraction, the materials change from a fluid-like to a solid-like state, which is a phase change called the jamming transition. Because of the similarities between the jamming transition and the glass transition, a model has been formulated based on the schematic model of glass transition [87]. Also, microfluidic rheology and viscoplasticity have been utilized to analyze the material behavior near the jamming transition [83, 84].

However, much of the work on jamming behavior has a narrow focus such as the point where jamming occurs [75], and how to jam and unjam using vibratory excitation [76]. Many other significant factors in the target application of additive manufacturing (AM), including the effects of capillary inner diameter (ID), particle size and size distribution on jamming, and the flow behavior before jamming were not investigated. Additionally, most of the work utilizes shear thickening material [75-78]. However, most of the materials used in AM are shear thinning.

Given the lack of detailed models for rheology of particulate suspensions in non-Newtonian fluids and of information about the approach to the jamming transition in shear-thinning fluids, the present investigation focuses on these aspects of particulate suspensions in non-Newtonian fluids.

2.2 Rheology Experiment Design and Setup

To quantify the impact of particle and fluid properties on the particulate suspension rheology experimentally, it is essential to test the suspension rheology when different combinations of fluid and particles are utilized. To this end, an appropriate rheometer and materials must be selected.

2.2.1. Rheometer Design

Two types of rheometers commonly utilized in scientific and industrial analyses are the rotational and capillary rheometers. A rotational rheometer is usually made up of two plates, or other similar geometries such as a cone and a plate or concentric cylinders as Figure 2.1. Sample materials are loaded inside the geometries between the spinning and fixed elements. A torque is applied to the spinning component to generate a rotational shear stress on the material. Resulting shear rate is measured. Based on the shear rate and shear stress, the rheology can be determined.

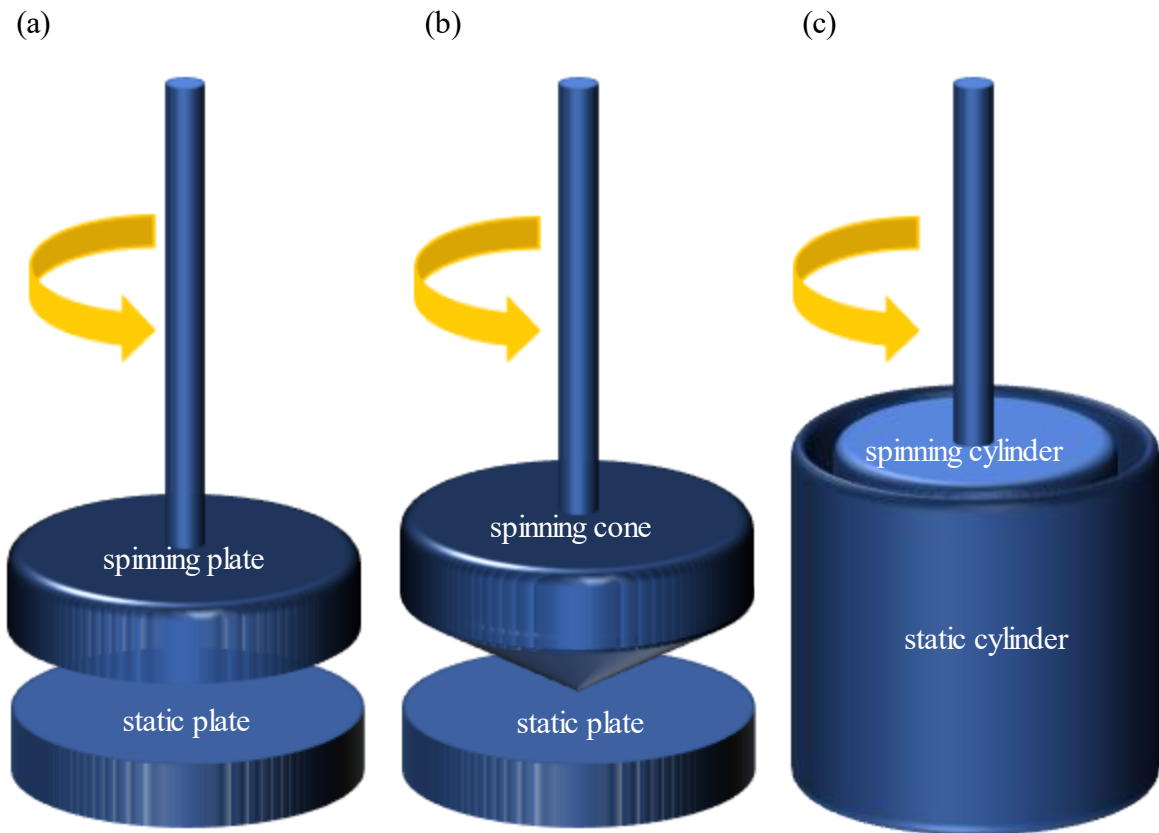


Figure 2.1 Schematic diagram of rotational rheometers with the geometries of two plates (a), a cone and a plate (b), and concentric cylinders (c)

A capillary rheometer is made up of a capillary tube or pipe of well-defined dimensions as in Figure 2.2. Materials are extruded through the tube under pressure. When the material flow rate is controlled, the pressure drop across the tube is measured. With enough different flow rates and pressure drops, shear stresses and shear rates can be calculated numerically, and the rheology can be determined.

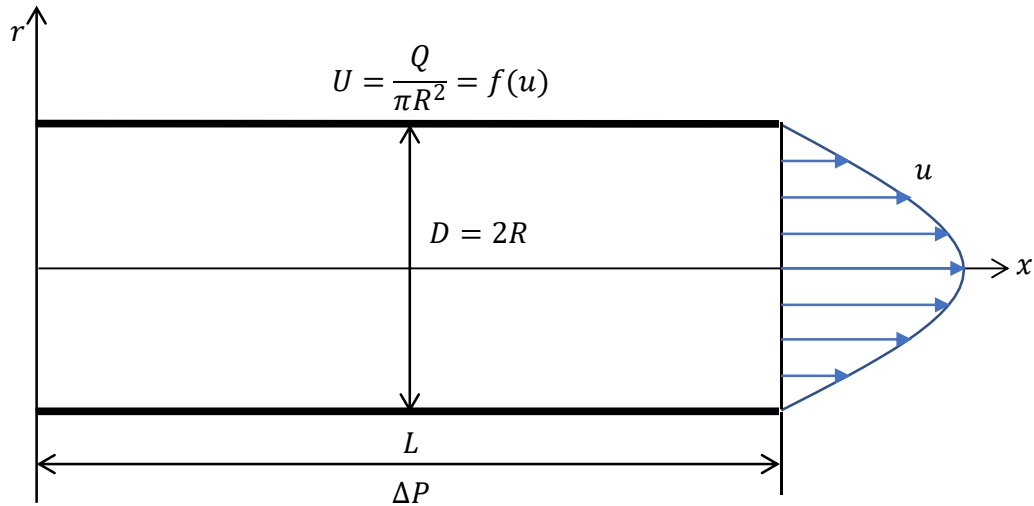


Figure 2.2 Schematic diagram of capillary rheometer

Rotational rheometers are sophisticated and capable measurement systems. They can provide large shear rate/stress test ranges, direct shear measurements, and provide measurements for a range of shear rates and temperatures (when heating is applied) very rapidly. Nevertheless, a rotational rheometer is not appropriate for the present investigation and a capillary rheometer is used. There are several reasons for this choice.

First, the materials to be measured are particulate suspensions. If rotational movement is applied, the centrifugal effects can displace the particles radially. Thus, the particle volume fraction will be different at different positions within the measurement system and the measured results would not represent the desired particulate suspension.

Second, in additive manufacturing the material is extruded through small-diameter nozzles. Especially with particles of diameter similar to the nozzle size, the nozzle size may impact the

flow behavior. Using capillaries of sufficiently small inner diameter (ID) can mimic the conditions of additive manufacturing and help quantify the impact of nozzle diameter on printing behavior.

To investigate capillary ID (D , as shown in Figure 2.2) effects, it is necessary for the capillary of the rheometer to be replaceable. However, rheometers currently in the market do not meet this requirement, especially when D is required to be around 1 mm or smaller to mimic the additive manufacturing process. Hence, a rheometer with replaceable capillaries was designed and built. A schematic and photo of the rheometer is shown in Figure 2.3.

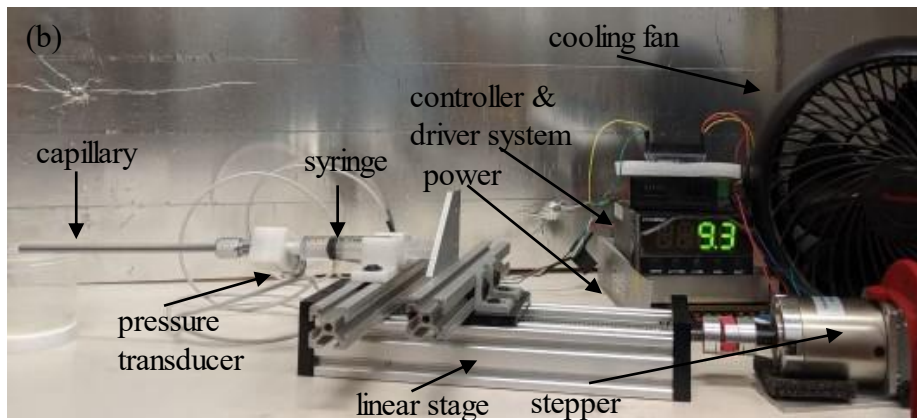
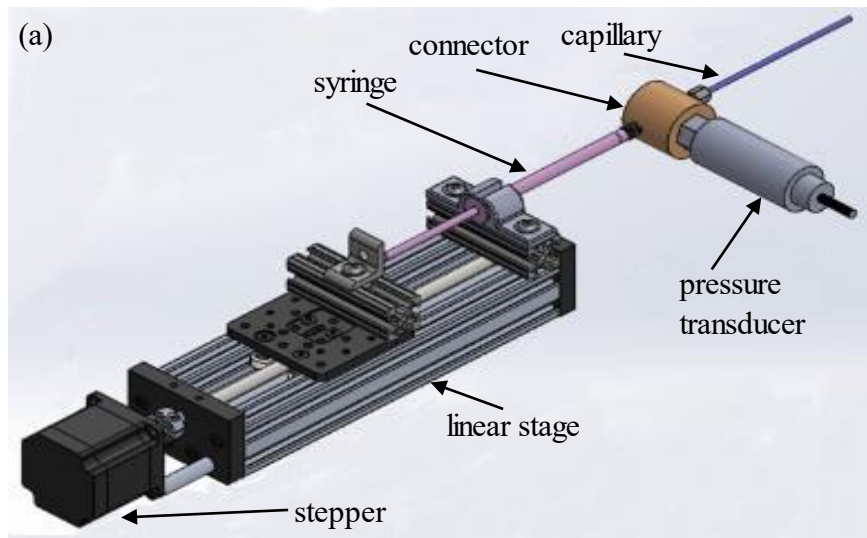


Figure 2.3 Rheometer schematic (a) and the actual system (b)

In the designed testing system, a motorized linear stage (OpenBuild C-Beam® Linear Actuator Bundle and NEMA 23HS22-2804S-PG47 Stepper) with multiple syringes of 1 mL to 60 mL capacity were used to drive the flow. The capillaries were steel needles or seamless tubes with different lengths and D as shown in **Error! Reference source not found.**.2. Pressure transducers (PX61V1-1KGI and PX61v1-100GI) were used to measure the inlet pressure to the capillaries. Multiple connection and support parts were also used to build the rheometer.

During a test, the stepper motor actuated the linear stage (connected to the syringe plunger) to set the flow rate of the suspension through the capillary. Once the fluid arrived at steady state, the inlet pressure to the capillary was collected from pressure transducer. (The flow exited the capillary as a free jet.) Using the pressure data at different flow rates and the capillary dimensions, the rheology on different shear rates was determined using standard methods [88]. Details of the calculation method are discussed in Section 2.2.3.

In the experiments, it was found that the contraction at the entrance of the capillary and fluid developing region impacted the measured pressure drop along the capillary significantly. To account for the inlet effect, capillaries with the D and different lengths were used as Figure 2.4. With the same flow rate Q , the pressure drops ΔP_1 and ΔP_2 were measured when capillaries with two lengths L_1 and L_2 were used. Then pressure drop ΔP in the fully developed region L was obtained from their difference, where $\Delta P = \Delta P_1 - \Delta P_2$, and $L = L_1 - L_2$.

Based on the capillary dimensions, preliminary tests, and computational results for non-Newtonian pipe flow [105], the entrance length for the flows considered ($\frac{L_{entr}}{D} \leq 0.64$) was less than L_2 . Hence, all the flow in the region L can be considered fully-developed. To simplify the

discussion, all the results in the later sections are the pressure drop ΔP in the fully-developed region L .

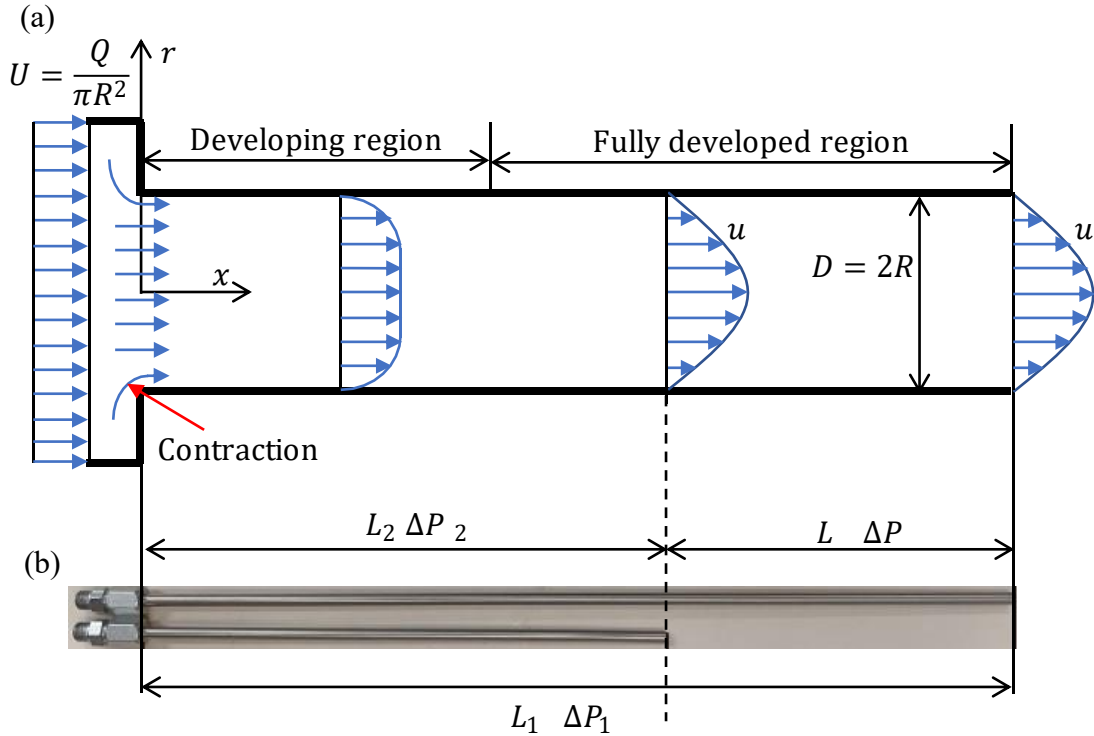


Figure 2.4 Schematic diagram (a) and actual parts (b) of the capillaries with length L_1 and L_2

In FEAM, the nozzle ID is typically in the range of 0.5 mm to 2 mm with particle mean diameter (d) in the range of 0.010 mm to 0.325 mm. To mimic the flow behavior and collect enough data to investigate the impact of $\omega \equiv D/d$ (the ratio of capillary ID to particle mean size), capillaries were selected as shown in Table 2.2 and particles were selected as given in Table 2.3 (b) (details are presented in Section 2.2.2) based on preliminary tests.

Table 2.2 Rheometer Capillaries Used (values given in mm)¹

D	0.3302	0.4064	0.6096	0.8382	1.36	1.73	2.01	3.05	3.861	4.572
L₁	50.8	50.8	101.6	101.6	217	214.5	263	357	499	595.5
L₂	28.57	34.22	54.15	57.79	175	124	214.5	176	298.5	334.5
L	22.23	16.58	47.45	43.81	42	90.5	48.5	181	200.5	261

2.2.2. Material Selection

In FEAM, the printing material is a mixture of metal powders and thermoplastic polymer. However, since the rheology of the particulate composite flow is dependent only on the physical properties (there is no chemical reaction), different materials can be used in this investigation. Because high temperatures are required to extrude thermoplastic polymers and the rheometer developed for this investigation didn't have the capability to accommodate such temperatures, a shear thinning silicone polymer was used as the base material in the composite blends instead of polymer melts. To investigate the impact of the suspension fluid type, a Newtonian fluid was also tested for comparison purposes. Details for the suspension fluids are provided in Table 2.3 (a).

Two types of glass beads (Table 2.3 (b)) were used in this investigation instead of metal particles used in typical ECPC. This approach was for convenience by lowering the cost and allowing testing of a broader range of parameters. To check the particles used in ECPC have the same impact on the suspension rheology, the metal particles used in ECPC (Table 2.3 (b)) was also used for limited number of tests.

¹ Capillary IDs are from the manufacturer datasheets except for 1.36, 1.73, and 2.01 mm, which are measured with a digital caliper (Mitutoyo 500-197-30) as the values from the datasheet were inaccurate.

Table 2.3 Rheology Experiment Materials

(a) Suspension fluids
Newtonian: 95% ADM corn syrup 42/43 and 5% water mixer (volume fraction), referred to as “ADM” throughout
Non-Newtonian: Momentive UV-Electro 225-1 Base, referred to as “UV 225-1” throughout

(b) Particle
Spheriglass® Solid Glass Microspheres A3000, referred to as “A3000” throughout
Fibre Glast Microspheres 22, referred to as “FG22” throughout
Potters Industry silver coated nickel SN08S40 (particle mean size $d = 10.00 \mu\text{m}$), referred to as “SN08S40” throughout

As particle mean size is a significant factor impacting the composites’ rheology, the mean sizes of both types of glass beads were measured. Particles were imaged with a microscope (OLYMPUS BX60F-3 10 × 20), collecting 10 images of groups for each type of particle. A sample image is shown in Figure 2.5 (a). Particles in the pictures were visualized and identified with MATLAB as shown in Figure 2.5 (b). Over 2000 particles of each type were identified. Their size distributions were also obtained in this process. The results are summarized in Table 2.4 and Figure 2.6. According to the image results, the Spheriglass® Solid Glass Microspheres A3000 have a wider size distribution than the Fibre Glast Microspheres 22. Given the significant difference between the manufacturer reported mean particle diameters and the measured particle diameters (Table 2.4), the measured particle diameters will be used in the measurements and data analyses in the following.

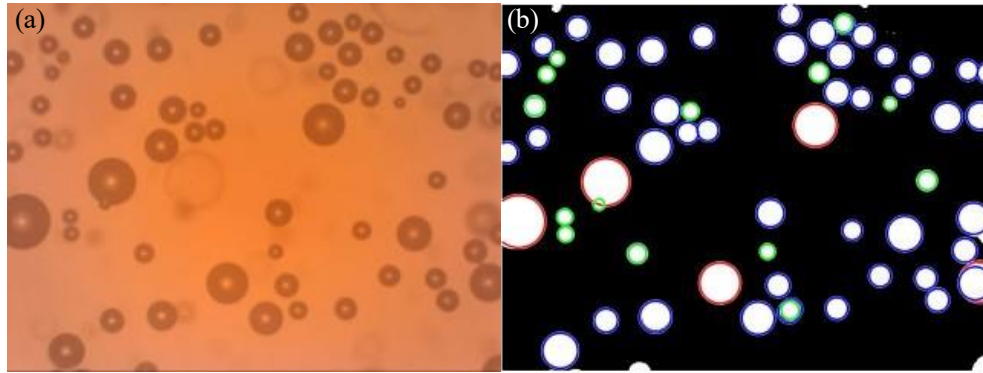


Figure 2.5 Particles (A3000) under microscope (OLYMPUS BX60F-3 10 × 20) (a) and sphere recognition via MATLAB visualization of particles (b)

Table 2.4 Particle size distribution summary

Particle type	FG 22	A3000
Mean size from datasheet (μm)	70	35
Measured mean size (μm)	41.9	29.9
Measured max size (μm)	127.3	53.1
Measured min size (μm)	5.4	2.3
Particle count	2219	2272

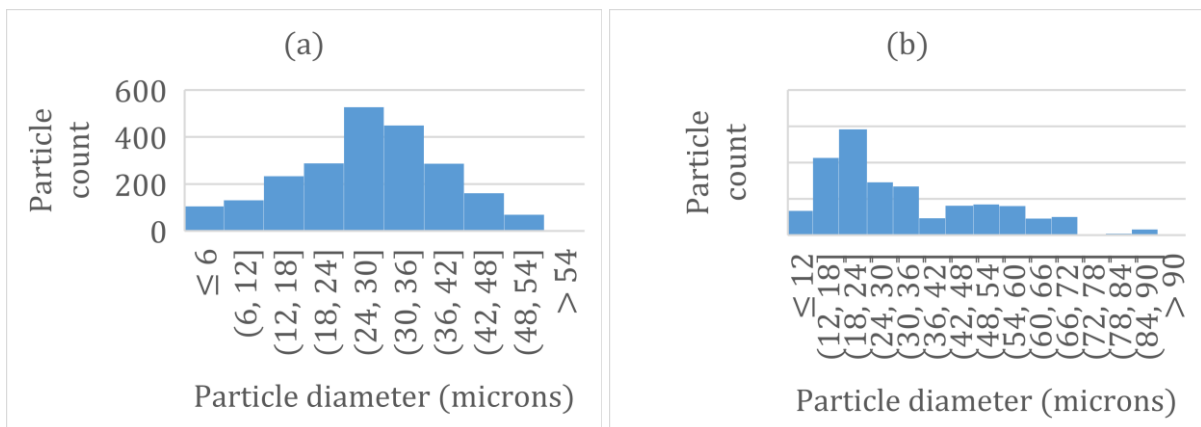


Figure 2.6 Particle size distributions for FG 22 (a) and A3000 (b)

2.2.3. Experimental procedures

The rheology measurements utilized the following test procedure:

Material preparation. Particulate suspensions utilized here are classified according to the type of particle, suspension fluid, and the particle volume fraction. To prepare a suspension, a scale (Cole-Parmer Symmetry UX-20000-34) was used to measure the weight of the particles and suspension fluid. The required weight of each component was calculated according to their density and required particle volume fraction (accuracy within 0.5%). To make the particles uniformly distributed in the suspension fluid and eliminate the air bubbles, a Flacktek Speedmixer DAC 150.1 FVZ-K was used to mix the suspension for around 5 minutes at a speed of 3000 rpm.

Measurements for one test of a suspension. Testing a suspension with a capillary of the same D is defined as one test. In one test, five different flow rates were applied, the applied flow rates were offset by a factor of two in sequence to facilitate later calculations. The shear rate range was controlled to be in the range 0.5 to 50 s^{-1} by adjusting the flow rates. The average inlet pressure was collected when the flow arrived at steady state. Pressures for capillaries with two different lengths were used to find ΔP for a test as described in Section 2.2.1. Five tests of the same type were repeated on the same suspension. Averages of the pressure drops at each flow rate were used to evaluate the rheology. Examples of the accuracy and repeatability of results are illustrated in Appendix A.1.

Calculate the rheology of the materials. With different flow rates, the wall shear stress τ_w , wall shear rate $\frac{du}{dr_w}$, and viscosity μ can be calculated from the following four equations [12]:

$$\tau_w = \frac{R}{2L} \Delta P \quad (2.1)$$

$$n = \frac{d\left(\ln\left(\frac{Q}{\pi R^3}\right)\right)}{d(\ln(\tau_w))} \quad (2.2)$$

$$\frac{du}{dr_w} = \frac{4Q}{\pi R^3} \left(\frac{1}{4}n + \frac{3}{4}\right) \quad (2.3)$$

$$\mu = \frac{\tau_w}{\frac{du}{dr_w}} \quad (2.4)$$

For the suspensions tested, it was found that n in Equation (2.2) was constant for the same suspension in a capillary with the same D and could be determined by a linear fit of $\ln\left(\frac{Q}{\pi R^3}\right)$ vs $\ln(\tau_w)$. This is illustrated for a typical experiment in Appendix A.2. Thus, it can be concluded the suspensions follow a power law in which the shear stress can be described as

$$\tau = K\dot{\gamma}^n. \quad (2.5)$$

Here, K is the flow consistency index and n is the flow behavior index. These two parameters are used to characterize the suspension rheology in the later chapters. For a power-law fluid, the Reynolds number can be computed as [29]

$$Re = \frac{2^{7-3n}}{\pi^{2-n}} \left(\frac{n}{3n+1}\right)^n \frac{Q^{2-n} D^{3n-4} \rho}{K}. \quad (2.6)$$

Among all the experiments, the maximum Reynolds number was determined to be 0.0061, so the flows were all laminar.

2.2.4. Testing Conditions

Using the rheometer and materials discussed above, rheology was collected for a range of suspensions and flow conditions. To quantify the impact of factors including particle volume fraction and $\omega = D/d$, experiments were conducted with the conditions listed in Table 2.5 Group 1 to 3. Here not all the capillaries were used to test all the materials. However, enough capillary

IDs were used to quantify effects of interest. Details are presented in Section 2.3. As the cost of SN08S40 is expensive, this material was only tested with the selected particle volume fraction and capillaries listed in Table 2.5 Group 4. Matrix material UV 225-1 was also measured with the system, which gave the results $K = 93 \text{ Pa}^n \cdot \text{s}$ and $n = 0.816 [-]$.

Table 2.5 Configurations of tested suspensions.

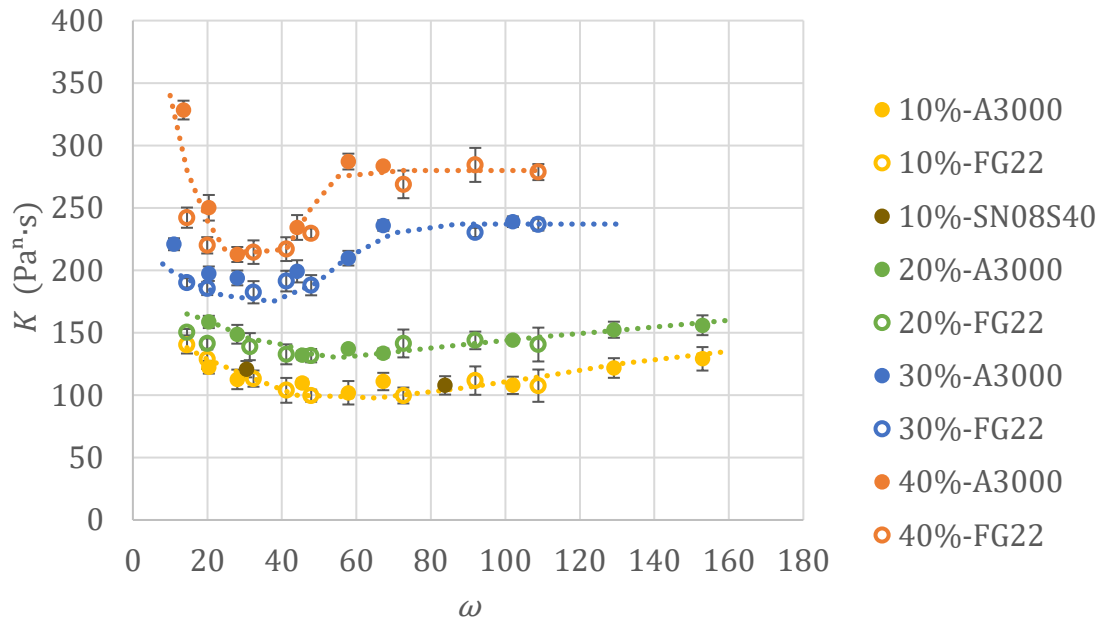
Group Number	Suspension Fluid	Particle Type	Nominal Particle Volume Fraction (%)			
			10	20	30	40
Group 1	UV 225-1	A3000	10	20	30	40
Group 2	UV 225-1	FG22	10	20	30	40
Group 3	ADM	FG22	30			
Group 4	UV 225-1	SN08S40	10 (capillaries with $D = 0.3302$ and 0.8382 mm)			

2.3 Results

2.3.1. Particulate Suspension Rheology General Behavior

Based on the experiments described in Section 2.2, the flow consistency index K and flow behavior index n were obtained for the suspensions listed in Table 2.5. Results for both flow indices are shown in Figures 2.7 and 2.8. Suspensions with different formulations are indicated by symbols with different colors and shapes. Working conditions ($\omega = \frac{R}{r} = \frac{D}{d}$) are shown on the abscissa. The error bars represent the standard deviation of the results over the five tests at each condition. The example of calculations is presented in Appendix A.3. One key phenomenon is the data from Group 4 (brown symbols in Figure 2.7) matches the data for Group 1 and 2 for $\varphi = 10\%$. The results for the glass spheres do not appear to be significantly different from the results for the silver coated nickel spheres.

(a)



(b)

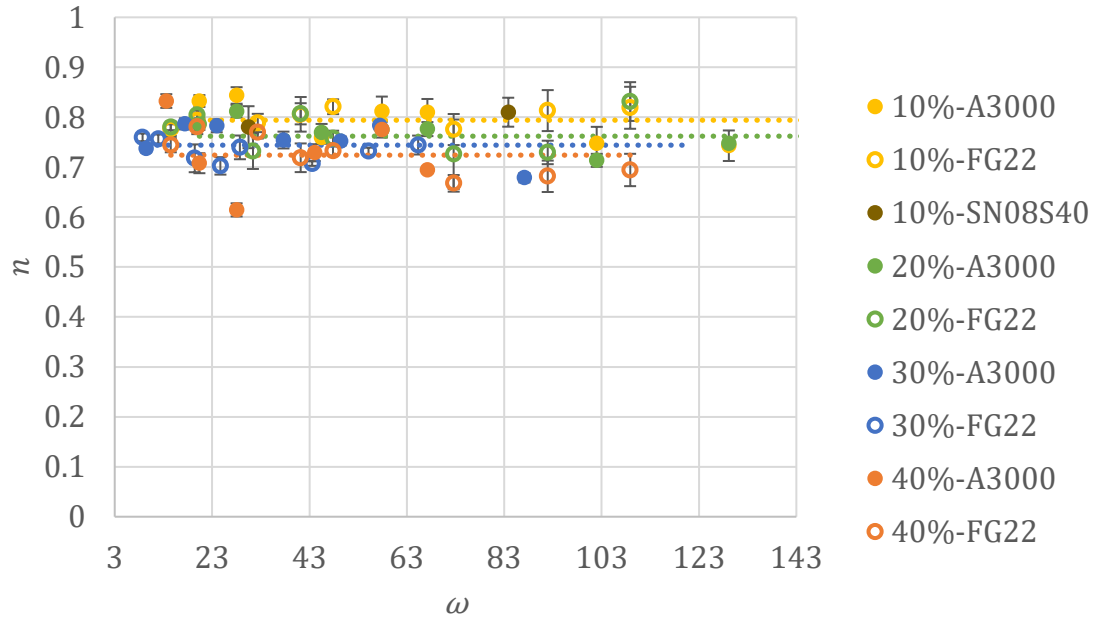


Figure 2.7 Flow consistency index K ($\text{Pa}^n \cdot \text{s}$) (a) and flow behavior index n (b) vs. ratio of capillary ID to particle mean size ω (experimental results for Groups 1, 2 and 4) with legend indications following the format: particle volume fraction – particle type

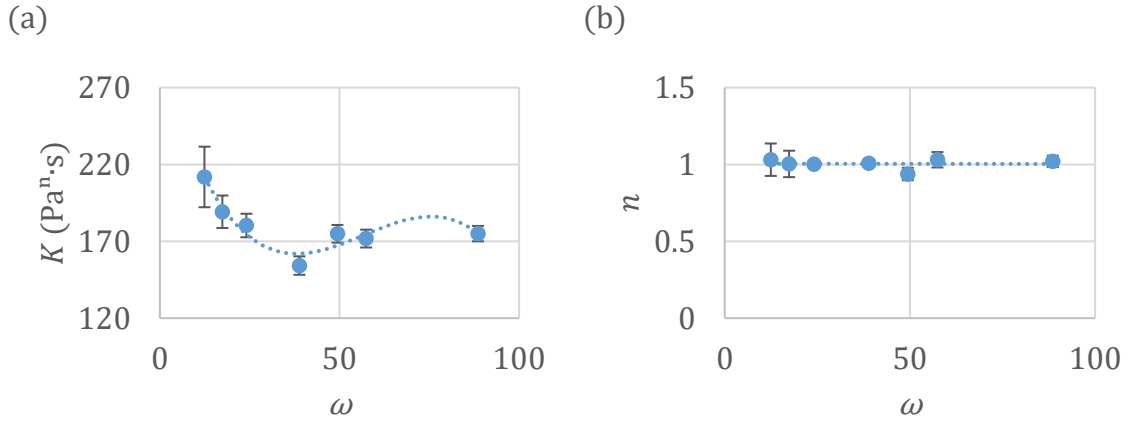


Figure 2.8 Flow consistency index K ($\text{Pa}^n \cdot \text{s}$) (a) and flow behavior index n (b) vs. ratio of capillary ID to particle mean size ω (experimental results for Group 3)

2.3.2. Flow Conditions as a function of ω

In Figure 2.7 and 2.8, a similar shape for the trend lines (dash lines) is observed for all cases tested. A schematic illustration of the generic behavior is shown in Figure 2.9. The trend line shape stays the same with varied particle volume fraction, suspension fluid, and particle size, but seems to be shifted and scaled depending on particle type and volume fraction.

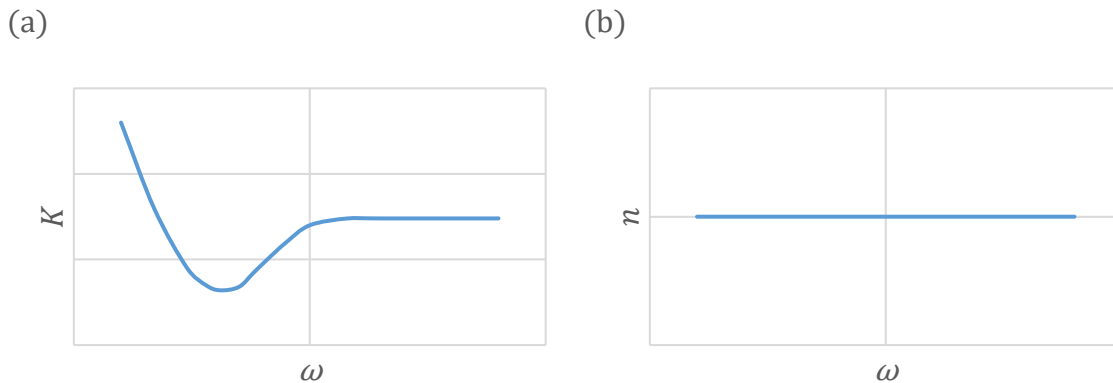


Figure 2.9 Flow consistency index K (a) and flow behavior index n (b) vs. ratio of capillary ID to particle mean size ω

The flow consistency index shows a strong dependence on ω , while the flow behavior index appears independent of this parameter. Generally, the flow consistency index shows three trends: approximately constant, decreasing, and increasing. Additionally, when the ratio is small enough, the capillary will be blocked by the particles, and the flow consistency index rapidly increases toward infinity. The physical reasons for these behaviors and the factors causing the trend lines to shift and scale are proposed and explored in the remainder of this chapter.

2.4 Modeling Particulate Suspension Rheology

Excluding jamming, the particulate suspension flow in the capillary maintains the same particle volume fraction and the suspension flows consistently. Thus, it is reasonable to conclude the particles inside the fluid will move with the same velocity as the fluid. The different flow behaviors prior to jamming can then be related to the different particle distributions for different φ and ω .

2.4.1. Flow Behavior Index (n)

As discussed in Section 2.3.2, ω has minimal effect on the flow behavior index n . The results in Figure 2.10 show that n is a function only of the particle volume fraction φ and decreases with φ increasing. On the other hand, $n = 1$ for the particulate suspension with a Newtonian suspension fluid, regardless of φ (Figure 2.8(b)). This is also the case for all the relative viscosity models in Table 2.1 and the fluid itself. A model for the flow behavior index of the particulate suspension is described as

$$n = n_f(1 + a\varphi) \tag{2.7}$$

where n_f is the flow behavior index of the suspension fluid and a is an adjustable parameter. For the Group 1 and 2 experiments, a least square fit of Equation (2.7) to the results gives $a = -0.23 \pm 0.01$. The results of this fit are shown in Figure 2.10 as the dotted line. For a Newtonian fluid, $a = 0$, and in general, a may depend on the suspension fluid.

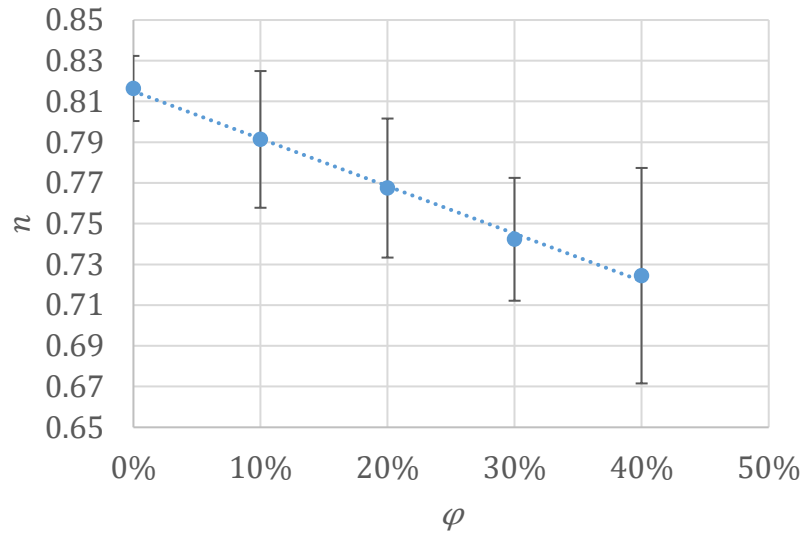


Figure 2.10 Flow behavior index n vs. particle volume fraction ϕ (experimental results for Group 1 and 2). Error bars represent the standard deviations of all n for each ϕ and the dotted line is the least squares fit of Equation (2.7) to the data.

2.4.2. Conceptual Model for Flow Consistency Index (K)

Earlier work by the author [90] described the observed behavior for K in terms of the interaction between the capillary wall and particles and the interaction between the particles themselves as illustrated in Figure 2.11. Four flow regimes were hypothesized and described as follows.

When ω is larger than a specific value, ω_{ffc} , there is enough space between particles or particles and the capillary wall, that the particles have minimal interaction with their surroundings and the suspension is in a free flow condition (“ffc”). Thus, K is constant with minimal impact from the capillary tube.

When ω is between ω_{pic} and ω_{ffc} , interaction occurs between the particles and the wall. Since the wall is fixed, a key effect of the wall is to push particles away from it so that collisions with the wall tend to push particles into the center of the capillary. As a result, there is a higher concentration of suspension fluid near the wall, which tends to lower shear stress and the flow consistency index. In this ω range, the results suggest a smaller ω tends to strengthen the particle centering effect, resulting in a reduced flow consistency index. This condition is called the particle & wall interaction condition.

When ω is between ω_{jc} (“jc” for jamming condition) and ω_{pic} (“pic” for particle interaction condition), there is not enough space for the particles to go smoothly through the capillaries. With smaller ω , there is less channel space available relative to the particle size and it is easier for the particles to interfere with each other, which results in a larger flow consistency index. This is called the particle interaction condition.

When ω is around ω_{jc} or smaller, particles begin to cluster and span the entire capillary. Then it is impossible to move the flow with the original pressure. The particles become fixed in place (the capillary becomes “blocked” with “jammed” particles) and no longer move with the fluid.

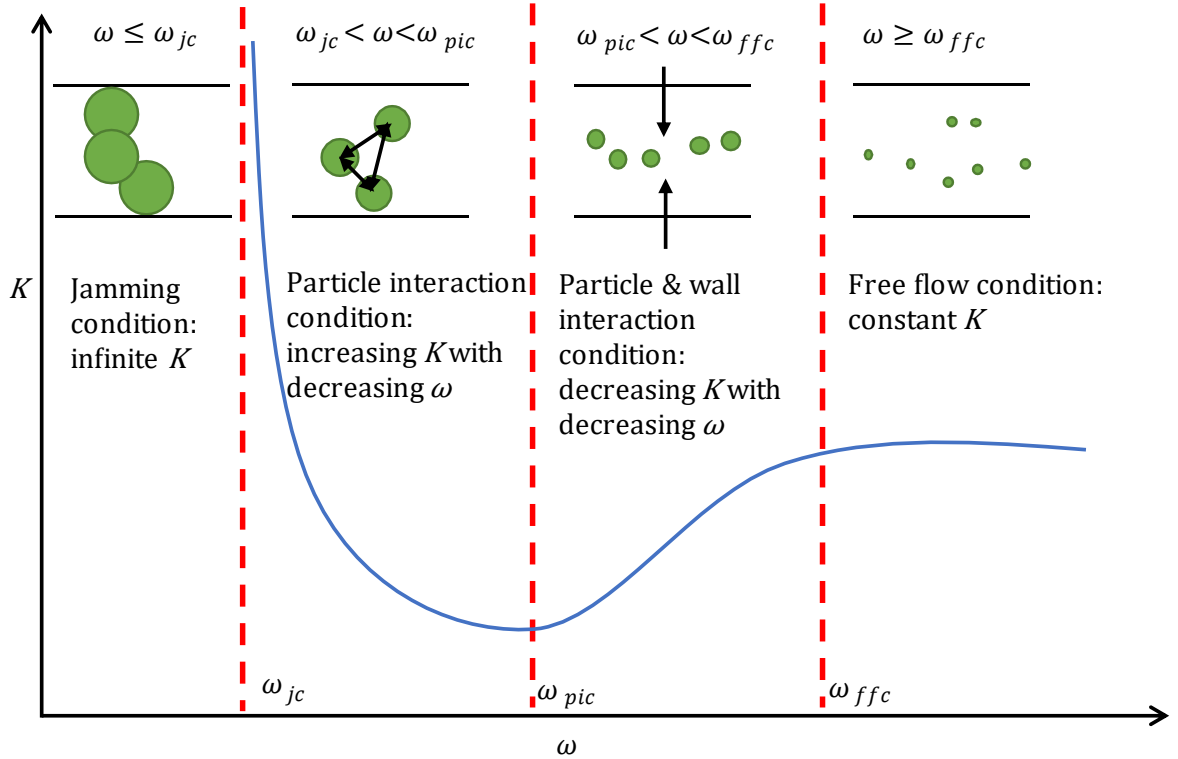


Figure 2.11 Categorization of flow conditions based on the hypothetical relationship between ω and K

To validate the hypothesis regarding particle distribution (in relation to the particle and wall interaction condition), some particle distributions inside the capillary for suspensions at the particle and wall interaction condition ($\omega = 43.01$, $\phi = 30\%$, see Figure 2.7) were visualized via a micro-CT (SkyScan 1172 high-resolution desktop scanner at a resolution of $2.00 \mu\text{m}$). The sample was fabricated by extruding the suspension (with the addition of a curing agent) into transparent tubing and then curing the silicone polymer with a UV light to create a solid sample that could be further analyzed. There is minimal force generated during solidification so the particles can be

regarded as staying at the same position. Figure 2.12 shows microscope images before and after solidification indicating the same overall structure before and after.

Example cross-sections in both the radial and axial directions obtained from the micro-CT scans are shown in Figure 2.13. The darker holes are the particles, and the lighter regions are the silicone (fluid when it is a particulate suspension before solidification). Hence, the radial particle density distribution can be obtained by calculating the average of gray scale of the sample at different radial positions for all axial cross sections. The result for this sample is shown in Figure 2.14, which shows no dependence of the particle distribution on radial position within the measurement tolerance. Hence, it can be concluded that the particles are uniformly distributed inside the capillary for the particle and wall interaction condition, instead of having a higher probability distribution away from the wall as posited in prior work [90].

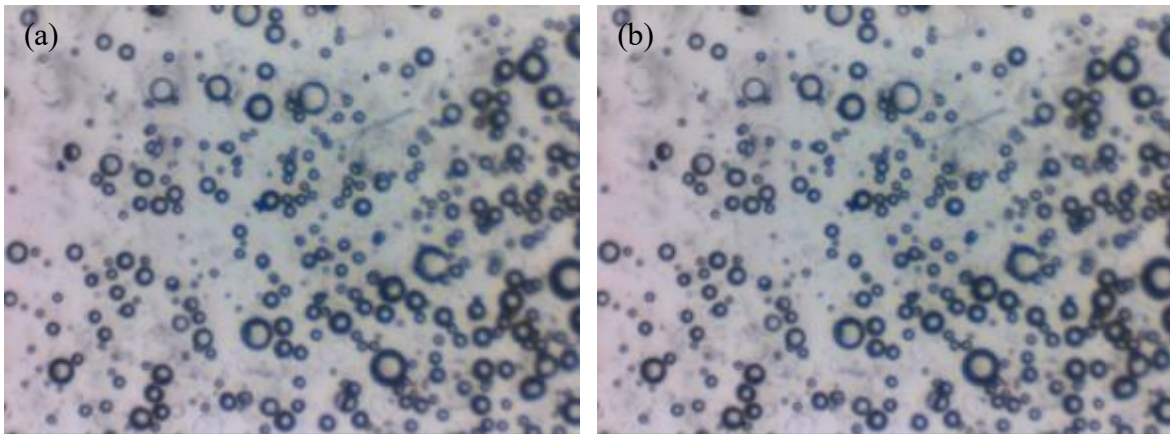


Figure 2.12 Particulate composite made of UV 225-1 and 30% FG 22 under microscope with a 10×4.5 lens before (a) and after UV-light solidification (b)

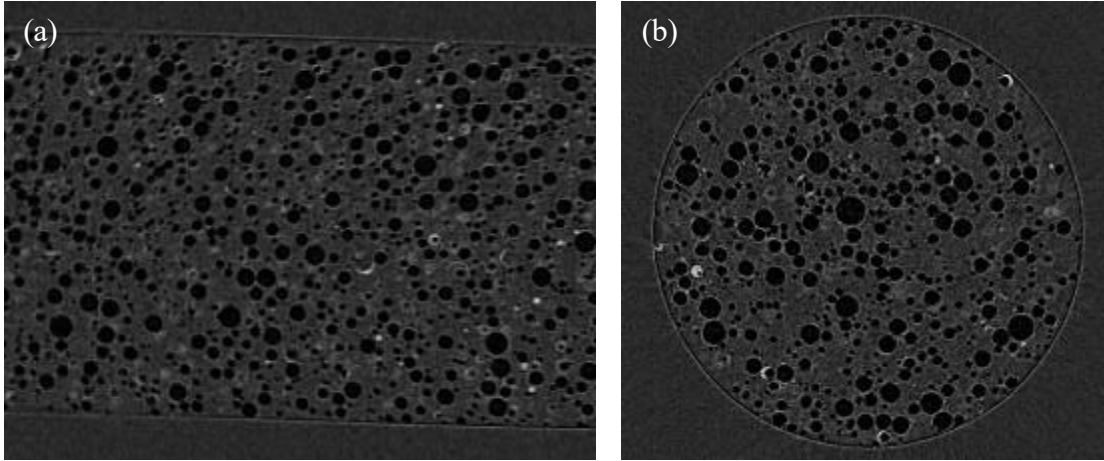


Figure 2.13 Cross sections of micro-CT scans of a particulate suspension ($\omega = 43.01, \phi = 30\%$) in the axial (a) and radial (b) directions.

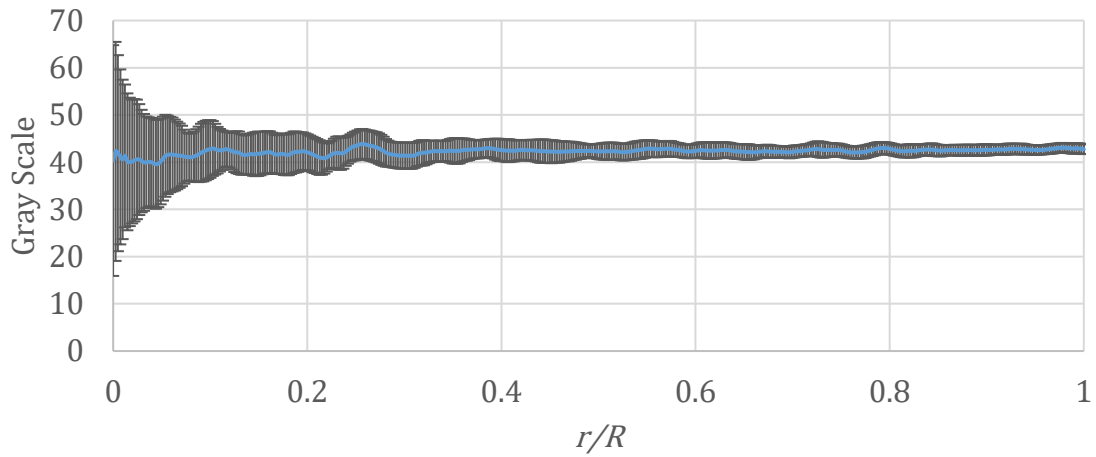


Figure 2.14 Average gray scale of all micro-CT scan vs. position in the radial direction inside the particulate composite cylinder sample shown in Figure 2.13 (error bars represent the standard deviation of the gray scale tested at different positions with the same radius).

To explain the flow behavior for a uniform particle distribution at large ω , analyses are conducted to demonstrate how the decreasing ω results in initially constant and then decreasing K

before $\omega = \omega_{pic}$. Considering jamming happens at the end of the particle interaction region and jamming results from the interaction among contacting particles, the jamming condition can be regarded as part of the particle interaction condition. According to this new perspective, the flow conditions are recategorized into two types: the free flow condition characterized by minimal particle interaction (constant and decreasing K with decreasing ω), and the particle interaction condition characterized by non-negligible particle interaction (increasing K with decreasing ω) that is bounded by particle jamming as $\omega \rightarrow \omega_{jc}$, as illustrated in Figure 2.15. That is, the particle and wall interaction condition is eliminated and merged with the free-flow condition, and the jamming condition is merged with the particle interaction condition. The details discussing the mechanisms of each region and how the suspension parameters impact K are presented in separate sections below.

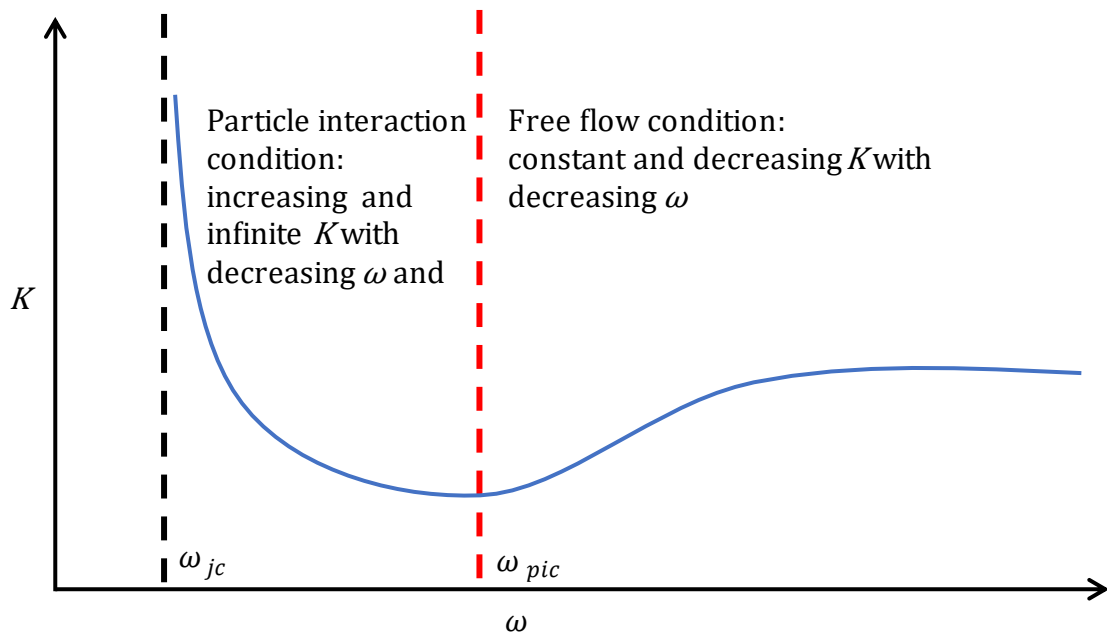


Figure 2.15 Categorization of different flow conditions based on the statistical relationship between K and ω

2.4.3. Model of the Free Flow Condition

Following the preceding discussion, the particulate suspension can be regarded as homogenous flow before jamming as illustrated in Figure 2.16 for the fully-developed region. For these conditions, the flow behavior can be described by

$$\tau_w = K\dot{\gamma}_w^n \quad (2.8)$$

$$F = \tau_w A_c = K\dot{\gamma}_w^n A_c \quad (2.9)$$

where τ_w and $\dot{\gamma}$ are the shear stress and shear rate caused in the flow at the capillary wall; K and n are the particulate suspension consistency and behavior indexes, respectively; F is the total shear force caused by the shear stress on the capillary wall; and A_c , is the surface area.

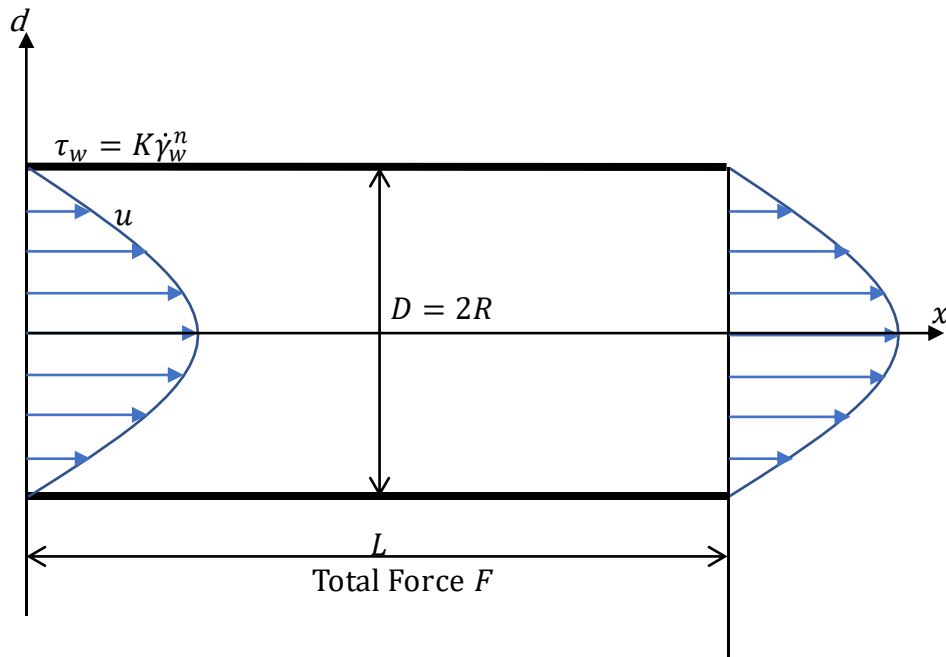


Figure 2.16 Schematic diagram of particulate suspension flow in the capillary for the fully-developed region.

The total shear force is the result of the contributions from the individual suspension components. Specifically, particles near the capillary wall influence the fluid flow near the wall by diverting flow between the wall and the particles. Conversely, in regions where particles are further away from the wall, the force can be described by the effect of the fluid without considering the presence of particles. This is illustrated in Figure 2.17.

The total flow is the combination of the effects from regions (A_i) where particles are influencing the flow near the wall and the rest of the capillary wall region where the fluid flow effects dominate. Hence, the total force on the capillary wall can also be obtained as

$$F = \sum F_{im} + F_{un} \quad (2.10)$$

where F_{im} are the wall forces generated under the influence of particles near the wall and F_{un} are the forces generated without particle influence.

To describe the characteristics of wall flow with particle influence and without, the distance between the particle and the centerline of the capillary is defined as q . The radius of the inner boundary of the region where the particles may influence the wall shear rate is defined as q_0 . For any particle where $q < q_0$, the wall shear rate will not be influenced by the particle and the shear rate is defined as $\dot{\gamma}_{w,0}$. For the particle where $q > q_0$, the wall shear rate will be influenced by the particle, and the particle is defined as a wall particle. The average wall shear rate influenced by the i^{th} wall particle is defined as $\overline{\dot{\gamma}_{w,i}}$, and the area on the wall where the shear rate is influenced is defined as A_i , as illustrated in Figure 2.17.

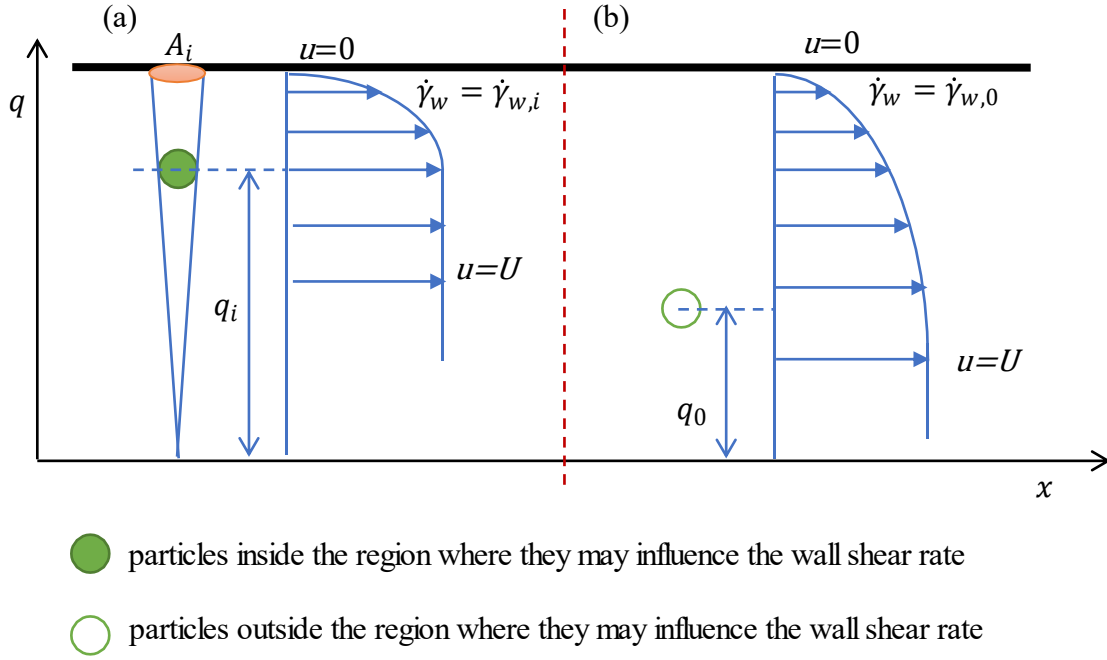


Figure 2.17 Schematic diagram of particles inside (a) and outside (b) the region where the particles may influence the wall shear rate.

Based on the above description of the flow, the force on the capillary wall can be derived as

$$F = \sum_{i=1}^{N_w} K_f (\overline{\dot{\gamma}_{w,i}})^{n_f} A_i + K_f \dot{\gamma}_{w,0}^{n_f} \left(1 - \sum_{i=1}^{N_w} A_i \right) \quad (2.11)$$

where K_f and n_f are the flow consistency and behavior indexes (respectively) for the fluid, and N_w is the number of particles near the wall ($q > q_0$). Since the total force on the capillary wall is the same in Equations (2.9) and (2.11), the relationship between K and K_f can be derived as

$$\frac{K}{K_f} = \left(1 + \sum_{i=1}^{N_w} \left(\left(\frac{\overline{\dot{\gamma}_{w,i}}}{\dot{\gamma}_{w,0}} \right)^{n_f} - 1 \right) \frac{A_i}{A_c} \right) \frac{\dot{\gamma}_{w,0}^{n_f}}{\dot{\gamma}_w^n} \quad (2.12)$$

According to Equation (2.12), $\frac{K}{K_f}$ is determined by the four terms: $\frac{\dot{\gamma}_{w,0}^{n_f}}{\dot{\gamma}_w^n}$, $\frac{\overline{\dot{\gamma}_{w,l}}}{\dot{\gamma}_{w,0}}$, $\frac{A_i}{A_c}$, and N_w . To analyze the relation between $\frac{K}{K_f}$ and properties of the particles, properties of the suspension fluid, and D , these four terms will be discussed below separately.

2.4.3.1 Model for $\frac{\dot{\gamma}_{w,0}^{n_f}}{\dot{\gamma}_w^n}$:

For the same type of suspension fluid, n_f is a constant. As the fully-developed suspension can be regarded as uniform at the free flow condition, the velocity profile is expected to have a universal shape for different D . Hence, $\dot{\gamma}_{w,0}$ and $\dot{\gamma}_w$ are also constants at the free flow condition after non-dimensionalizing. n is a function of particle volume fraction only as discussed in Chapter 2.4.1. Thus, it can be concluded that $\frac{\dot{\gamma}_{w,0}^{n_f}}{\dot{\gamma}_w^n}$ is a function of particle volume fraction only and can be represented as

$$G(\varphi) = \frac{\dot{\gamma}_{w,0}^{n_f}}{\dot{\gamma}_w^n} \quad (2.13)$$

Using Equation (2.7), Equation (2.13) can be expressed as

$$G(\varphi) = \frac{\dot{\gamma}_{w,0}^{n_f}}{\dot{\gamma}_w^n} = \frac{\dot{\gamma}_{w,0}^{n_f}}{\dot{\gamma}_w^{n_f(1+a\varphi)}} = \frac{\dot{\gamma}_{w,0}^{n_f}}{\dot{\gamma}_w^{n_f}} \dot{\gamma}_w^{-a\varphi} e^{\ln(\dot{\gamma}_w^{-a\varphi})} = e^{-a\varphi \ln(\dot{\gamma}_w)} = C_1 e^{b_1\varphi} \quad (2.14)$$

where C_1 and $b_1 = -a \ln(\dot{\gamma}_w)$ are constants and φ is the particle volume fraction. Using Equation (2.14), Equation (2.12) can be expressed as

$$\frac{K}{K_f} = G(\varphi) f_s \quad (2.15)$$

with

$$f_s = 1 + \sum_{i=1}^{N_w} \left(\left(\frac{\overline{\dot{\gamma}_{w,l}}}{\dot{\gamma}_{w,0}} \right)^{n_f} - 1 \right) \frac{A_i}{A_c}. \quad (2.16)$$

For the Group 1 and 2 experiments, the values of C_1 and b_1 for G obtained by $\frac{K}{K_f f_s}$. Details are presented in Section 2.4.3.6.

2.4.3.2 Model for $\frac{\overline{\dot{\gamma}_{w,l}}}{\dot{\gamma}_{w,0}}$:

The term $\frac{\overline{\dot{\gamma}_{w,l}}}{\dot{\gamma}_{w,0}}$ is the ratio of wall shear rates for the cases with and without particles near the capillary wall. As the fluid in the capillary is the same and the position of the particles relative to the wall is changing, the boundary flow profile shape near the capillary wall can be assumed “similar” for the two cases. That is, the velocity profile near the wall is modeled as

$$u = UH\left(\frac{y}{y_m}\right) \quad (2.17)$$

for $0 < y < y_m$ where y_m is the distance from the capillary wall at which the flow reaches the centerline velocity U , and H is a function describing the velocity profile shape. Then the shear rate of the boundary layer can be expressed as

$$\dot{\gamma} = \frac{\partial u}{\partial y} = H'(0) \frac{U}{y_m}. \quad (2.18)$$

Applying Equation (2.18) to the conditions of without and with a wall particle in the flow, the shear rates can be derived as

$$\dot{\gamma}_{w,0} = H'(0) \frac{U}{R - q_0} \quad (2.19)$$

and

$$\overline{\dot{\gamma}_{w,i}} = H'(0) \frac{U}{R - q_i}. \quad (2.20)$$

As $H'(0)$ is the same for both cases, $\frac{\overline{\dot{\gamma}_{w,i}}}{\overline{\dot{\gamma}_{w,0}}}$ can be expressed as

$$\frac{\overline{\dot{\gamma}_{w,i}}}{\overline{\dot{\gamma}_{w,0}}} = \frac{R - q_0}{R - q_i}. \quad (2.21)$$

Considering the value of q_0 is determined by the capillary radius R and particle radius r , the relationship among them can be modeled as

$$q_0 = R - \epsilon_0 r \quad (2.22)$$

where ϵ_0 is a constant for the same group data. To simplify the derivation in the following, q_i is modeled as

$$q_i = R - \epsilon_i r \quad (2.23)$$

where ϵ_i is a constant for the same group of data. Then the term $\frac{\overline{\dot{\gamma}_{w,i}}}{\overline{\dot{\gamma}_{w,0}}}$ can be expressed as

$$\frac{\overline{\dot{\gamma}_{w,i}}}{\overline{\dot{\gamma}_{w,0}}} = \frac{\epsilon_0}{\epsilon_i}. \quad (2.24)$$

The details of ϵ_0 and ϵ_i are analyzed later in Section 2.4.4.5.

2.4.3.3 Model for $\frac{A_i}{A_c}$:

As described above, the i^{th} wall particle can impact wall shear within the area of A_i on the wall as illustrated in Figure 2.18. As the angle β is small at free flow conditions (scale of ~ 0.01), it can be approximated as

$$\beta \approx \sin \beta \approx \tan \beta = \frac{r}{q_i} \quad (2.25)$$

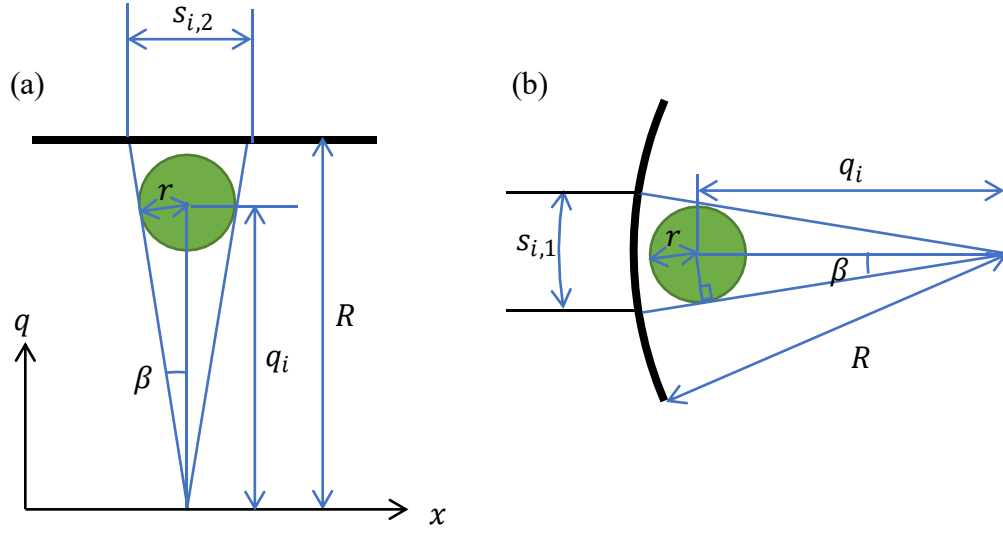


Figure 2.18 Schematic diagram of the i^{th} wall particle and its geometrical relation with the capillary and impacted area in the axial direction (a) and radial direction (b)

Based on the geometrical relations shown as Figure 2.18 and using the approximation in Equation (2.25), the following geometrical relations and approximations can be found:

$$s_{i,1} = 2\beta R \approx \frac{2Rr}{q_i} \quad (2.26)$$

$$s_{i,2} = 2R \tan \beta \approx \frac{2Rr}{q_i} \quad (2.27)$$

$$A_i \approx \frac{\pi}{4} s_{i,1} s_{i,2} = \pi \left(\frac{Rr}{q_i} \right)^2 \quad (2.28)$$

$$A_c = 2\pi RL \quad (2.29)$$

Hence, the term $\frac{A_i}{A_c}$ can be derived as a function of R , ϵ_i , r , and L as

$$\frac{A_i}{A_c} = \frac{R}{2L} \left(\frac{r}{q_i} \right)^2 = \frac{R}{2L} \left(\frac{r}{R - \epsilon_i r} \right)^2 \quad (2.30)$$

2.4.3.4 Model for N_w :

Using the above results, f_s can be expressed as

$$f_s = 1 + \sum_{i=1}^{N_w} \left(\left(\frac{\epsilon_0}{\epsilon_i} \right)^{n_f} - 1 \right) \frac{R}{2L} \left(\frac{r}{R - \epsilon_i r} \right)^2. \quad (2.31)$$

As the value of ϵ_i varies with particle location within the capillary, and total number of wall particles N_w is large, f_s is approximated by replacing ϵ_i with the average value $\bar{\epsilon}$ to simplify the analysis:

$$f_s \approx 1 + N_w \left(\left(\frac{\epsilon_0}{\bar{\epsilon}} \right)^{n_f} - 1 \right) \frac{R}{2L} \left(\frac{r}{R - \bar{\epsilon} r} \right)^2. \quad (2.32)$$

Based on the geometry of the capillary and particles, the total number of particles in the capillary, N_p , and the total number of wall particles, N_w , can be expressed as

$$N_w = N_p P_w \quad (2.33)$$

and

$$N_p = \frac{3}{4} \phi L \frac{R^2}{r^3} = \frac{3\phi L}{4R} \omega^3 \quad (2.34)$$

where P_w is the probability that a particle is in the region influencing the wall shear rate ($q > q_0$).

According to the micro-CT scan results in Section 2.4.2, the particles are uniformly distributed inside the capillary, on average. Hence, P_w can be calculated based on geometrical considerations. Calculation of the P_w in the actual three-dimensional (3-D) case can be simplified to the calculation of the probability for an equivalent two-dimensional (2-D) projection onto the capillary cross section given that the flow is fully-developed. The geometry for calculating the probability of particles located within a 2-D projected ring bounded by radii R_1 and R_2 is illustrated in Figure 2.19 with the particles represented as projected circles of radii r_{2D} .

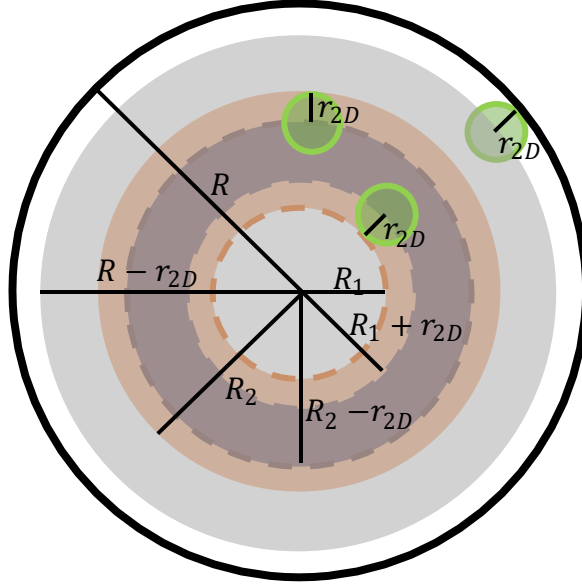


Figure 2.19 Schematic diagram of particles randomly distributed in a ring area and dimensions related to different regions that may contain particles

For the 2D projection, the probability that a particle is in the ring area between the radii of R_1 and R_2 can be determined as the ratio of the total accessible area in the ring to that of the capillary, namely,

$$P_{R_1 \leftrightarrow R_2} = \frac{(R_2 - r_{2D})^2 - (R_1 + r_{2D})^2}{(R - r_{2D})^2} \quad (2.35)$$

where R is the radius of the capillary, and r_{2D} is adjusted radius for the 2-D case. For the 2-D case, the particles are treated as cylinders of length $2r$, so the equivalent radius r_{2D} is determined so that particle volume is preserved, namely,

$$(2r)\pi r_{2D}^2 = \frac{4}{3}\pi r^3 \quad (2.36)$$

so that

$$r_{2D} = \sqrt{\frac{2}{3}}r. \quad (2.37)$$

Substituting Equation (2.37) into Equation (2.35) and using Equation (2.22) gives

$$P_w = P_{q_0 \leftrightarrow R} = \frac{r(2R - \epsilon_0 r) \left(\epsilon_0 - 2\sqrt{\frac{2}{3}} \right)}{\left(R - \sqrt{\frac{2}{3}}r \right)^2} = \frac{(2\omega - \epsilon_0) \left(\epsilon_0 - 2\sqrt{\frac{2}{3}} \right)}{\left(\omega - \sqrt{\frac{2}{3}} \right)^2}. \quad (2.38)$$

Hence, N_w is obtained as

$$N_w = N_p P_w = \frac{3\phi L}{4R} \omega^3 \frac{(2\omega - \epsilon_0) \left(\epsilon_0 - 2\sqrt{\frac{2}{3}} \right)}{\left(\omega - \sqrt{\frac{2}{3}} \right)^2} \quad (2.39)$$

Using the above results, f_s for the free flow condition ($\omega > \omega_{pic}$) can be modeled as

$$f_s \approx 1 + \frac{3\phi}{8} \left(\epsilon_0 - 2\sqrt{\frac{2}{3}} \right) \left(\left(\frac{\epsilon_0}{\bar{\epsilon}} \right)^{n_f} - 1 \right) \frac{\omega^3 (2\omega - \epsilon_0)}{(\omega - \bar{\epsilon})^2 \left(\omega - \sqrt{\frac{2}{3}} \right)^2}. \quad (2.40)$$

2.4.3.5 Determination of ω_{pic} , ϵ_0 and $\bar{\epsilon}$

Particles start interfering with each other to increase K under the particle interaction condition ($\omega < \omega_{pic}$) as discussed in Section 2.4.2. The interaction comes from the forces generated between two adjacent particles by the flow between them when the separation distance is small enough, resulting in rapid increasing of the flow consistency index. As the interaction is perpendicular to the flow direction, the particle separation distance causing the interaction is in the radial direction as illustrated in Figure 2.20.

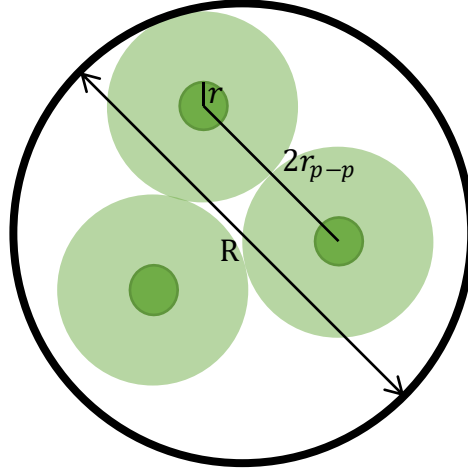


Figure 2.20 Schematic diagram of particles and their interaction spheres under dense packing

The fluid within the region of particle interaction is defined as a sphere with the radius of r_{p-p} as shown in Figure 2.20. When the distance between two particles is smaller than $2r_{p-p}$, they are considered to interact. Following the observation that the interaction is in the radial direction, analysis the interaction can be performed on a 2-D projection of the capillary cross-section as with the method of calculating probability used in Section 2.4.3.3. Based on these assumptions, when $\omega = \omega_{pic}$ (particle interaction starts), the relationship between r_{p-p} and the capillary dimensions is given by

$$N_{2D}\pi r_{p-p}^2 = \varphi_{SP}\pi R^2 \quad (2.41)$$

where φ_{SP} is the sphere volume ratio for close packing in the capillary (cylinder) and N_{2D} is the number of particles in the capillary cross section. Its value is determined by D , the interaction sphere mean radius, and the particle distribution (the particle mean size and its distribution). In this case ($\omega = \omega_{pic}$), ω is large enough that the boundary spheres around the particles can be

regarded as dense packed inside the capillary. When ω is smaller, more complex analysis is required [89].

According to the geometrical relationship between the particle and capillary cross-sections, N_{2D} , can be derived as

$$N_{2D} = \frac{\varphi\pi R^2}{\pi r_{2D}^2} = \frac{3\varphi R^2}{2r^2} = \frac{3\varphi}{2} \omega^2 \quad (2.42)$$

Combining Equations (2.41) and (2.42) gives an expression for r_{p-p} . As the particles are constrained in the capillary with the radius of R , it is reasonable to assume when $\alpha_{p-p} \equiv \frac{R}{r_{p-p}}$ arrives at a characteristic value, α_{pic} , the particle interaction condition is achieved. Eliminating N_{2D} from Equations (2.41) and (2.42) and rearranging gives

$$\frac{r_{p-p}}{R} = \frac{1}{\alpha_{pic}} = \frac{1}{\omega_{pic}} \sqrt{\frac{2\varphi_{SP}}{3\varphi}} \quad (2.43)$$

Hence, the relation between ω_{pic} and the particle volume fraction φ has the following form:

$$\omega_{pic} = \frac{C_2}{\sqrt{\varphi}}, \quad \text{where } C_2 = \alpha_{pic} \sqrt{\frac{2}{3} \varphi_{SP}}. \quad (2.44)$$

As the options of capillary and particle size are limited, ω_{pic} cannot be directly detected from the experiments. However, a reasonable approximation can be made by using K vs. ω linear trendlines on both sides of ω_{pic} (location of minimum K). The intersection of the two trendlines determines the approximate value of ω_{pic} . An example for $\varphi = 10\%$ is illustrated in Figure 2.21. Values of ω_{pic} and its flow behavior index K_{min} determined in this way for Group 1 and 2 experiments are listed in Table 2.6. A least square fit of Equation (2.44) to the results in Table 2.6 gives $C_2 = 18.5 \pm 0.2$. The uncertainties were calculated from Jackknife method [106]. The results of this fit are shown in Figure 2.22.

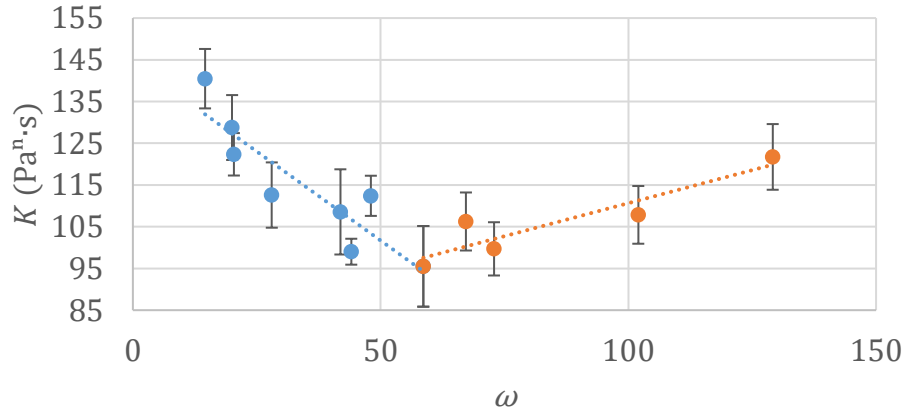


Figure 2.21 ω_{pic} obtained from K ($\text{Pa}^n \cdot \text{s}$) and ω trendlines (when $\varphi = 10\%$ for Group 1 and 2 experiments)

Table 2.6 Approximate ω_{pic} and K_{min} for Group 1 and 2 experiments

φ	10%	20%	30%	40%
ω_{pic} [-]	58	44	33	27
K_{min} ($\text{Pa}^n \cdot \text{s}$)	96	125	186	223

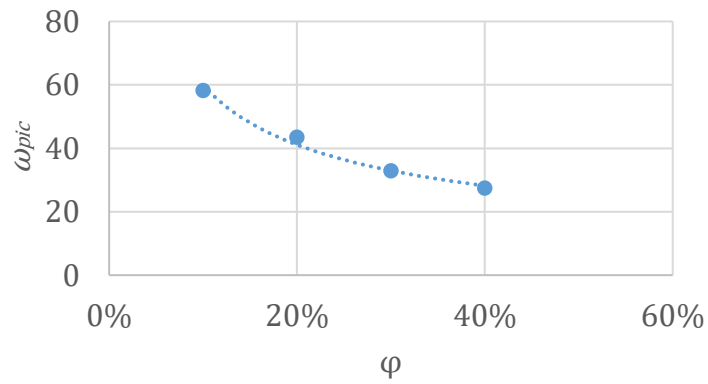


Figure 2.22 ω_{pic} vs. φ for experimental results for Group 1 and 2

The $\epsilon_0 r$ term is the largest distance from the capillary wall for which particles may affect the wall shear rate. At the end of free flow condition ($\omega = \omega_{pic}$), the flow has the largest number of particles impacting the wall shear rate. To simplify the calculation, it can be assumed that all the particles affect the wall shear rate at this point. Hence, the governing radius of the sphere is the same as the capillary radius as shown in Figure 2.23. That is, at $\omega = \omega_{pic}$

$$\epsilon_0 r = R, \tag{2.45}$$

in which case ϵ_0 is given by

$$\epsilon_0 = \omega_{pic} = C_2 \varphi^{-\frac{1}{2}}. \tag{2.46}$$

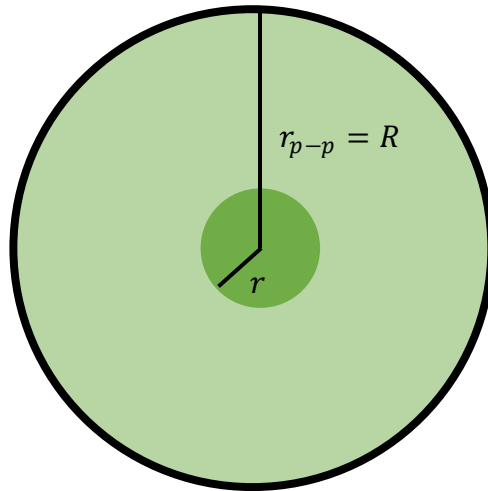


Figure 2.23 Schematic diagram of a wall particle with largest r_{p-p} at $\omega = \omega_{pic}$

The average distance between particles and the capillary wall is given by $\bar{\epsilon} r$. For real flows, many factors may impact on this value, including particle size variation, particles “sheltering” next to adjacent particles, etc. (additional detail is presented in Section 2.4.3.6). To accommodate this complexity, $\bar{\epsilon}$ is determined empirically using $\frac{K_{min}}{K_{inf}}$.

As determined previously, K_{min} is the minimum value of K when $\omega = \omega_{pic}$ for the same φ . K_{inf} is the value of K when $\omega \rightarrow \infty$ and K can be regarded as a constant for the same φ . Values of K_{inf} at $\varphi = 30\%$ and 40% were directly measured as shown in Figure 2.7 (a). However, they cannot be measured directly at $\varphi = 10\%$ and 20% as the required ω is too large as shown in Figure 2.7 (a), and the testing system cannot provide it. Instead, values of K_{inf} at $\varphi = 10\%$ and 20% were obtained by following a 2nd order polynomial model as discussed in Section 2.1 (an exponential model provides similar results). Values of K_{inf} determined this are listed in Table 2.7 and plotted in Figure 2.24 for the Group 1 and 2 experiments.

Table 2.7 Approximate K_{inf} for Group 1 and 2 experiments

φ	0%	10%	20%	30%	40%
K_{inf} ($\text{Pa}^n \cdot \text{s}$)	92	135	175	237	280

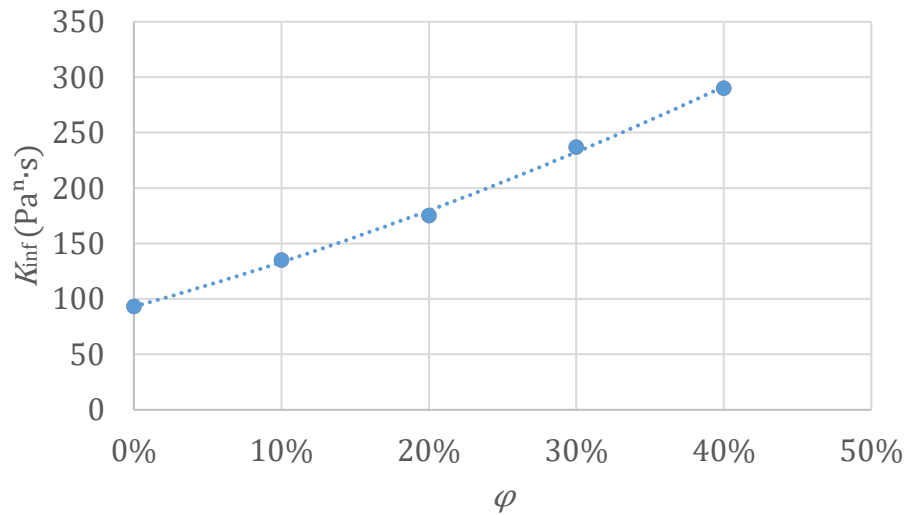


Figure 2.24 K_{inf} ($\text{Pa}^n \cdot \text{s}$) vs. φ for experimental results for Group 1 and 2.

Combining Equations (2.13), (2.14), (2.40), and (2.46), $\frac{K_{min}}{K_{inf}}$ can be expressed as a function of

$\bar{\epsilon}$ and φ , namely,

$$\frac{K_{min}}{K_{inf}} = \frac{1 + \frac{3C_2^4\varphi^3 \left(C_2\varphi^{-\frac{1}{2}} - 2\sqrt{\frac{2}{3}} \right) \left(\left(\frac{C_2\varphi^{-\frac{1}{2}}}{\bar{\epsilon}} \right)^{n_f} - 1 \right)}{8 \left(C_2\varphi^{-\frac{1}{2}} - \bar{\epsilon} \right)^2 \left(C_2\varphi^{-\frac{1}{2}} - \sqrt{\frac{2}{3}} \right)^2}}{1 + \frac{3\varphi}{4} \left(C_2\varphi^{-\frac{1}{2}} - 2\sqrt{\frac{2}{3}} \right) \left(\left(\frac{C_2\varphi^{-\frac{1}{2}}}{\bar{\epsilon}} \right)^{n_f} - 1 \right)}. \quad (2.47)$$

By substituting values of K_{min} , K_{inf} , and φ into Equation (2.47), the values of $\bar{\epsilon}$ at different φ can be determined, giving the results listed in Table 2.8.

Table 2.8 Approximate $\bar{\epsilon}$ vs. φ for experimental results for Group 1 and 2

φ	10%	20%	30%	40%
$\bar{\epsilon}$ [-]	7.2	6.7	5.2	4.8

As $\bar{\epsilon}$ is closely related with ϵ_0 , an empirical power law relationship is proposed to simplify calculations:

$$\bar{\epsilon} = C_3\varphi^{b_3} \quad (2.48)$$

where C_3 and b_3 are two adjustable parameters. For the Group 1 and 2 experiments, a least square fit of Equation (2.48) to the results in Table 2.8 gives $C_3 = 3.5 \pm 0.4$ and $b_3 = -0.34 \pm 0.11$.

The uncertainties were calculated using the Jackknife method [106]. The results of this fit are shown in as Figure 2.25.

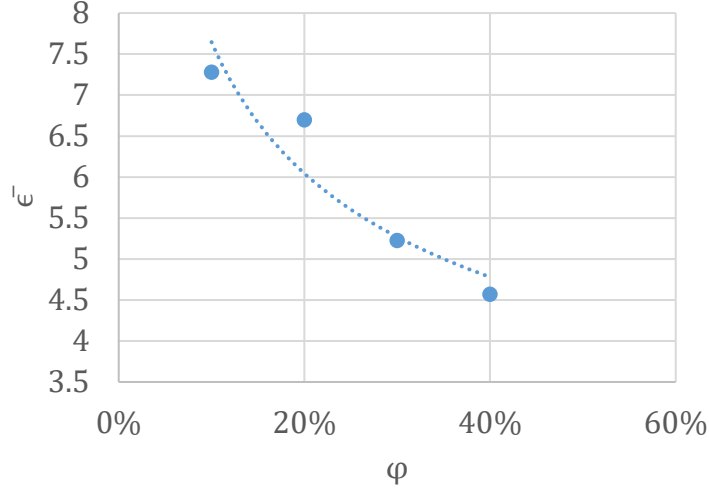


Figure 2.25 $\bar{\epsilon}$ vs. φ (from experimental results for Group 1 and 2).

Combining the above results, the function to describe the flow behavior of a particulate suspension with the same particle volume fraction can be expressed as

$$\frac{K}{K_f} = C_1 e^{b_1 \varphi} \left(1 + \frac{3\varphi \left(C_2 \varphi^{\frac{1}{2}} - 2\sqrt{\frac{2}{3}} \right) \left(\left(\frac{C_2}{C_3} \varphi^{\frac{1}{2} - b_3} \right)^{n_f} - 1 \right) \omega^3 \left(2\omega - C_2 \varphi^{\frac{1}{2}} \right)}{(\omega - C_3 \varphi^{b_3})^2 \left(\omega - \sqrt{\frac{2}{3}} \right)^2} \right). \quad (2.49)$$

2.4.3.6 Comparison between the model and data

f_s was calculated following the model developed in Sections 2.4.3.2 to 2.4.3.5 with the results shown in Table 2.9. With K obtained from experiments as shown in (see Figure 2.7 (a)) and known K_f , the values of G were obtained as listed in Table 2.9. A least square fit of Equation (2.12) to the results for G gives $C_1 = 5.6 \pm 0.4$ and $b_1 = 1.6 \pm 0.2$. The uncertainties were calculated

using the Jackknife method [106]. The results of this fit are shown in as the dotted line in Figure 2.26.

Table 2.9 f_s and G vs. φ for experimental results for Group 1 and 2

φ	10%	20%	30%	40%
f_s [-]	20.3	24.1	26.1	27.2
G [-]	6.6	7.2	9.1	10.7

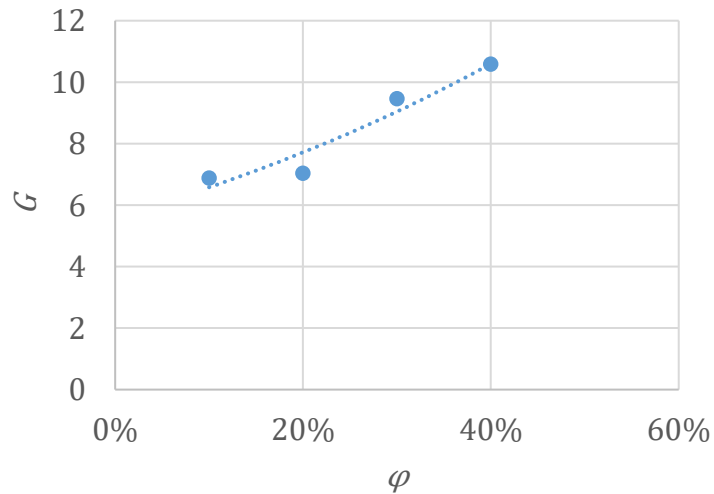


Figure 2.26 Free flow condition particle volume fraction dependence of G vs. φ (experimental results for Group 1 and 2). The dotted line is the best fit curve from Equation (2.12).

A comparison between the model for K in the free flow condition and the measured results is shown in Figure 2.27 with Equation (2.49) and the parameters discussed above.

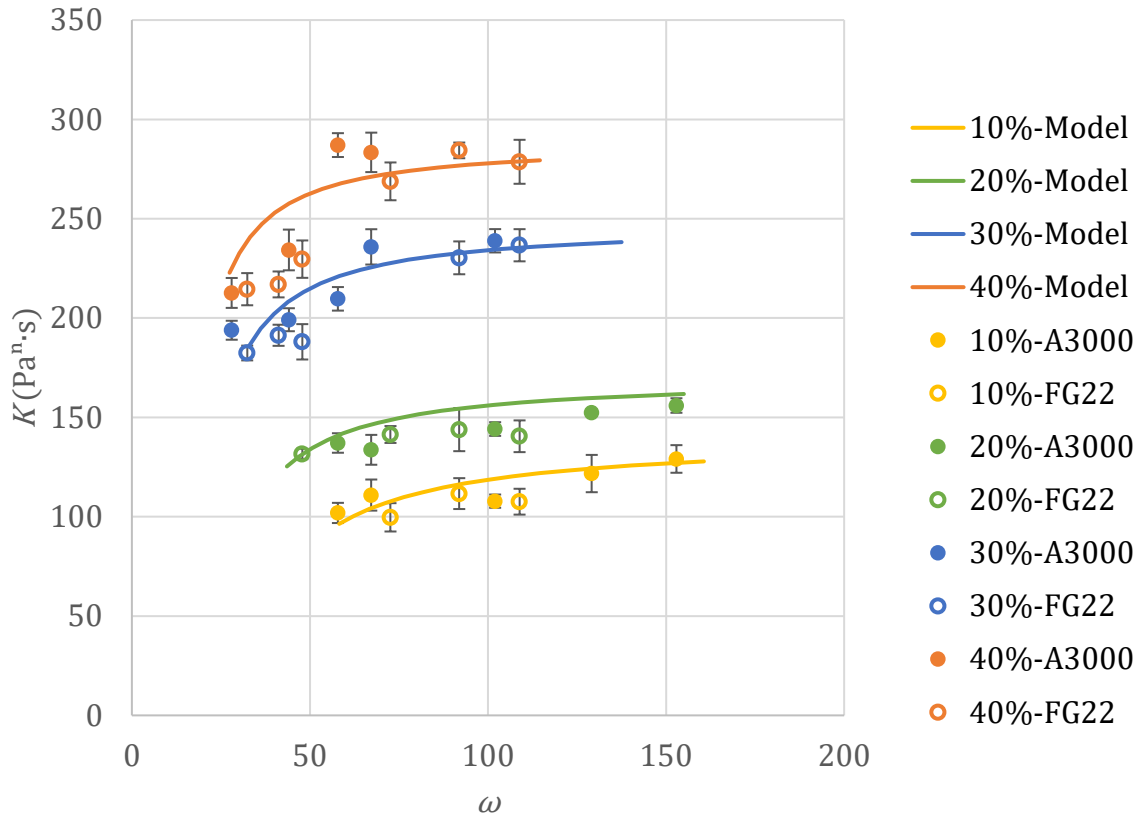


Figure 2.27 Flow consistency index K ($\text{Pa}^n \cdot \text{s}$) vs. ratio of capillary and particle mean radius ω (experimental results for Groups 1 and 2) under the free flow condition with legend indications following the format: particle volume fraction – particle type

The model generally follows the trends in the data well. The possible reasons for differences between the model and experiments (aside from experimental uncertainty and uncertainty in the model fitted parameters) are likely related to simplifications utilized to obtain the model. Particles may be adjacent to one another on the wall, as illustrated in Figure 2.28 (a), resulting in higher wall shear rate. Some particles may be close enough to each other near the wall in the radial direction that particles at smaller radii are “sheltered” by the particle in the front, as illustrated in Figure 2.28 (b), resulting in minimal impact from the sheltered particle on the wall shear rate.

Additionally, the particles are regarded as the same size in the model. However, the actual situation involves polydisperse spheres, which may lead to complex packing density and other effects as illustrated in Figure 2.28 (c).

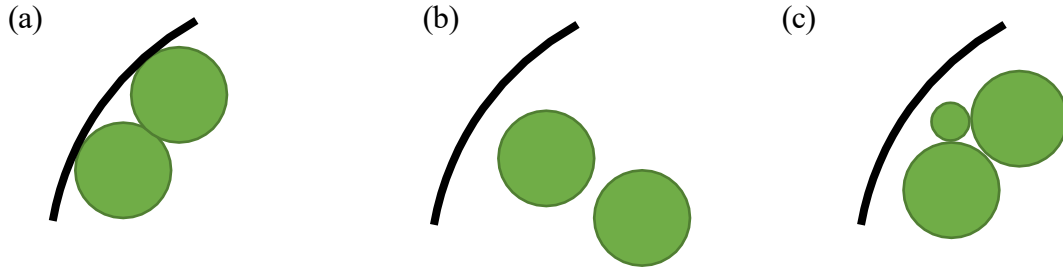


Figure 2.28 Sketches of possible particle situations not considered in the model: adjacent particles (a), sheltered particles (b), and polydisperse particles (c).

2.4.4. Semi-empirical Models for the Particle Interaction Condition

As shown in Figure 2.15, K increases with decreasing ω in the particle interaction condition ($\omega_{pic} > \omega > \omega_{jc}$). This behavior results from the interaction of nearby particles as discussed in Chapter 2.3.4.5. The interaction becomes stronger with smaller distance between particles, which is controlled by ω and φ .

As the interaction can only happen when the particulate suspension is moving, it is impossible to visualize the particle interaction with the micro-CT. Hence, the particle interaction condition is modeled using an empirical relationship as

$$K = \frac{A}{(\omega - \omega_{jc})^b} \quad (2.50)$$

where ω_{jc} is the value of ω when jamming occurs ($K \rightarrow \infty$), and A and b are curve fitting parameters.

2.4.4.1. Model for ω_{jc}

For the reason of limited options of capillary and particle size, ω_{jc} can not be directly determined. Rewriting Equation (2.50) as

$$\ln(K) = \ln(A) - b \ln(\omega - \omega_{jc}) \quad (2.51)$$

a linear relationship can be found between $\ln(K)$ and $\ln(\omega - \omega_{jc})$. By adjusting the value of ω_{jc} around where jamming happens (detected from experiments), the $\ln(K)$ vs. $\ln(\omega - \omega_{jc})$ linear trendline with least square error can be obtained, as illustrated in Figure 2.29. ω_{jc} on this condition is regarded as the approximate value used in the models as illustrated in Figure 2.29. The ω_{jc} obtained in this was for experimental results for Group 1 and 2 are listed in Table 2.10.

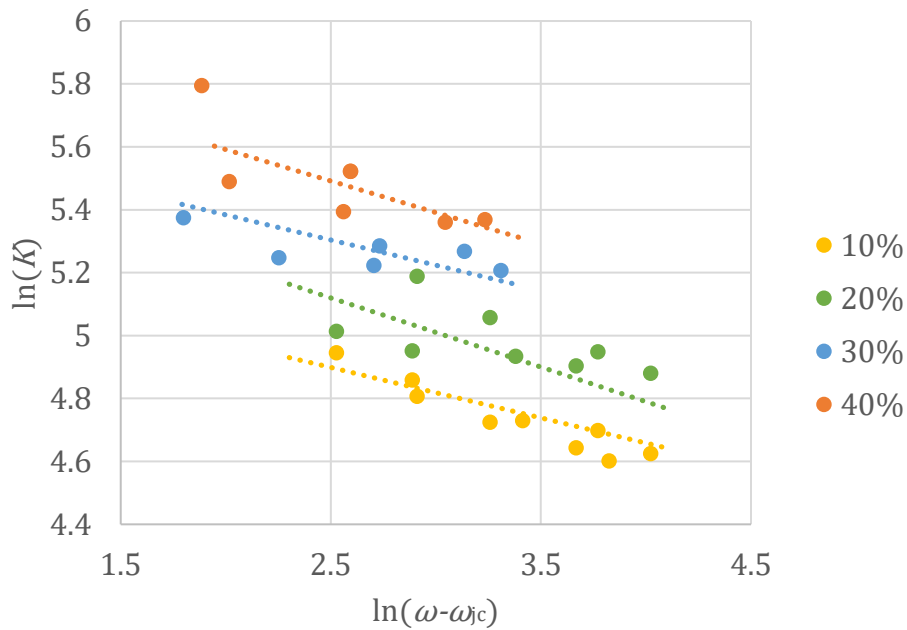


Figure 2.29 Illustration of obtaining approximate ω_{jc} (experimental results for Group 1 and 2). The legend indicates the particle volume fraction.

Table 2.10 Semi-empirical values of ω_{jc} (for experimental results for Group 1 and 2)

φ	10%	20%	30%	40%
ω_{jc} [-]	2.3	2.0	4.2	7.9

According to the experimental results, jamming occurs at larger ω when φ increases. This behavior is expected from behavior at limiting conditions. For the limiting case of only one particle in the suspension, $\varphi = 0$. However, jamming can still happen with only one particle in the capillary if the particle is the same diameter as the capillary. That is, $\omega_{jc} \rightarrow 1$ as $\varphi \rightarrow 0$. With more particles added into the suspension, particle volume fraction φ increases and will approach its maximum particle volume fraction, φ_M , for which each particle is in contact with multiple other particles and the liquid matrix fills the voids. At this condition, the particle configuration is stable even under the action of finite loads and the suspension has become jammed even with a very large capillary. For this condition, $\omega_{jc} \rightarrow \infty$. The value of φ_M may be impacted by many factors [89]. However, to simplify the analysis, it is reasonable to assume the particles are monodisperse spheres. As clear experimental evidence shows, monodisperse spheres start spanning the fluid domain from $\varphi \approx 0.49$ when the spheres are randomly packed [89], so $\varphi_M = 0.49$ was used in this work. To capture the dependence of ω_{jc} on φ it is represented as

$$\omega_{jc} = \frac{C_4}{(\varphi_M - \varphi)^{b_4}} \quad (2.52)$$

where C_4 and b_4 are two adjustable parameters. For the Group 1 and 2 experiments, a least square fit of Equation (2.52) to the results gives the values of $C_4 = 1.0 \pm 0.3$ and $b_4 = 0.86 \pm 0.21$. The results of this fit are shown in as Figure 2.30. In the real experimental situation, more factors including particle size distribution influence ω_{jc} and impact jamming. Details are presented in Section 2.4.4.4.

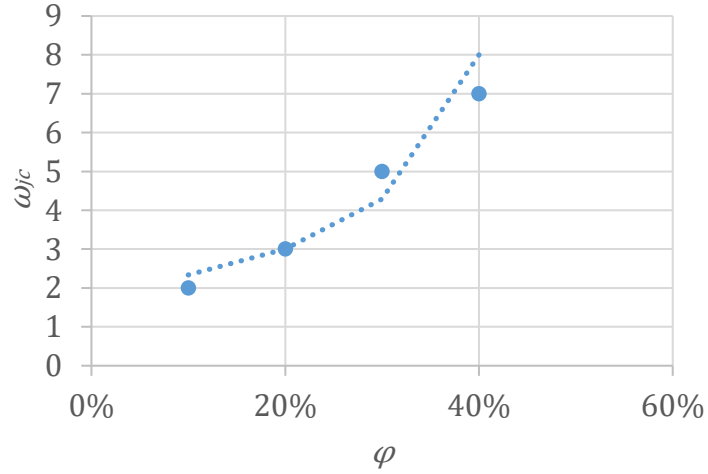


Figure 2.30 ω_{jc} vs. φ (experimental results for Group 1 and 2)

2.4.4.2. Model for b and A

In the process of empirically determining ω_{jc} , it was found that the slopes of $\ln(K)$ vs. $\ln(\omega - \omega_{jc})$ (b in Equation (2.51)) were close for all φ . A reasonable model for b , then, is the average slope for all cases, which is 0.16.

With the values of ω_{jc} and b in Equation (2.50) determined from the best fit to the data and modeled by $b = 0.16$ and Equation (2.52) for ω_{jc} , the value of A in Equation (2.50) was determined to match the value of K_{min} at $\omega = \omega_{pic}$ for the free flow conditions computed from Equation (2.49). The values for A obtained from this method are listed in Table 2.11. As A increases with particle volume fraction, a simple linear model is proposed for this quantity:

$$A = b_5\varphi + C_5 \quad (2.53)$$

where C_5 and b_5 are two adjustable parameters. For the Group 1 and 2 experiments, a least square fit of Equation (2.53) to the results gives the values of $C_5 = 118 \pm 9$ and $b_5 = 623 \pm 28$. The uncertainties were calculated using the Jackknife method [106]. The results of this fit are shown in as Figure 2.31.

Table 2.11 Semi-empirical values of A (for experimental results for Group 1 and 2)

φ	10%	20%	30%	40%
A ($\text{Pa}^n \cdot \text{s}$)	184	229	315	363

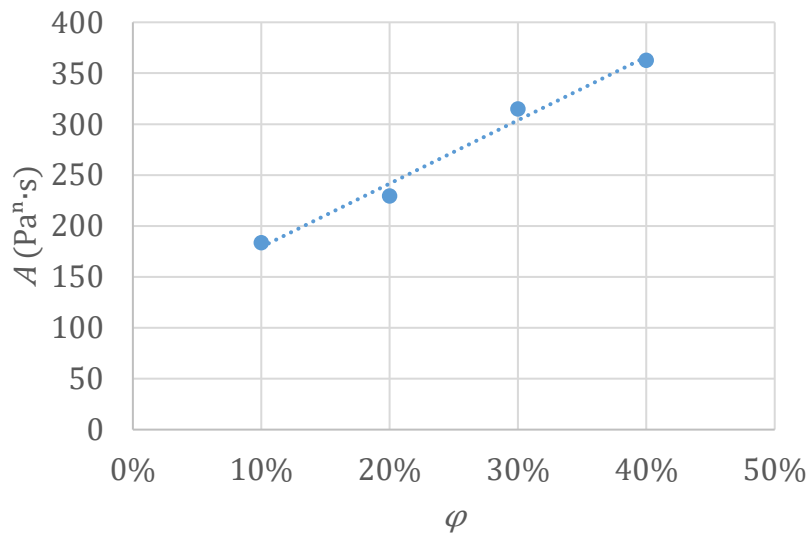


Figure 2.31 A ($\text{Pa}^n \cdot \text{s}$) vs. φ (experimental results for Group 1 and 2)

2.4.4.3. Comparison between model and measurements for the particle interaction condition

From Equations (2.50) to (2.53), K under particle interaction condition is modeled as

$$K_{pic} = \frac{b_5\varphi + C_5}{\left(\omega - \frac{C_4}{(\varphi_M - \varphi)^{b_4}}\right)^b} \quad (2.54)$$

Using the empirical constants determined above based on the experimental results for Group 1 and 2 for $\omega_{jc} < \omega < \omega_{pic}$ give the curves shown in Figure 2.32, which are plotted together with the corresponding measurements for K . The model results show acceptable agreement with the measurements.

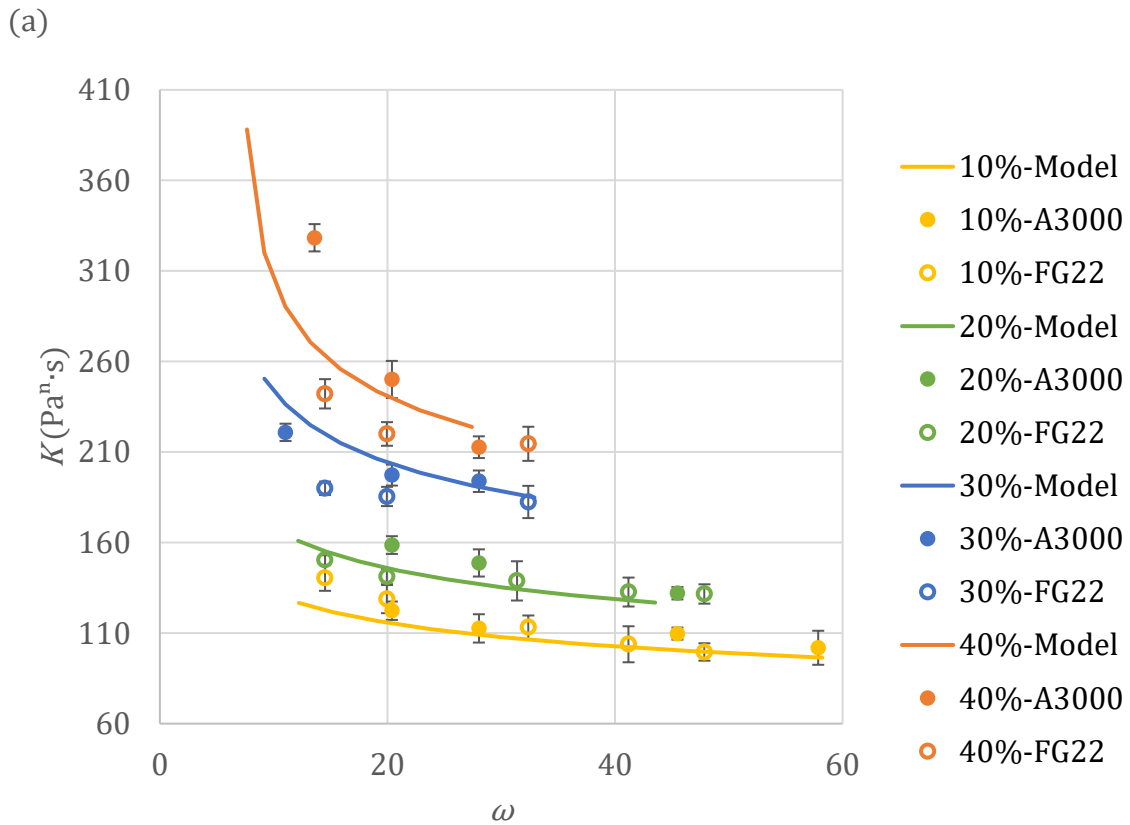


Figure 2.32 Flow consistency index K ($\text{Pa}^n \cdot \text{s}$) vs. ω (experimental results for Group 1 and 2) under particle interaction condition with legend indications following the format: particle volume fraction – particle type

Besides φ and ω , there is another possible factor influencing the suspension rheology under the particle interaction condition. As presented in Figure 2.32, the K values may differ when ω is the same but the types of particles are different. This may be caused by different particle size distributions. It is also noted that suspensions of the same particle volume fraction with particles having a wider particle size distribution have a larger K for the same ω . A possible explanation is the larger particles dominate the interaction. It is also found this trend is more significant with higher particle volume fraction, as the interaction is stronger when there are more particles to interact.

2.4.4.4.Explanation on jamming and particle clustering

As discussed in Section 2.4.2, jamming occurs when particles begin to cluster and span the entire capillary. The most important parameter describing jamming is ω_{jc} . An empirical model proposed in Equation 2.32 captures the basic behavior. It shows ω_{jc} increasing with particle volume fraction φ increasing as expected, meaning jamming has a higher probability of happening when the particle volume fraction is higher.

One key phenomenon of ω_{jc} is that jamming does not always happen at this ratio in the conducted experiments. As ω_{jc} is derived from the semi-empirical process as presented in Section 2.4.4.1, the impact of particle size distribution is ignored. In the real situation, the particles have different sizes as demonstrated in Section 2.2.2. The particle clustering results from particle interaction, which is dominated by the larger particles as assumed in Section 2.4.4.3. Hence, jamming has higher probability of happening when the particle size range is larger for the same ω and φ . For example, when ω is similar, the jamming happened three times in all three tests with

the suspension made of UV 225-1 and $\varphi = 30\%$ FG22, and happened two times in all three tests with the suspension made of UV 225-1 and $\varphi = 30\%$ A3000.

Additionally, the impact of particle size distribution on jamming is stronger with higher particle volume fraction. The possibility of particle jamming was different for the $\varphi = 30\%$ suspensions as discussed above. However, there was almost no difference in jamming with FG22 and A3000 at $\varphi = 10\%$. This behavior is also expected, following the trends observed for the particle interaction condition (demonstrated in Section 2.4.4.3).

2.5 Rheology Conclusion

In this chapter, the rheology of particulate suspensions in shear thinning fluids was investigated, concentrating on the flow behavior (n) and consistency (K) indices. Related theories and models on viscosity were reviewed and compared. Experiments to investigate the indices were designed and conducted. Particle volume fraction (φ) and the ratio of capillary ID to the particle mean size (ω) were found to be the key factors impacting the suspension rheology.

Based on the experimental results, the flow behavior index n was found to be only dependent on φ for a suspension with the same suspension fluid. A linear relation between n and φ was observed and modeled with an empirical equation with acceptable accuracy.

The flow consistency index K was also investigated based on the experimental results. It was found the behavior of K for suspensions with different φ followed the similar trends with ω . The behavior was categorized into two categories: the free flow condition and the particle interaction condition. Analysis based on the results and fluid mechanics were conducted for both conditions. Equations to model K were generated for both conditions. With all the models together, the flow consistency index of the particulate suspension with different φ and ω can be described with

acceptable accuracy as illustrated in Figure 2.33. Differences between the model and tested results were also discussed. The flow with the same ϕ and ω has a larger K when the particles have a wider size distribution. Possible factors impacting jamming were also assessed. Higher ϕ and a wider particle size distribution may result in a higher probability of jamming occurring.

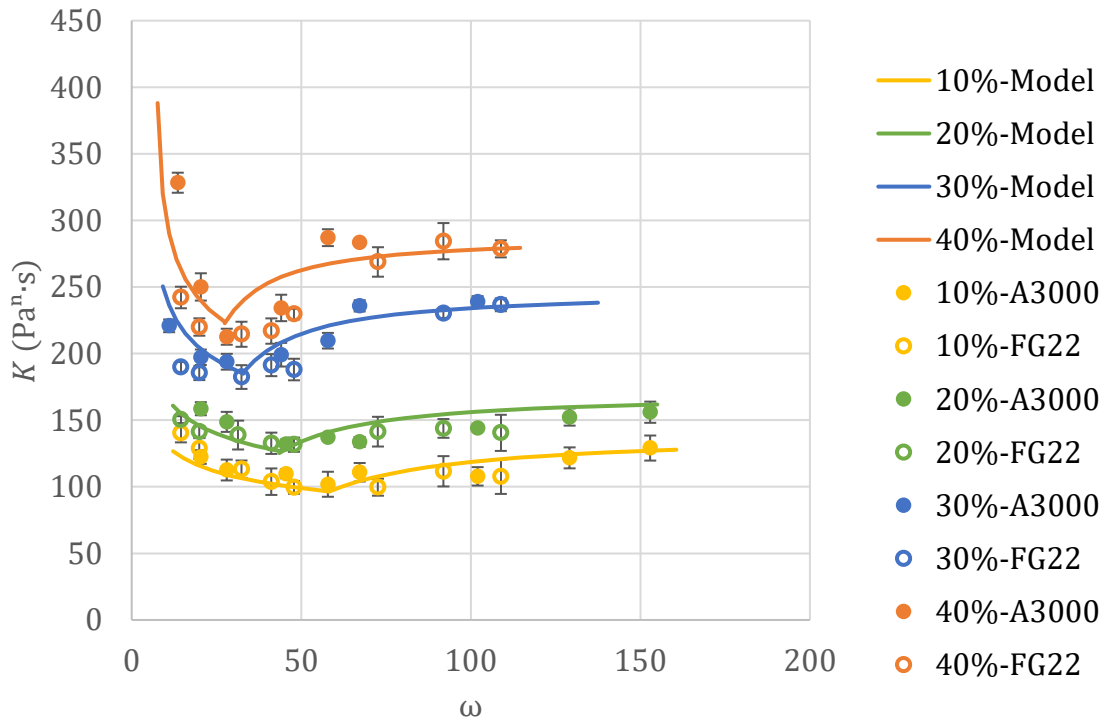


Figure 2.33 Flow consistency index K ($\text{Pa}^n \cdot \text{s}$) vs. ω (experimental results for Group 1 and 2) under the both flow conditions with legend indications following the format: particle volume fraction – particle type

CHAPTER 3 ELECTRICAL RESISTIVITY OF PARTICULATE COMPOSITES

To guarantee the manufactured products can achieve the desired function, the required properties of the component materials, such as mechanical strength, electrical conductivity, thermal conductivity, etc., should be in the desired range. Thus, it is important to investigate how material properties behave with different formulations and processing conditions.

Since the FEAM process utilizes ECPC to provide electrical conductivity between fiber segments, it is essential to investigate its electrical conductivity and how this property depends on formulation and processing of the ECPC. In this chapter, related theories and models for electrical conductivity in particulate composites are reviewed and developed, and experiments for quantifying performance under a variety of conditions are presented. To quantify electrical behavior, electrical resistivity (the inverse of conductivity) is used in this chapter.

3.1 Introduction to Quantum Tunneling Composite

In ECPC, the particles in the composite are electrically conductive. The bulk particulate composite can also be electrically conductive if the particle amount is high enough to form conductive paths throughout the material (percolation). The leading theory for the conductive behavior in the particle paths posits quantum tunneling effects as the primary conduction mechanism between adjacent particles in conductive paths. Such materials are also called quantum tunneling composites.

In quantum tunneling composites, the particles are viewed as encapsulated in the matrix material so that there is no direct atomistic contact between the conductive particles (see Figure 3.1 (a)). As such, the physical phenomenon of quantum tunneling is employed to describe how electrons can “jump” from one particle to another when a very thin insulating layer exists between them.

Many models of quantum tunneling composite electrical resistivity have been introduced [46-74]. Most of them concentrate on the resistance resulting from the quantum tunneling effect while ignoring other resistance as being negligible compared to the quantum tunneling resistance. However, to be explicit regarding models of composite resistance, with the overall material resistance can be regarded as resulting from two effects: the resistance of the conductive particles, which is called the particle resistance, and the resistance from quantum tunneling between adjacent particles, which is called the junction resistance [61]. Considering these two types of resistance, the composite can be regarded as a network of resistor as illustrated schematically in Figure 3.1 (b).

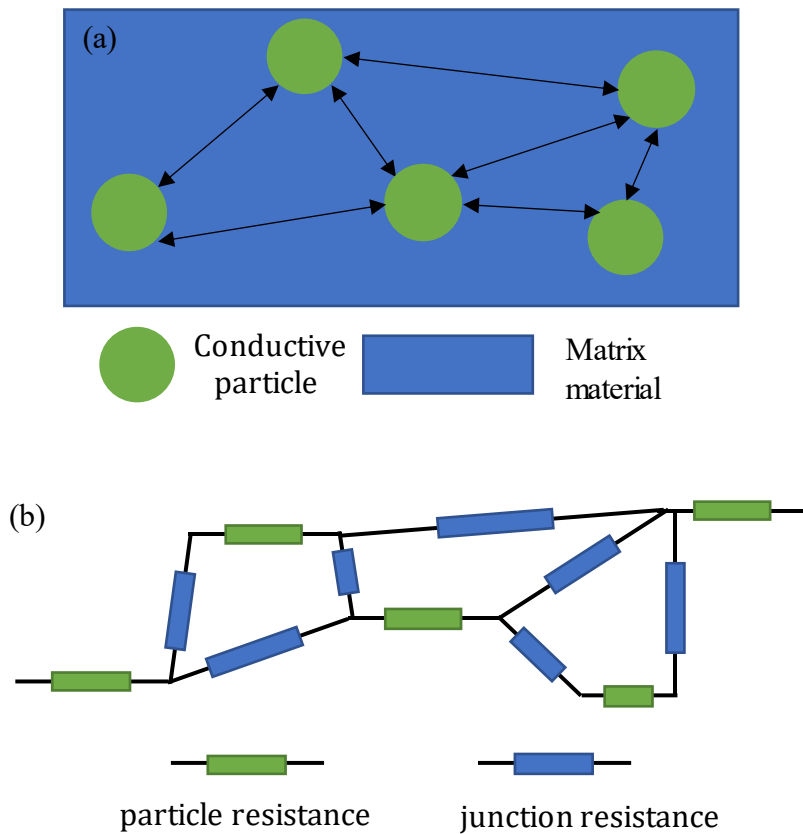


Figure 3.1 Schematic diagram of particles in the composite (a) and its resistor model (b)

Utilizing this physical description, the total resistance of a sample can be modeled as

$$\frac{1}{R_{total}} = \sum_{m=1}^{N_{path}} \frac{1}{R_{path,m}} \quad (3.1)$$

where R_{total} is the total resistance of the composite, N_{path} is the number of resistor paths, and $R_{path,m}$ is the resistance of the m^{th} path. Following the resistance in a path, it can be modeled as

$$R_{path,m} = \sum_{n=1}^{N_{pp,m}-1} R_{j,m,n} + \sum_{n=1}^{N_{pp,m}} R_{p,m,n} \approx \sum_{n=1}^{N_{pp,m}} (R_{j,m,n} + R_{p,m,n}) \quad (3.2)$$

where $N_{pp,m}$ is the number of conductive particles forming the m^{th} path ($N_{pp,m} \gg 1$), $R_{j,m,n}$ is the junction resistance between the n^{th} and $n + 1^{th}$ adjacent particles in path m , and $R_{p,m,n}$ is the resistance of the n^{th} particle in path m .

To simplify the derivation, the average resistance of all the paths, $\overline{R_{path}}$, is used. Following above equations, it can be derived as

$$\overline{R_{path}} = \frac{\sum_{m=1}^{N_{path}} R_{path,m}}{N_{path}} = \frac{\sum_{m=1}^{N_{path}} \sum_{n=1}^{N_{pp,m}} (R_{j,m,n} + R_{p,m,n})}{N_{path}} = N_{pp} (R_j + R_p) \quad (3.3)$$

where N_{pp} is average number of conductive particles forming a path, R_j is the average junction resistance, and R_p is the average particle resistance, each of which can be expressed as

$$N_{pp} = \sum_{m=1}^{N_{path}} \frac{N_{pp,m}}{N_{path}} \quad (3.4)$$

$$R_j = \frac{1}{N_{pp} N_{path}} \sum_{m=1}^{N_{path}} \sum_{n=1}^{N_{pp,m}} R_{j,m,n} \quad (3.5)$$

$$R_p = \frac{1}{N_{pp}N_{path}} \sum_{m=1}^{N_{path}} \sum_{n=1}^{N_{pp,m}} R_{p,m,n} \quad (3.6)$$

Hence, R_{total} can be modeled as

$$R_{total} = \frac{N_{pp}(R_j + R_p)}{N_{path}} \quad (3.7)$$

According to the preliminary tests of ECPC resistivity, the smallest resistivity of ECPC is on the order of 10^{-2} to $\Omega \cdot \text{cm}$. Compared with the resistivity of the conductive particles (Potter Industry SN08P40) of $5.04 \times 10^{-6} \Omega \cdot \text{cm}$, R_p is negligible. Hence, R_p can be ignored in the above equation, giving R_{total} as

$$R_{total} \approx \frac{N_{pp}R_j}{N_{path}} \quad (3.8)$$

where R_j is the average junction resistance.

Under the quantum tunneling model, the average junction resistance R_j can be derived based on the tunneling current from Schrödinger's equation [61-68], resulting in

$$R_j = \frac{V}{a^2 J} = \frac{8\pi h s}{3a^2 \Gamma e_0^2} \exp(\Gamma s) \quad (3.9)$$

where V is the applied voltage, J is the average current density through the junction under the applied voltage, a^2 is the average effective cross-sectional area of the junction, $\Gamma = \frac{4\pi}{h} \sqrt{2m_0\psi_p}$ is a constant for the same type of matrix material, m_0 and e_0 are the electron mass and charge respectively, h is Plank's constant, s is the average junction distance, or the average distance between two adjacent conductive particles (see Figure 3.2), and ψ_p is the height of the potential barrier between the adjacent particles.

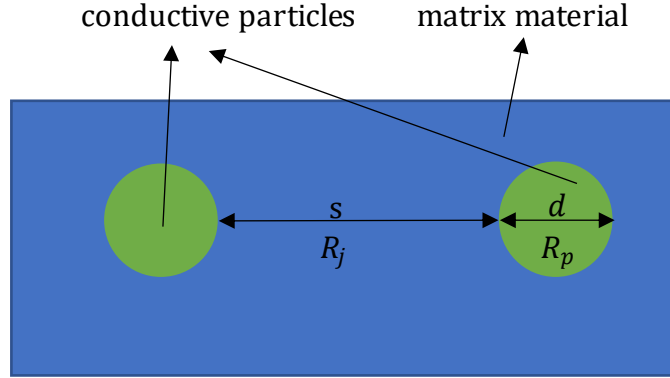


Figure 3.2 Schematic diagram of quantum tunneling variables for adjacent particles

For materials with the same conductive particles and matrix material, a^2 and ψ_p are the same. Hence, the key additional factor determining differences in composite electrical resistivity (as opposed to just that of a single junction) for composites made from the same materials is the distribution of the particles inside the composite. Current models and theories contain two types of assumptions for the particle distribution inside the composite: uniform and non-uniform junction distance distribution.

3.1.1 Uniform junction distance distribution

In the uniform junction distance assumption, the conductive particles are regarded as uniformly distributed in the matrix material [62-70] so that the junction lengths are the same for all the paths. Hence, Equations (3.8) and (3.9) can be combined and simplified as

$$R_{total} = \frac{N_{pp}R_j}{N_{path}} = \frac{N_{pp}}{N_{path}} \frac{8\pi h}{3a^2\Gamma e_0^2} s e^{\Gamma s} \quad (3.10)$$

where Γ is a constant determined by the material properties. N_{pp} is average number of conductive particles forming a path and N_{path} is the number of resistor paths as defined above. As the path is

in axial-direction, N_{pp} is dependent on the number of particles in the axial direction and should be proportional to $\varphi^{\frac{1}{3}}$. Similarly, N_{path} is dependent on particle number in the cross section and should be proportional to $\varphi^{\frac{2}{3}}$. Hence, it is reasonable to assume

$$\frac{N_{pp}}{N_{path}} \approx C_7 \varphi^{-\frac{1}{3}} \quad (3.11)$$

where C_7 is a constant.

The number of particles in a sample, N_p , can be derived as

$$N_p = \frac{V\varphi}{\frac{4}{3}\pi\left(\frac{d}{2}\right)^3} \quad (3.12)$$

where V is the sample volume, φ is the particle volume fraction, and d is the particle mean size (diameter). Considering the particles are assumed uniformly distributed inside the sample, the sample can be regarded as having N_p imaginary contacting spheres with the mean radius of $\frac{s_{sp}}{2}$ packed inside it as illustrated schematically in Figure 3.3.

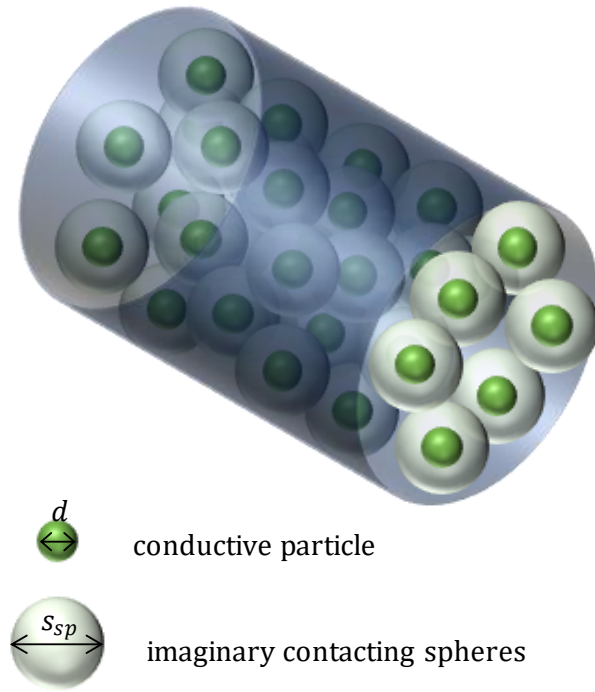


Figure 3.3 Schematic diagram of particle and imaginary contacting spheres inside sample

Hence, N_p can also be derived as,

$$N_p = \frac{V \varphi_{sp}}{\frac{4}{3} \pi \left(\frac{s_{sp}}{2}\right)^3} \quad (3.13)$$

where φ_{sp} is the sphere packing density of the imaginary contacting spheres. The value of φ_{sp} is a constant determined by the arrangement of the particles, which for close packed spheres is given by $\varphi_{sp} = \frac{\pi}{3\sqrt{2}} \approx 0.74048 > \varphi$. As N_p derived from the two equivalent equations, s_{sp} can be determined by eliminating N_p from Equations (3.12) and (3.13):

$$s_{sp} = d \left(\frac{\varphi_{sp}}{\varphi}\right)^{1/3}. \quad (3.14)$$

Hence, the mean junction distance between two adjacent particles can be derived as

$$s = s_{sp} - d = d \left(\left(\frac{\varphi_{sp}}{\varphi} \right)^{\frac{1}{3}} - 1 \right). \quad (3.15)$$

Under the conditions of Equations (3.10) and (3.11), Equation (3.15) indicates that the electrical resistivity is only impacted by the particle size and particle volume fraction when no mechanical load is applied to the material. Though it is possible to measure ψ_p in solids, the method currently used [69] is very complex and expensive. Hence, the two constants C_7 and Γ are determined by fitting Equations (3.10), (3.11), and (3.15) to measured results. The resulting model can describe the material behavior for different particle volume fractions when no mechanical loads are applied. Details are presented in section 3.4.

Based on the assumed behavior, junctions will not appear or disappear when mechanical loads are applied. Only the junction distance is impacted by mechanical loads, which is observed through changes in the electrical resistivity. For a uniform junction distance distribution, the junction distance is the same everywhere in the material and can be regarded as linearly proportional to strain of the material. For uniaxial strain the relationship is

$$s = (1 + \varepsilon)s_0 \quad (3.16)$$

where s and s_0 are the junction distance after and before the mechanical load is applied, ε is the resulting strain of the composite, namely,

$$\varepsilon = \frac{\Delta L}{L}, \quad (3.17)$$

(see Figure 3.4) and the strain is regarded as the same everywhere inside the material.

Combined with Equations (3.10) and (3.11), the assumed strain and junction distance behavior predicts an increasing trend of the electrical resistivity when tension is applied to the material. However, the preliminary tests of ECPC based on two thermo plastic matrix materials (material details are listed in Table 3.1) are the opposite. This uniform junction assumption does not satisfy the material behavior investigated in this work.

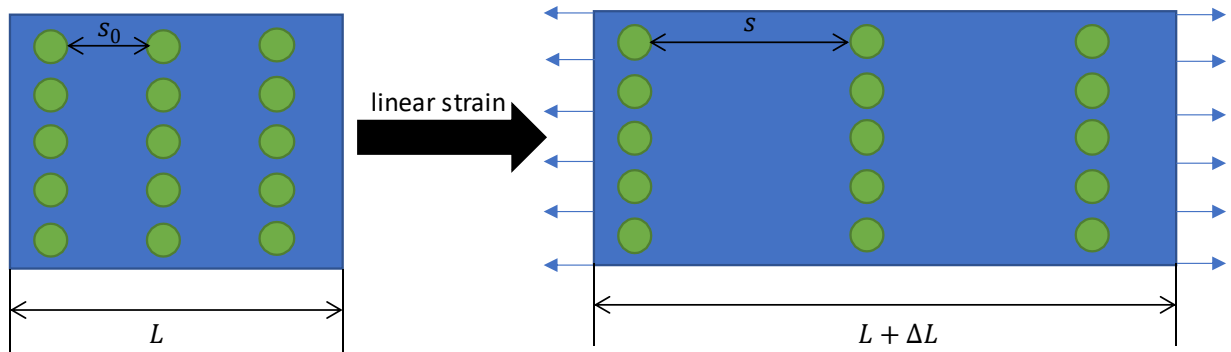


Figure 3.4 Schematic diagram of uniform junction distance distribution under tensile loading

3.1.2 Non-uniform junction distance distribution

In the non-uniform junction distance assumption, the particles are randomly distributed in the matrix material and the junction distance is not uniform. The total material resistance still follows the Equation (3.10) when no mechanical load is applied. However, adjacent particles will move in more complex ways, as illustrated in Figure 3.5, when a mechanical load is applied. The junction distance may be smaller or larger after deformation under load as determined by the original relative position of the particles (relative angle θ and separation s_0), material property (Poisson's ratio μ) and strain ϵ (a detailed analysis is presented in section 3.4). Hence, junctions may lengthen or shorten and the dominant conductive paths in the composite can be rearranged.

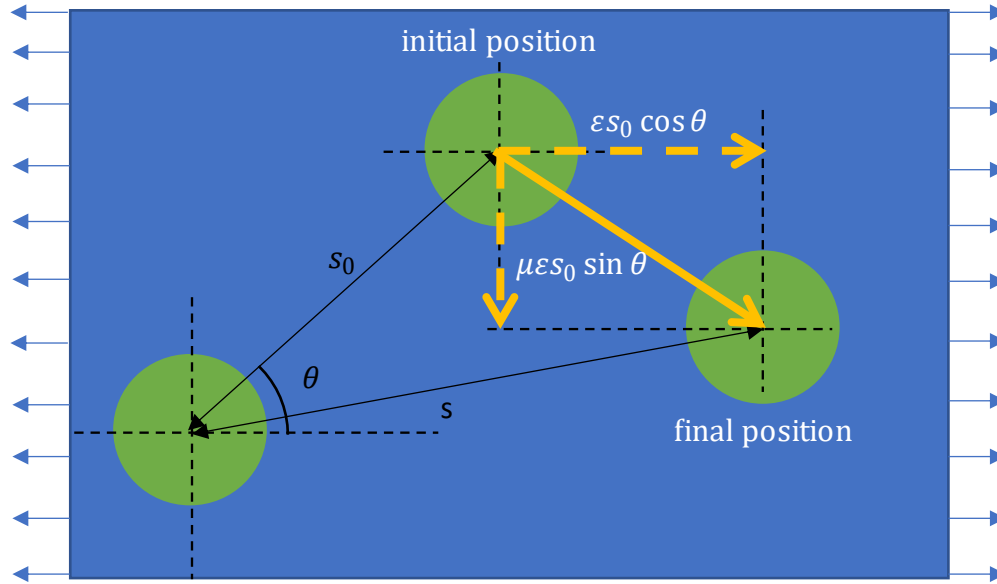


Figure 3.5 Schematic diagram of Relative position of two adjacent particles with tensile loading

Johnson et al. [69] utilized statistical methods to analyze and model the material behavior of non-uniformly distributed particles in ECPC under mechanical load. The junction distance was assumed to be Weibull distributed when no mechanical load was applied. A Monte-Carlo simulation was applied to find the junction distance distribution when a specific strain was applied. Resistivity with an inverse relation to tensile strain was observed based on the new junction distance distribution.

However, this model is inadequate for the conditions of this work. The model was formulated to describe materials with nano-strand conductive elements instead of micro-scale particles. The model cannot explain some dynamic phenomena, such as the decreasing resistivity under viscoelastic stress relaxation observed for some matrix materials, as only uniaxial static strain was considered with no contemplation of stress-strain relationships. More broadly, the model is

complex (e.g., the particle distribution under strain is determined iteratively, so that the connection between particle position and the applied load is implicit), making behavior such as the boundary between positive and negative changes in resistivity relative to applied strain difficult to determine.

3.1.3 Empirical models

In addition to theoretical models, there are also several empirical models for resistivity/conductivity in ECPCs [49-56]. Though some of them can describe the material behavior under some conditions, none can describe the behavior under all types of mechanical loading. Moreover, given the empirical nature of the models, they cannot provide a clear physical explanation of the observed behavior.

The current conditions of models for ECPC motivate an investigation of the resistivity of these types of materials, especially with different mechanical loads applied. Both theoretical analysis and experimental tests for different material formulations and different mechanical loads were conducted and are presented in the following sections.

3.2 Experiment Design and Setup for Electrical Resistivity Measurements

To experimentally quantify the impacts of material composition and working conditions, the resistivity of ECPC with different material formulations and mechanical loading was measured.

3.2.1 Material Selection and Testing Conditions

To quantify the impact of matrix material, two types of matrix material were selected and tested as shown in Table 3.1. The volume fractions of the formulated ECPC materials are also shown in Table 3.1. To attain an accurate model for the composite ECPC material with varied particle volume fraction, the range of tested particle volume fraction was maximized. The lowest particle volume fraction was chosen as the ECPC with highest measurable electrical resistivity. (ECPC with lower particle volume fractions were nonconductive.) The highest particle volume fraction

was chosen as the maximum packing volume fraction (or capacity) for the particle/matrix material combination (no more particles could be added into the composite beyond this point).

Table 3.1 ECPC material option

Conductive Particle	Matrix Material	Particle Volume Fractions (%)
Potters Industry silver coated nickel SN08S40 (mean size = 31 microns, Ag weight fraction = 8%)	Tecbond hot glue adhesive 7718 (referred to as T7718 throughout)	22, 24, 26, 28, 30
	Kraton thermal plastic elastomer G1161 (referred to as TPE throughout)	21, 23, 25, 27, 29

Given the polymer nature of the matrix material and the high loading of the particulate additive, the material behavior can be described by a standard linear viscoelastic model (Maxwell representation) [74] as illustrated in Figure 3.6. The mechanical model for this type of material can be expressed as

$$\sigma + \frac{\eta}{E_2} \dot{\sigma} = E_1 \varepsilon + \frac{\eta(E_1 + E_2)}{E_2} \dot{\varepsilon} \quad (3.18)$$

where σ and $\dot{\sigma}$ are the stress and rate of stress, ε and $\dot{\varepsilon}$ are the strain and rate of strain, E_1 & E_2 are Young's moduli of the spring components, and η is the viscosity of the dashpot (damping) component.

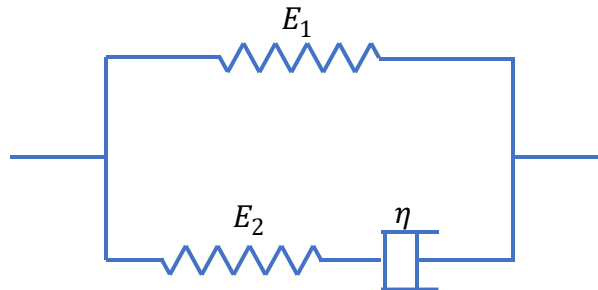


Figure 3.6 Schematic diagram of standard linear viscoelastic model.

For such viscoelastic materials, the nature of the applied stress and/or strain can impact the behavior. For a fixed initial strain, stress is allowed to relax to a steady state (force magnitude is controlled during the process to keep the displacement the same). Alternatively, strain rate can be fixed providing a linear-ramp strain condition. For this investigation, both types of mechanical loading were applied to the sample as described in Table 3.2. These canonical loading conditions provide direct observations of the relationship between resistivity and strain/stress.

Table 3.2 ECPC mechanical loading conditions²

Material	Testing Conditions
Particle: SN08S40 Matrix material: T7718 Particle volume fraction: 30%	Relaxation (strain = 0.00625, 0.0125, 0.025, 0.05)
	Linear ramp (strain rate = $0.00625s^{-1}$)

Two key instruments were used to provide the material behavior information under the desired loading conditions. A Hioki RM7734 multimeter was used to measure the resistance of the material samples. An Instron E1000 was used to apply mechanical loads to the samples. Details of resistance measurements and mechanical loading are presented in section 3.2.2.

² the table indicates the nominal values. The true values are calculated in Section 3.3 and the Appendix for the different samples used.

3.2.2 Experimental Procedure

Sample Fabrication. To prepare the material with the desired particle volume fractions, particles and matrix material quantities were measured with a scale (Cole-Parmer Symmetry EC-Series Portable Top-loading Balance). The materials were heated in a hot pot (RITEHETE 1203.5 VR) to the mixing temperature (210 °C for G1161, 190 °C for T7718) and blended with a mechanical mixer to a uniform state. The materials were extruded using a manual extruder (GALOMB A-100) to obtain a long filament. The filaments were cut into samples of 5 cm length for testing. Sample dimensions and mass were measured after the samples cooled to room temperature. The actual particle volume fraction was calculated from the measured mass and dimensions according to

$$\varphi = \frac{m_s - \rho_m V_s}{(\rho_p - \rho_m) V_s} \quad (3.19)$$

$$V_s = \frac{\pi}{4} D^2 L_0 \quad (3.20)$$

where φ is the particle volume fraction, m_s (measured with the same scale) and V_s are the sample mass and volume, D and L_0 are the sample diameter and length (measured with Mitutoyo 500-197-30 digital calipers), ρ_p and ρ_m are the particle and matrix material density (determined from manufacturer specifications).

Mechanical Loading and Resistance Measurement. Once the test sample was configured, the Instron E1000 clamps were retracted slightly to pre-strain the sample until it was straight and then the mechanical load was applied on the sample. The displacement and force on the sample and the electrical resistance of the sample between the copper wires was recorded automatically every second. For each testing condition, three samples from the same long filament were tested.

To prepare the samples for testing, two copper wires were connected at the ends of the middle third of the sample and the ends were covered with electrical tape as shown in Figure 3.7. Copper wires were utilized to provide conductivity (negligible resistance) between the clamps of the Hioki multimeter and the sample without deforming the sample. Electrical tape applied to the sample ends was used to insulate the samples from the Instron E1000 clamps. Lines on the sample were marked to confirm negligible slipping of the clamps or wires during testing.

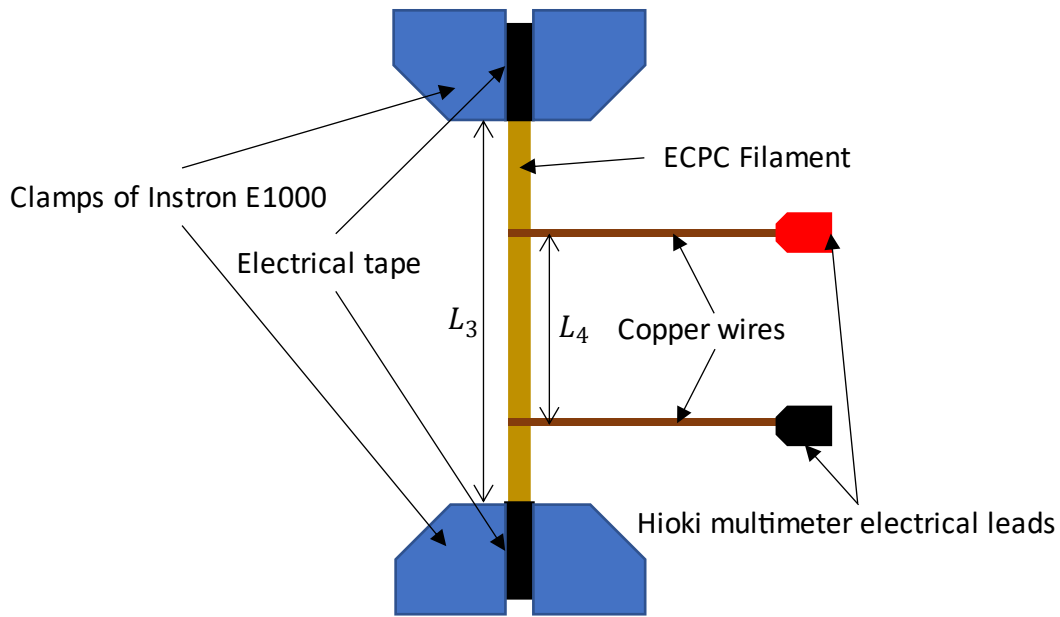


Figure 3.7 Schematic diagram of experimental setup

3.2.3 Resistivity Calculation

Using the measured resistance, displacement, force and dimensions of the sample, the sample stress, strain, and resistivity were determined as

$$\varepsilon = \frac{\Delta L}{L_3}, \quad (3.21)$$

$$\sigma = \frac{F}{A} = \frac{4F}{\pi D^2}, \quad (3.22)$$

and

$$\rho = R \frac{A}{L_4} \quad (3.23)$$

where ε is the normal strain, ΔL is the measured displacement, L_3 is the (initial) sample length between clamps, σ is the normal stress, F is the applied force, ρ is the resistivity, R is the resistance of the sample between the copper wires, A is the cross-section area of the sample, D is the (initial) sample diameter, and L_4 is the (initial) distance between the copper wires. Averages of the results for the three samples tested were used to assess the behavior for each test condition.

3.3 Electrical Conductivity/Mechanical Experiment Results

The results for the ECPC formulations listed in Table 3.1 under the mechanical loading conditions in Table 3.2 are presented in Figure 3.8 and 3.9. The error bars represent the standard deviation of the results over the three tests at each formulation/condition.

From Figure 3.8, it can be found that the resistivity decreases rapidly with increasing the particle fraction as additional conductive paths become present with a higher density of particles in the material. For volume fraction below the lowest values tested, the electrical resistance was too high to measure. For the different matrix materials, the resistivity follows a similar trend, but with different magnitudes.

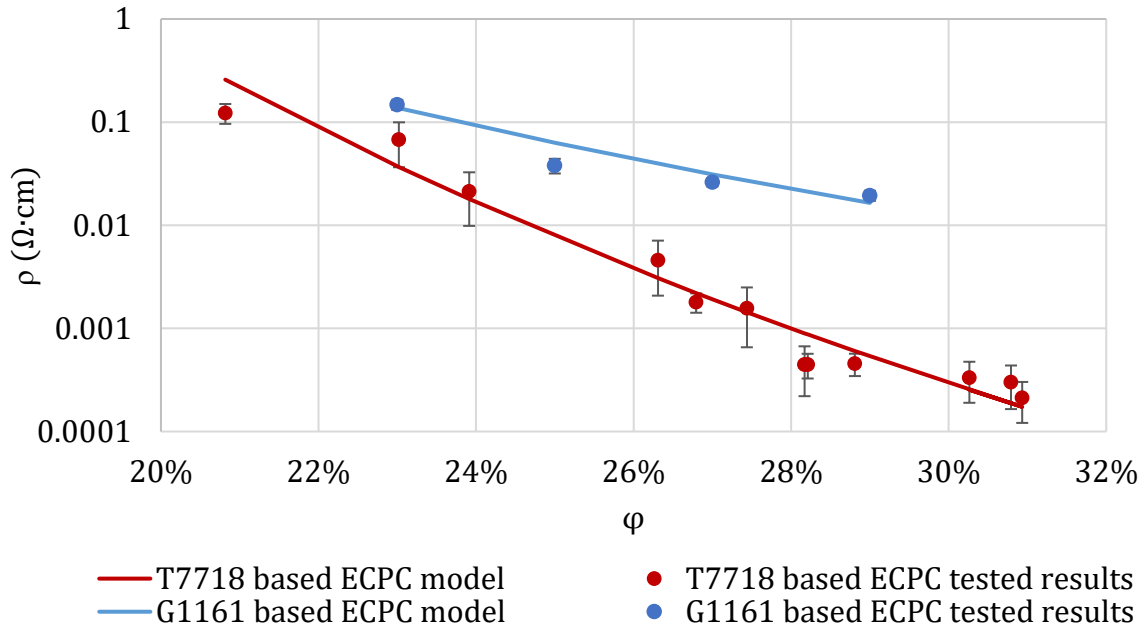


Figure 3.8 Sample electrical resistivity ρ vs. particle volume fraction ϕ at an applied strain of 0.05.

Figure 3.9 shows that the electrical resistivity decreases rapidly both with the linear-ramp tensile strain and during stress relaxation (constant strain). The decreasing rate is larger with the linear-ramp strain than during stress relaxation. The resistivity has larger uncertainties when the strain is smaller (at the beginning of test), but the trends are consistent with multiple applications of the same loading profile.

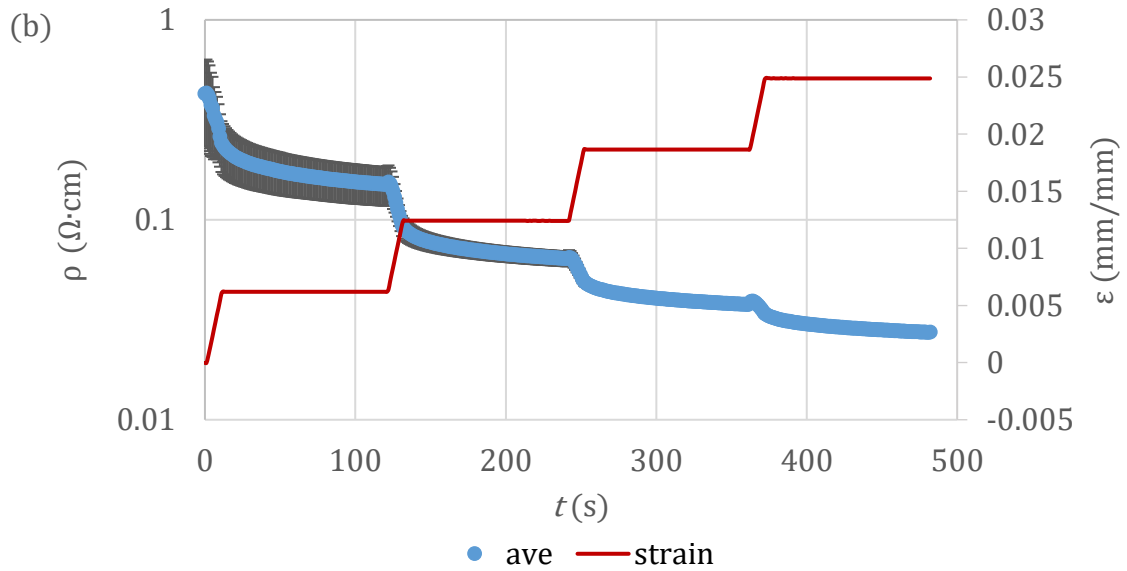
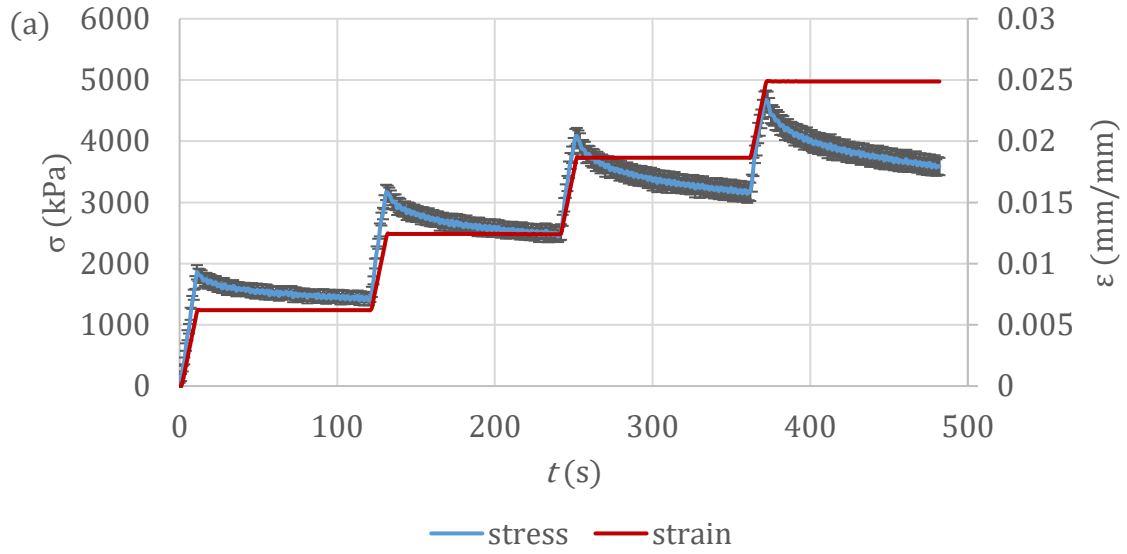


Figure 3.9 Sample strain ϵ (mm/mm) and stress σ (kPa) (a) and electrical resistivity ρ ($\Omega \cdot \text{cm}$) (b) vs. time t (s).

3.4 Electrical Conductivity Data Analysis and Modeling

Following the discussion in section 3.1, the electrical resistivity of the material is determined by the junction distance, number of junctions, and the potential barrier of the matrix material (determined by matrix material only). Junction distance and number of junctions are determined by the particle volume fraction, the mechanical properties of the material, and applied mechanical loads. The mechanical properties are determined by the particle volume fraction, particle type, and matrix material type. However, since the particle in this work is much stiffer than the matrix material, its impact is negligible compared with matrix material. Hence, the particle volume fraction, matrix material type, and mechanical loads are the key factors impacting the material's electrical resistivity. These three factors are analyzed and modeled in this section based on the experimental results of section 3.2.

3.4.1 Particle volume fraction and matrix material

As presented in section 3.1.1, the bulk resistance of a sample can be expressed as Equation (3.10) and (3.11), and the average junction distance between two adjacent particles can be determined from Equation (3.15). Combining these with Equation (3.23), the resistivity of the material can be obtained as

$$\rho_0 = \frac{N_{pp}}{N_{path}} \frac{A}{L_4} \frac{8\pi h d}{3a^2 \Gamma e_0^2} \left(\left(\frac{\varphi_{sp}}{\varphi} \right)^{\frac{1}{3}} - 1 \right) e^{\Gamma d \left(\left(\frac{\varphi_{sp}}{\varphi} \right)^{\frac{1}{3}} - 1 \right)}. \quad (3.24)$$

For the non-uniform junction distance assumption, the behavior of $\frac{N_{pp}}{N_{path}}$ may be more complex, but follows a trend similar to the uniform distance assumption. Considering the particle volume fraction in the experiment only varies from 20% to 30%, the impact of $\frac{N_{pp}}{N_{path}}$ following Equation

(3.11) is negligible, and it will be considered a constant: $\frac{N_{pp}}{N_{path}} = C_8$.

Hence, ρ_0 can be modeled as

$$\rho_0 = C_9 \left(\left(\frac{\varphi_{sp}}{\varphi} \right)^{\frac{1}{3}} - 1 \right) e^{C_{10} \left(\left(\frac{\varphi_{sp}}{\varphi} \right)^{\frac{1}{3}} - 1 \right)} \quad (3.25)$$

with

$$C_9 = C_8 \frac{A}{L_4} \frac{8\pi h d}{3a^2 \Gamma e_0^2} \quad (3.26)$$

and

$$C_{10} = \Gamma d. \quad (3.27)$$

As Γ is determined by the matrix material only, as discussed in section 3.1.1, and the particle mean size is the same for a given material formulation, C_9 and C_{10} can be regarded as constants for the same composite material formulation.

For the material formulations in Table 3.1, a least square fit of Equation (3.25) to the results shown in Figure 3.8 gives the values of C_9 and C_{10} as listed in Table 3.3. Here C_9 and C_{10} are marked as $C_{9,\varepsilon}$ and $C_{10,\varepsilon}$ because resistivity was measured when strain was applied on the sample ($\varepsilon = 0.05$ in this case). The uncertainties were calculated from Jackknife method [106]. The results of this fit are shown in Figure 3.8.

Table 3.3 Constant values in Equation 3.25 for different matrix materials

	$C_{9,\varepsilon} (\Omega \cdot \text{cm})$	$C_{10,\varepsilon} [-]$
T7718 based ECPC	$(4.2 \pm 0.8) \times 10^{-9}$	34.9 ± 1.2
G1161 based ECPC	$(1.5 \pm 0.7) \times 10^{-4}$	15.6 ± 4.9

The reason for measuring resistivity at a fixed strain in Figure 3.8 is due to the sensitivity of the sample resistivity to displacement and force, especially when the applied strain is small and particle volume fraction is low. As it is impossible to eliminate all the forces from the samples during the initial test setup, the resistivity measured with small applied strain varied dramatically, as shown in Figure 3.10. This variation is also observed in the large uncertainties for resistivity at early times (when strain is low) in Figure 3.9 (b). Since more repeatable resistivity results were obtained at larger strains, the measurements in Figure 3.8 and Table 3.3 were obtained before failure with the same strain applied (in the linear ramp portion of the test). Additional details of this behavior are discussed in the next section.

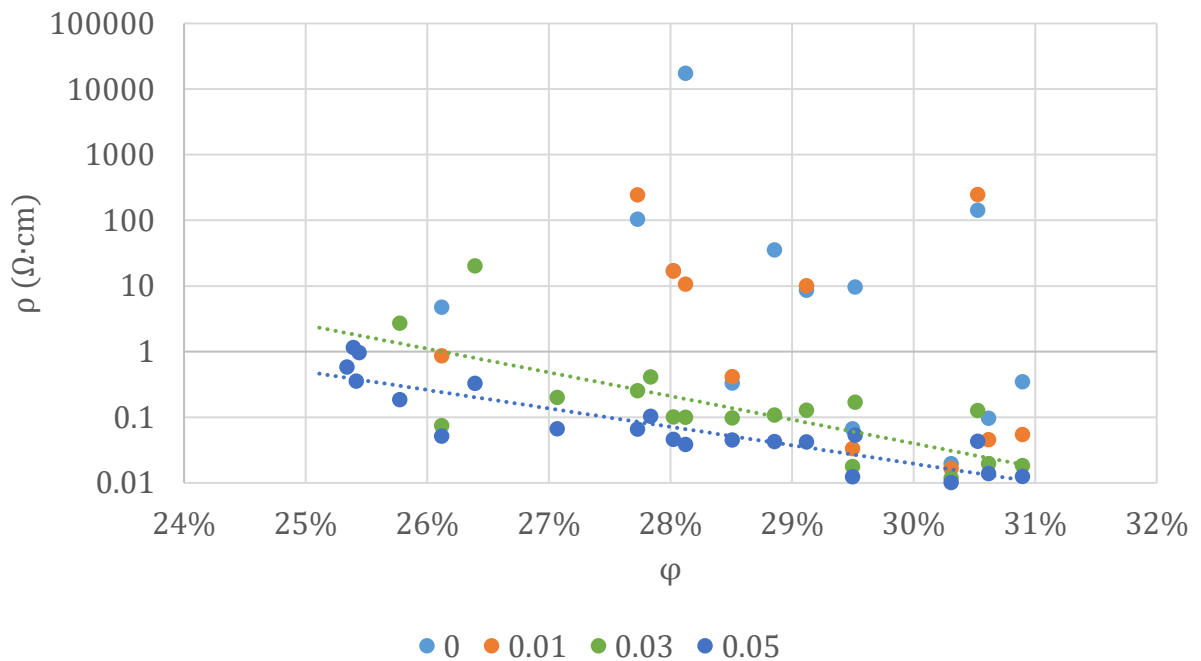


Figure 3.10 Sample electrical resistivity ρ ($\Omega \cdot \text{cm}$) vs. particle volume fraction ϕ (T 7718 based ECPC) with legend indicating applied strain ε . Each point with the same ϕ is from the same sample. At small ε and small ϕ , ρ became too large to be measurable. Dotted lines are trendlines fitting Equation (3.25) for the data with the same color. Trendlines are only shown for data where a clear trend exists.

3.4.2 Influence of Mechanical Loading

Junction distance and number are the key factors impacting the electrical resistivity of the material when mechanical loads are applied. The particles are assumed to have a random distribution inside the matrix material as shown in Figure 3.11 (a). As the junction distances are changing proportional to the strain and the particle network structure does not change topologically (the adjacent particles are still adjacent) with and without mechanical loading before failure, the junction number is regarded as the same during loading. For the same matrix material, the junction distance is the key factor impacting the electrical resistivity under mechanical load.

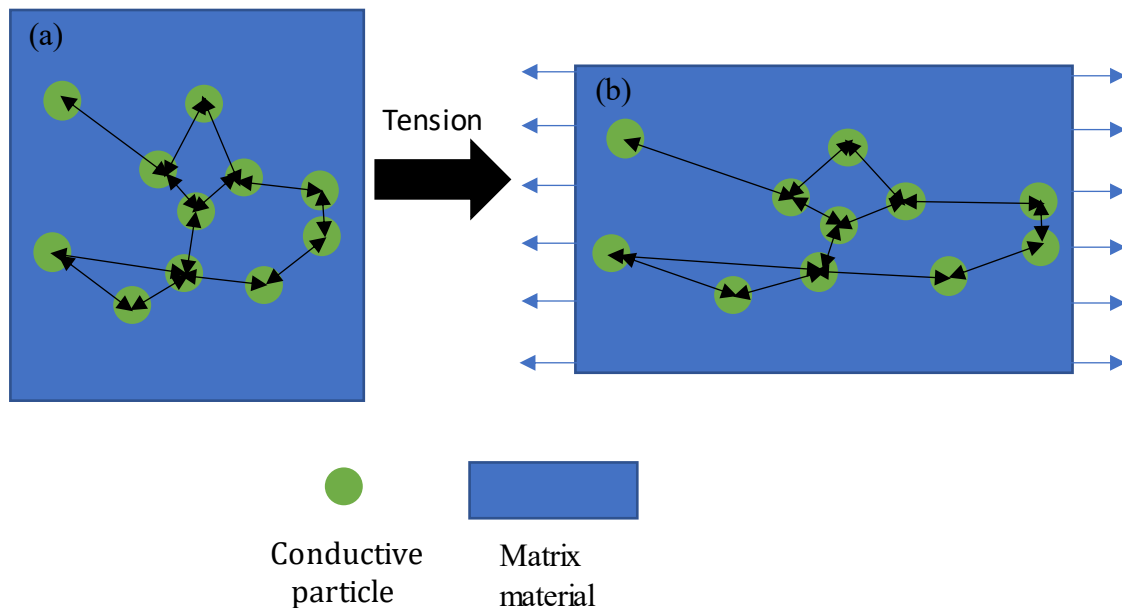


Figure 3.11 Schematic diagram of random junction distances without (a) and with (b) tensile loading

Based on the assumption of unchanged particle network structure, the particle packing structure is the same. Hence, analogous to the approach in section 2.4.4.5, the average junction distance is proportional to the cubic root of the material volume, namely

$$\frac{s}{s_0} = \left(\frac{V}{V_0}\right)^{\frac{1}{3}} \quad (3.28)$$

where s and V are the average junction distance and the sample volume and s_0 and V_0 are the corresponding values with no load applied. Under load, the material deformation dictates [94]

$$\frac{V}{V_0} = (1 - \mu\varepsilon)^2(1 + \varepsilon) \quad (3.29)$$

where ε is the strain of the material, and μ is the Poisson's ratio of the material. Combining Equation (3.29) with Equation (3.10), the bulk electrical resistivity of the material can be modeled as

$$\frac{\rho}{\rho_0} = \frac{s}{s_0} e^{C_{11}\left(\frac{s}{s_0}-1\right)} \quad (3.30)$$

where

$$\frac{s}{s_0} = \sqrt[3]{(1 - \mu\varepsilon)^2(1 + \varepsilon)} \quad (3.31)$$

and $C_{11} = \Gamma s_0$ is a constant for a given material formulation.

Given the viscoelastic behavior of the material, described in Equation (3.18), both μ and ε can change when mechanical loads are applied. Based on the Equations (3.30) and (3.31), the behavior of bulk electrical resistivity as a function of μ and ε is shown in Figure 3.12. Domains of both increasing and decreasing resistivity exist, with trends determined by the relative values of μ and ε .

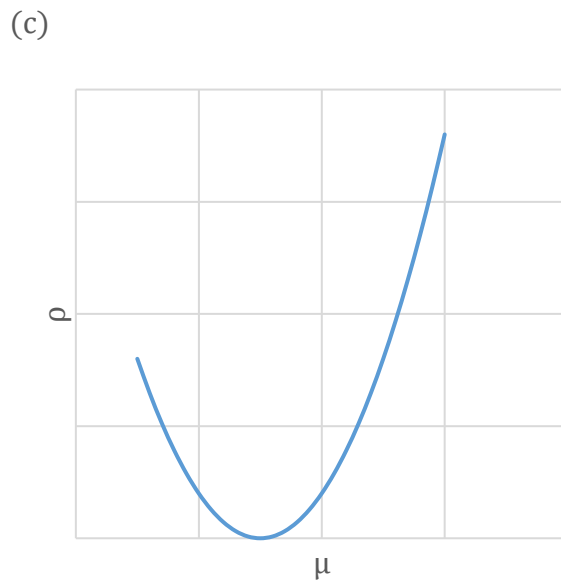
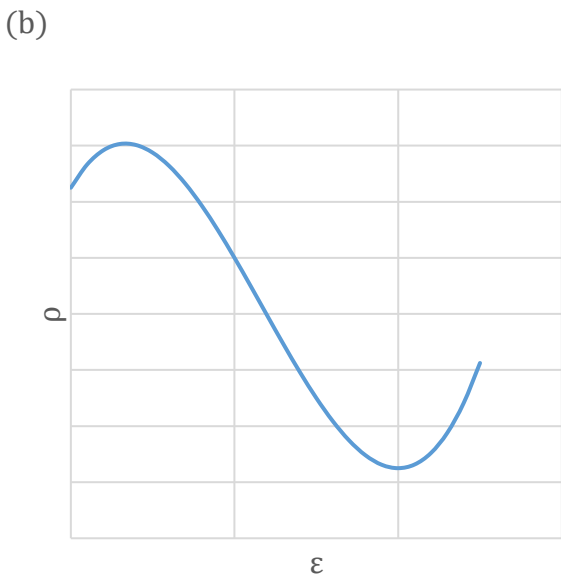
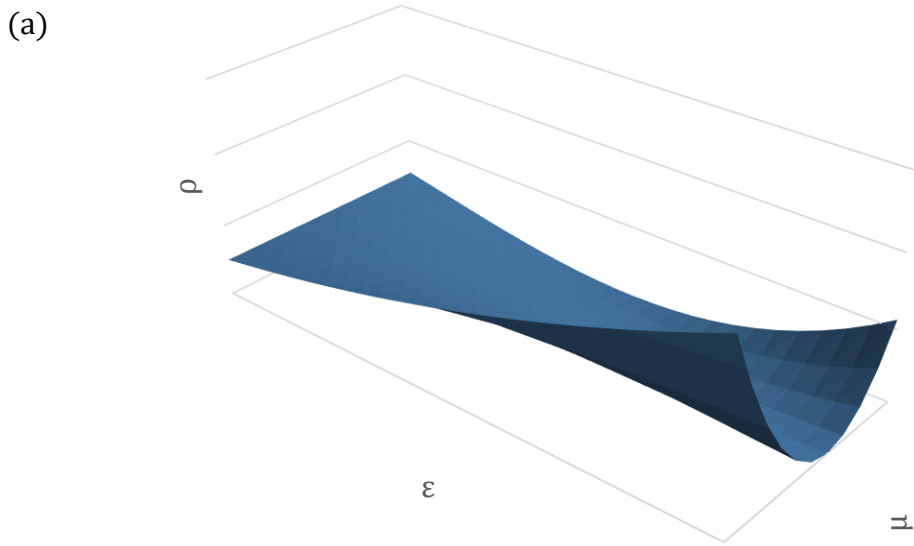


Figure 3.12 Resistivity ρ vs. strain ε and Poisson's ratio μ (a) Resistivity ρ vs. strain ε with Poisson's ratio as a constant (b) and Resistivity ρ vs. Poisson's ratio μ with strain ε as a constant (c)

The relation between the μ and the applied mechanical load is complex and time dependent for a Maxwell viscoelastic material, as described and modeled in several investigations [98, 99, 100]. To simplify the derivation and analysis, the condition of linear-ramp strain and stress relaxation were chosen to demonstrate the behavior. In this case, Poisson's ratio can be modeled as

$$\mu = \frac{1}{2} - \frac{E}{6B} \quad (3.32)$$

where E is the Young's modulus and B is the bulk modulus, which can be regarded as a constant. The value of B can be measured from standard experiments, however, here it is taken as 2.8×10^7 kPa, which is in the middle of the datasheet range for the matrix material used (T 7718). More accurate model results may be achieved with a more accurate value for the bulk modulus.

Under conditions of linear-ramp strain, stress was linearly proportional to strain as shown in Figure 3.13. Thus, E can be regarded as a constant under these conditions. During stress relaxation, on the other hand, Young's modulus can be determined as [94]

$$E = \frac{\sigma}{\varepsilon_0} \quad (3.33)$$

where σ is the stress in the sample and ε_0 is the fixed strain during stress relaxation.

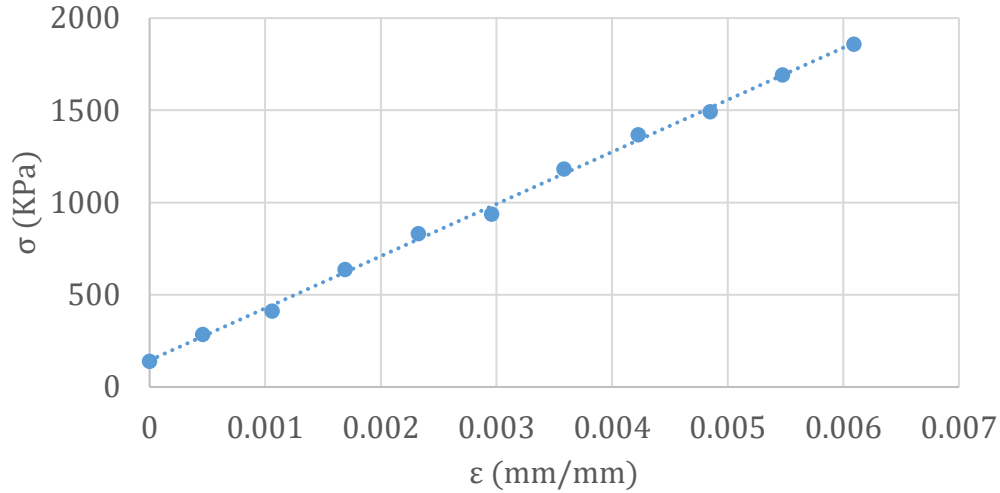


Figure 3.13 stress σ (kPa) vs. strain ϵ (mm/mm) with linear-ramp strain.

Applying the strain conditions indicated in Table 3.2 to Equations (3.30) to (3.31), the constant values in the equations can be determined from a least square fit of the corresponding experimental measurements as $C_{11} = (2.3 \pm 0.4) \times 10^5 [-]$ and $\rho_0 = 0.4 \pm 0.2 \Omega \cdot \text{cm}$. Here $C_{11} = C_{10} \left(\left(\frac{\varphi_{sp}}{\varphi} \right)^{\frac{1}{3}} - 1 \right)$ can be derived using Equation (3.15) to determine s_0 . The value of $\frac{C_{11}}{C_{10}}$ should be close to $\left(\frac{\varphi_{sp}}{\varphi} \right)^{\frac{1}{3}} - 1 \approx \left(\frac{0.74}{0.3} \right)^{\frac{1}{3}} - 1 \approx 0.35$. However, a large difference exists between the C_{11} calculated here and the C_{10} calculated in Section 3.4.1. These differences may result from different fit conditions as $\epsilon = 0.05$ was applied on the sample in Section 3.1. In particular, s_0 in Equation (3.31) is a reference value (corresponding to ρ_0) and may not be given directly by Equation (3.15). Additionally, the difference may be influenced by the bulk modulus as an approximate value was used and the model is very sensitive to bulk modulus. The uncertainties are the standard deviations

of the three tests. The results of this fit are shown in as Figure 3.14 together with the measured resistivity.

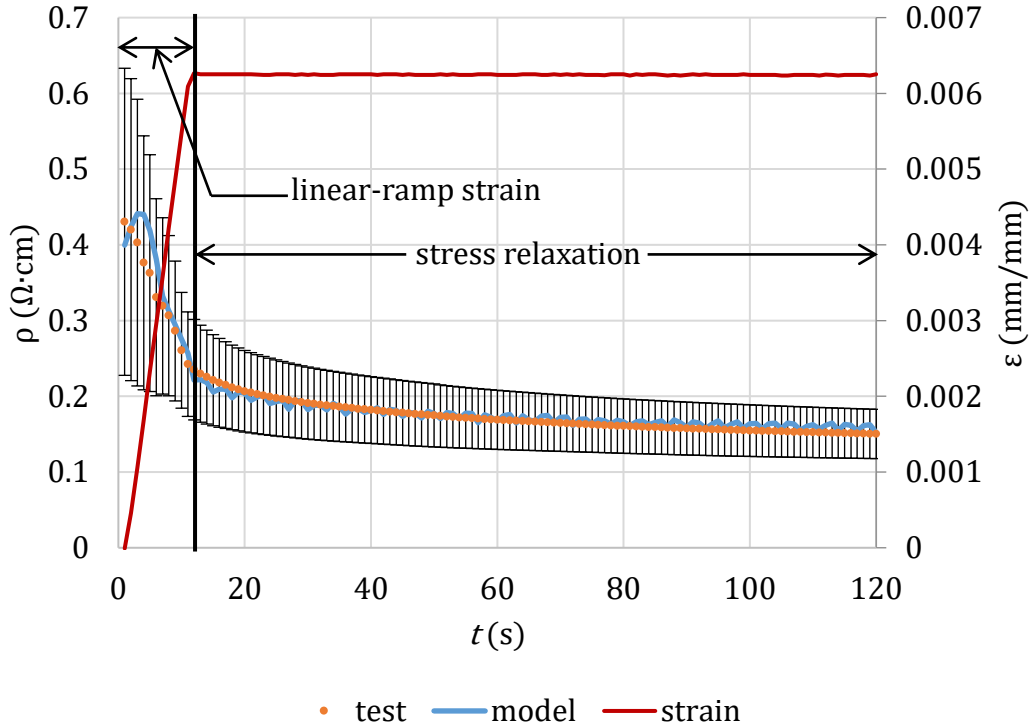


Figure 3.14 Tested/modeled resistivity ρ and strain ε vs. Time t (s)

The resistivity model predicts the correct trend and has an error smaller than 5% for the stress relaxation phase and most of the linear-ramp strain phase. The key difference between the model and measured results is the increasing/decreasing trend of resistivity at the start of the linear-ramp strain. To guarantee the sample was straight when testing, a small pre-strain was applied before the test started. As the electrical resistivity is sensitive to the strain especially when the strain is small, the pre-strain may generate a large variance and miss the increasing stage at the start of

linear-ramp strain. Figure 3.15 demonstrates the existence of increasing trend at the start of the linear-ramp strain when pre-strain was not applied (or was too small).

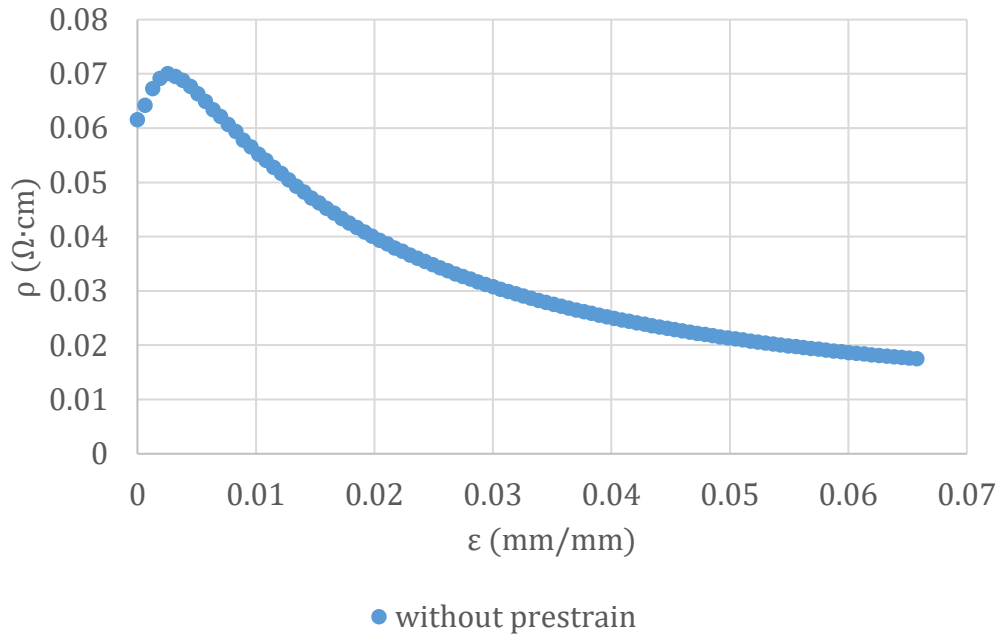


Figure 3.15 Resistivity ρ vs. strain ϵ when pre-strain was not applied (or too small)

3.5 Electrical Conductivity Experiment Results

In this chapter, current theories for electrical resistivity of conductive particulate composite were reviewed and compared. The importance and necessity of investigating the electrical resistivity of ECPC further was presented. Experiments were designed and conducted to investigate the resistivity of ECPC with two matrix materials over a range of particle volume fractions under different mechanical loading conditions (using uniaxial tension as an example). Theoretical analyses were conducted based on tested data and reasonable assumptions. Combining

the models presented above, the bulk electrical resistivity of ECPC with different particle volume fraction under mechanical load can be modeled as

$$\rho = C_9 H_\varphi H_s e^{C_{10} H_\varphi H_s} \quad (3.34)$$

$$C_9 = \frac{A}{L_4} \frac{N_{pp}}{N_{path}} \frac{8\pi h}{3a^2 \Gamma e_0^2} d \quad (3.26)$$

$$C_{10} = \Gamma d \quad (3.27)$$

$$H_\varphi = \left(\frac{\varphi_{sp}}{\varphi} \right)^{\frac{1}{3}} - 1 \quad (3.35)$$

$$H_s = \frac{S}{S_0} = \sqrt[3]{(1 - \mu\varepsilon)^2 (1 + \varepsilon)} \quad (3.36)$$

where C_9 and C_{10} can be obtained from fits to the experimental results. Based on the experiments, it can be concluded that the above models can describe the electrical resistivity behavior well for conductive particulate composites with viscoelastic matrix materials when the strain is small ($\varepsilon \leq 0.05$). Differences between the model and tested results were presented, with sensitivity to pre-strain of the material having a strong effect on variability of the experimental results at low strain.

CHAPTER 4 SUMMARY AND RECOMMENDATIONS

4.1 Conclusion

Particulate composites are one of the key solutions to satisfy different functional requirements in AM. Challenges exist to utilizing this type of material for AM. Key among them are avoiding capillary blocking and maintaining flow behavior to improve manufacturing efficiency. Based on the experience from FEAM, the rheology of particulate composites in the liquid-phase (also known as particulate suspensions) during the AM process is the key feature. Another important and interesting characteristic is the electrical conductivity of particulate composites containing after manufacturing when the particles are electrically conductive. Both rheology and electrical conductivity of particulate composites were investigated experimentally and theoretically in this work.

4.1.1 Rheology

In AM, the matrix materials (suspension fluids) used in particulate composites are mainly polymers and silicone, which are shear thinning non-Newtonian fluids. The particles are typically spheres with diameters on the order of 10s of μm . Extruding nozzles can be regarded as (short) capillaries with ID on the scale of generally 10s to 100s of μm . Materials and geometries within these scale ranges were the focus of this work. Particle volume fraction, the ratio of capillary ID to particle mean size, and suspension fluid type were found to be the key factors impacting the suspension rheology. Particle size distribution is also appeared to have an impact.

Prior work with suspensions in confined tubes is lacking, but there is significant literature on viscosity modifications in particulate suspensions broadly. Existing viscosity models for particulate suspensions with Newtonian suspension fluids were reviewed [24-39]. These models concentrate on the influence of particle volume fraction. Models were also reviewed for the

suspensions with non-Newtonian suspension fluids [40-45]. However, these models were based on measurements using questionable methods and did not consider the impact of confined geometries such as flow in capillary tubes. Jamming (capillary blockage) was also discussed in some investigations [75-78], but the investigated suspension fluids were not shear thinning. In general, the existing literature covers some aspects of particulate suspension rheology, but it is not sufficient to build a robust model for conditions relevant in AM.

To quantify the impacts for the required materials under the required conditions, experiments were designed and conducted. A capillary rheometer with replaceable capillaries was built to mimic the flow in AM extrusion nozzles. Reasonable materials were selected to generate a comprehensive description of the flow. Due to the power-law nature of the resulting suspension flows, the flow behavior and consistency indices were chosen to quantify the rheology under different conditions.

The experimental results showed that the flow behavior index, n , was dependent on the particle volume fraction, φ , and the suspension fluid flow behavior index, n_f . An empirical equation was generated to describe the linear relationship between n and φ (Equation (2.8)) and provided acceptable accuracy as shown in Figure 2.8.

The experimental results for the flow behavior index, K , were more complex. This parameter was found to depend on the suspension fluid properties (K_f and n_f), φ , and the ratio of capillary ID to the particle mean diameter (ω). The particle size distribution also appeared to have a weak effect. As shown in Figure 2.6 (a) and 2.7 (a), the behavior of K with ω appeared to have a similar trend for all φ . Using this observation, flow behavior was categorized into two conditions: the free flow condition (K increases with increasing ω for $\omega > \omega_{pic}$ and eventually becomes constant

at large ω) and the particle interaction condition (K increases with ω decreasing for $\omega < \omega_{pic}$ and $K \rightarrow \infty$ as $\omega \rightarrow \omega_{jc}$).

The boundaries between the two flow conditions, ω_{pic} , was identified from the experimental results and was observed to increase with increasing φ . A model for ω_{pic} was developed based on the number of particles in the cross section of the capillary, which is determined by φ . Hence, a semi-empirical model of ω_{pic} was derived as a function of φ . Based on the model, the expected flow condition of the selected material formulation and capillary ID can be determined.

For the behavior of K under the different flow conditions, φ and ω were found to be the key factors impacting K based on the experimental results. For the free flow condition, K increased with increasing ω , starting from $\omega = \omega_{pic}$. The rate increase of K with ω decreased for larger ω and eventually a constant K was measured. With φ increasing, K followed the same trend as with ω , but started from and arrived at larger values and exhibited a faster rate of change with ω . A semi-empirical model was developed to describe the dependence of K on ω and φ . The model was based on a statistical analysis of particle location coupled with the assumption that particles closer to the wall have a stronger influence on the rheology. It described the flow behavior with acceptable accuracy as shown in Figure 2.24. Discrepancies between the model and measurements were explained by model simplifications including neglecting polydisperse particle distributions and ignoring complicated relationships between particles such as “sheltered” and “adjacent” particle configurations. For the particle interaction condition, K increased with decreasing ω for $\omega < \omega_{pic}$ and $K \rightarrow \infty$ as $\omega \rightarrow \omega_{jc}$. With larger φ , the observed trend was stronger (i.e., more rapid changes with ω). Because of insufficient theoretical foundation and data, K for this flow condition was modeled empirically with a power-law based equation to capture the features. The model

described the flow behavior with acceptable accuracy for the results in this investigation, as shown in Figure 2.30. Semi-empirical arguments were used to capture expected behaviors such as $\omega_{jc} \rightarrow 1$ as $\varphi \rightarrow 0$ and $\omega_{jc} \rightarrow \infty$ as $\varphi \rightarrow \varphi_M$. Differences between the model and measured K at similar ω appeared to be larger when the particle size distribution was wider. A possible explanation is that the larger particles dominate the interaction among the particles. Jamming was also investigated. The most important parameter describing jamming is ω_{jc} . It was identified from the experimental results and observed to increase with increasing φ . Similarities between jamming and the particle interaction condition were discussed as the particle clustering results from the particle interaction. Hence, jamming has a higher probability for the same ω with a larger particle size distribution.

Utilizing the obtained models in AM applications, the manufacturing process can be improved. Based on the requirements of accuracy and the particle volume fraction of the particulate composites (which is determined by the required properties such as the electrical conductivity described in the next section), the extruder nozzle ID and particle mean diameter can be optimized. Jamming can be avoided by keeping the ratio of extruder nozzle ID to the particle mean diameter always larger than ω_{jc} for the choosing particle volume fraction. Relatively small extruding force can be achieved by keeping the ratio close to ω_{pic} . The repeated work caused by the jamming and unsatisfied material properties can be avoided, and the manufacturing efficiency can be improved.

4.1.2 Electrical Conductivity

Electrical conductivity is an important requirement when printing components with electrical circuits in FEAM. ECPC (one type of conductive particulate composite) was explored as an option to provide conductive junctions between different conductive fibers and other electrical

components. Interesting electrical behavior was observed for several ECPC formulations, which can be characterized in terms of, electrical resistivity (the inverse of conductivity).

Current theories for electrical resistivity of conductive particulate composites were reviewed. A key element of many models is the incorporation of quantum tunneling effects to describe electrical conductivity between particles based on particle separation by a thin layer of matrix material. Existing models provided a good explanation of the resistivity dependence on particle volume fraction and can include effects of matrix material type. However, the impact of mechanical loads, especially under stress relaxation, was not adequately addressed in existing models.

Experiments were designed and conducted to investigate the resistivity of ECPC with two matrix materials over a range of particle volume fractions. Uniaxial tension was selected to provide linear-ramp strain and stress relaxation to illustrate the materials' electrical behaviors under mechanical load.

From the experiment results, the general effect of particle volume fraction was explained well using the existing models based on quantum tunneling effects. Combining parameters in the equations, a semi-empirical equation was derived to describe and predict the dependence of electrical resistivity on φ .

The resistivity with mechanical loading was analyzed based on the average junction distance between adjacent particles. To relate the micro-scale junction distance with the macro-scale measurable parameters, the average junction distance was modeled as proportional to the cubic root of material volume as in Equation (3.14). The volume change with mechanical loading was modeled with Poisson's ratio and applied strain as in Equation (3.15). Combining these

modifications with the resistivity model using quantum tunneling effects provided a general equation for resistivity under mechanical loads (Equation (3.16)). Experiment results with linear-ramp strain and stress relaxation were well-described by the model.

While the model captured the observed trends, a large variance in measured resistivity was found at the beginning of the tests. Additionally, resistivity results for small strain levels showed wide variability. These characteristics are also captured by the model which shows relatively large sensitivity when the strain is small. Additionally, although not observed in the present experiments, the model also captures some other trends reported by some other investigations [46-74], such as decreasing resistivity with increasing compression, increasing resistivity with increasing tension, etc. This model can help predict the electrical behavior of conductive particulate composites broadly.

In AM, once the required electrical resistivity or the required electrical resistivity change with required mechanical loads is determined, the model can be used to determine the composite formulation without minimal preliminary tests. By balancing the material formulation with the manufacturing process requirements as describe in Section 4.1.1, both the manufacturing efficiency and the manufactured product quality can be improved. The model can also be used to predict performance in different use scenarios.

4.2 Recommendation and Future Work

Following the observations and conclusions from the work presented, there is still room for future work to help broaden and improve the results.

4.2.1 Rheology

Additional results with a broader range of materials will provide additional information to help refine the model. For example, the current method to calculate ω_{pic} was approximated from the intersection of two trendlines as presented in Section 2.4.3.5. Better results can be obtained with more tests around current approximated ω_{pic} , which can be achieved by more capillary ID and particle mean diameter options. Additionally, ω_{jc} was calculated by a least square fit as presented in Section 2.4.4.1. Collecting more data near ω_{jc} can improve the analysis. Additionally, the impact of the particle size distribution was analyzed for the particle interaction and jamming conditions qualitatively. More tests with particles of different particle size distribution may be necessary and worthwhile to quantify this impact.

The particle interaction condition was modeled empirically. A more theoretical approach would be valuable for strengthening the model predictions. Here, visualization of particle interaction may be helpful together with theoretical analysis of small clusters of particles in confined spaces [89].

4.2.2 Electrical Conductivity

In the model, particle mean size was a key factor impacting the resistivity. However, no experiment was conducted to check the impact of this parameter because of material limitations. Particle size distribution may also impact the resistivity. Both effects are worth being quantified.

In the comparison of the resistivity model with experiment results under mechanical load, the bulk modulus in the model was estimated from a range of values in the material datasheet. A more accurate value may be obtained measurements of the material, which may improve the model accuracy. Additionally, Poisson's ratio was determined by the bulk modulus and Young's modulus. following Equation (3.17). Complex relations between the mechanical properties of the

composite and its component formulation exist [100-105]. A more comprehensive model may be appropriate for different material formulations.

Finally, only tension was applied to evaluate the resistivity model under mechanical load. Different mechanical loads such as compression and bending may be applied to the sample to evaluate and refine the model.

4.2.3 Other properties

Besides the two investigated aspects of particulate composite, there are also some other aspects worthwhile investigating.

As discussed in Section 2.2, silicone was used to avoid the thermal impacts during experiments. Thermal impact is an important factor in AM. The material may expand or shrink with temperature changes. Additionally, the rheology can change spatially with spatial temperature gradients and the melting and solidification process can impact the particle arrangement in the material. These effects can influence the material rheology during printing and its final electrical properties. It is worthwhile investigating how thermal conditions may impact the composites' behavior during AM processes.

Additionally, the particles used in the work were spherical. Short fibers may be used in the composite to improve the strength and other mechanical properties. Particles with other shapes may also be used to provide anisotropic properties and/or high electrical conductivity at lower φ . The orientation of non-spherical particles may also impact the suspension rheology. It is worthwhile investigating how different shapes impact in all those areas.

Finally, this work was inspired by extrusion-based additive manufacturing and are supposed to help improve the AM efficiency and quality as discussed in Section 4.1. The models for both

rheology and electrical conductivity were established to achieve the goal. However, they have not been utilized in AM yet. It is important and worthwhile utilizing the models in AM to manufacture some products and estimate the improvement of the models by comparing the manufacturing process with the prediction from the rheology model and comparing the manufactured products made of ECPC with the electrical resistivity model.

APPENDIX

A.1 Steady state, repeatability and accuracy in rheology experiments

In the rheology experiments, the steady state was judged by the slope of measured pressure drop ΔP_m vs. time t_m . If the absolute value of the slope was smaller than 7 Pa/s for more than 30 seconds, the flow was considered steady state.

Five tests were repeated with the same experimental settings (the same material, capillary, and flow rate) as discussed in section 2.2.4. The average pressure drop $\overline{\Delta P_m}$ and the standard deviation σ_m of the five tests were used to judge the repeatability of the experiment. In this work, all tested data satisfy a repeatability of $\frac{\sigma_m}{\overline{\Delta P_m}} \leq 0.05$.

When the measured pressure was too low (≤ 55 kPa), the data collected were not accurate because of limitations of the pressure transducer and linear stage/driving system accuracy. Data for these conditions were not included in the rheology analysis. Five flow rates were tested for each material combination. After excluding inaccurate data, data for a minimum of five flow rates was retained in all cases and for the majority (82%), data for all five flow rates were retained.

A.2 Power-law Applicability

To illustrate the applicability of the power law model to the materials tested, an example case with UV 225-1 and A3000 particles at $\varphi = 40\%$ having the data shown in Table A.1 is chosen. Flow rate Q was controlled, and ΔP was measured for each Q . As discussed in section 2.2, the flow behavior index n can be calculated numerically using

$$\tau_w = \frac{R}{2L} \Delta P \quad (2.2)$$

$$n = \frac{d(\ln(\frac{Q}{\pi R^3}))}{d(\ln(\tau_w))} \quad (2.3)$$

$$\dot{\gamma} = \frac{du}{dr_w} = \frac{4Q}{\pi R^3} \left(\frac{1}{4}n + \frac{3}{4} \right) \quad (2.4)$$

The results obtained from these equations for τ_w , n , and $\dot{\gamma}$ are listed in Table A.1. The results for n are similar for all cases. A log-log plot of the data for τ_w vs $\dot{\gamma}$ shows a power-law relation as illustrated in Figure A.2.

Table A.1 Tested and calculated data of experiment with the capillary of $D = 0.6096 \text{ mm}$ and $L = 101.6 \text{ mm}$ and the suspension made of UV 225-1 and A3000 $\varphi = 40\%$

Q (mL/min)	0.025	0.0125	0.00625	0.003125	0.0015625
ΔP (Pa)	1703142	1015280	601815	367600	238214
τ_w (Pa)	2554.71	1522.92	902.724	551.402	357.321
n	0.7463	0.7504	0.73283	0.66853	0.62588
$\dot{\gamma}$	17.5468	8.78298	4.37092	2.14781	1.06142

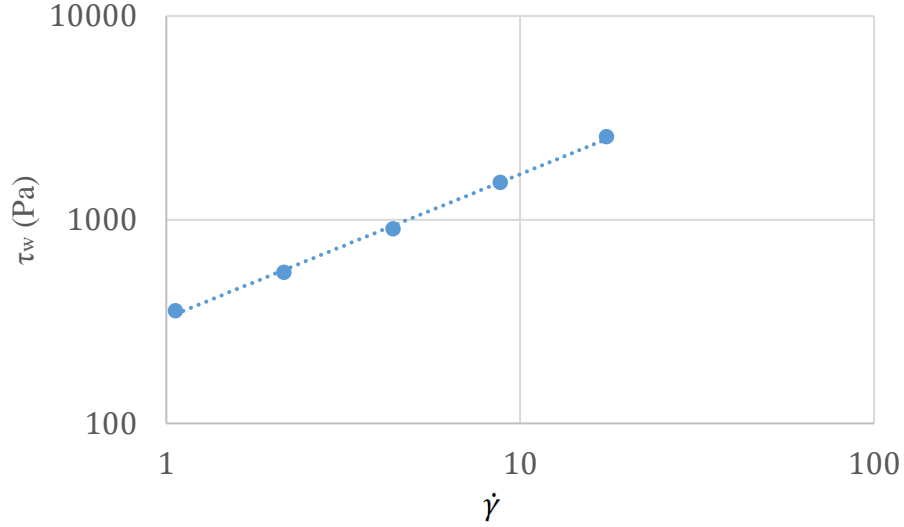


Figure A.1 Shear stress τ_w vs. shear rate $\dot{\gamma}$ for the experiment of Table A.1. The dotted line is a power-law trendline from least square fit.

A.3 Determination of rheology constants

Recognizing the power-law relationship between τ and $\dot{\gamma}$, the shear stress can be modeled as

$$\tau = K\dot{\gamma}^n \quad (2.6)$$

with K and n constant. Substituting Equations (2.2) and (2.4) into Equation (2.6), the relationship between Q and ΔP can be derived as

$$\frac{R}{2L}\Delta P = K \left(\frac{4Q}{\pi R^3} \left(\frac{1}{4}n + \frac{3}{4} \right) \right)^n. \quad (A.1)$$

Taking the natural logarithm of both sides and simplifying gives a linear relationship between $\ln(\Delta P)$ and $\ln(Q)$ as

$$\ln(\Delta P) = n \ln(Q) + \ln \left(\frac{2L}{R} \left(\frac{n+3}{\pi R^3} \right)^n K \right). \quad (A.3)$$

Thus, n and K can be derived as

$$n = \frac{d(\ln(\Delta P))}{d(\ln(Q))} \quad (\text{A.4})$$

$$K = \frac{e^{\beta} R}{2 \left(\frac{n+3}{\pi R^3} \right)^n L} \quad (\text{A.5})$$

where $\frac{d(\ln(\Delta P))}{d(\ln(Q))}$ is the slope of the linear trendline of $\ln(\Delta P)$ vs. $\ln(Q)$, and β is the y-intercept of the linear trendline of $\ln(\Delta P)$ vs. $\ln(Q)$.

Equations (A.4) and (A.5) were utilized to calculate n and K in this work. Following it, $n = 0.71$, and $K = 288.10 \text{ Pa} \cdot \text{s}^n$ are obtained following the example data shown in Table A.1 based on the slope and y-intercept of the least square best fit line for the data.

BIBLIOGRAPHY

- [1] Huang, Samuel H., et al. "Additive manufacturing and its societal impact: a literature review." *The International Journal of Advanced Manufacturing Technology* (2013): 1-13.
- [2] Gibson, Ian, David W. Rosen, and Brent Stucker. *Additive manufacturing technologies*. Vol. 238. New York: Springer, 2010.
- [3] Gao, Wei, et al. "The status, challenges, and future of additive manufacturing in engineering." *Computer-Aided Design* 69 (2015): 65-89.
- [4] Wohlers, Terry. *Wohlers report 2016*. Wohlers Associates, Inc, 2016.
- [5] Attaran, Mohsen. "The rise of 3-D printing: The advantages of additive manufacturing over traditional manufacturing." *Business Horizons* 60.5 (2017): 677-688.
- [6] Jiang, Ruth, Robin Kleer, and Frank T. Piller. "Predicting the future of additive manufacturing: A Delphi study on economic and societal implications of 3D printing for 2030." *Technological Forecasting and Social Change* 117 (2017): 84-97.
- [7] Wong, Kaufui V., and Aldo Hernandez. "A review of additive manufacturing." *ISRN Mechanical Engineering* 2012 (2012).
- [8] Saari, Matt, et al. "Fiber encapsulation additive manufacturing: An enabling technology for 3D printing of electromechanical devices and robotic components." *3D Printing and Additive Manufacturing* 2.1 (2015): 32-39.
- [9] Ott, Michael, and M. F. Zaeh. "Multi-material processing in additive manufacturing." *Proceedings of the Solid Freeform Fabrication Symposium*. 2010.

- [10] MacDonald, Eric, and Ryan Wicker. "Multiprocess 3D printing for increasing component functionality." *Science* 353.6307 (2016): aaf2093.
- [11] Espalin, David, et al. "Multi-material, multi-technology FDM: exploring build process variations." *Rapid Prototyping Journal* 20.3 (2014): 236-244.
- [12] Kokkinis, Dimitri, Manuel Schaffner, and André R. Studart. "Multimaterial magnetically assisted 3D printing of composite materials." *Nature communications* 6 (2015): 8643.
- [13] Miriyev, Aslan, Kenneth Stack, and Hod Lipson. "Soft material for soft actuators." *Nature Communications* 8 (2017).
- [14] Wehner, Michael, et al. "An integrated design and fabrication strategy for entirely soft, autonomous robots." *Nature* 536.7617 (2016): 451-455.
- [15] Sun, Ke, et al. "3D printing of interdigitated Li-Ion microbattery architectures." *Advanced Materials* 25.33 (2013): 4539-4543.
- [16] Coronel, Jose L., et al. "Increasing component functionality via multi-process additive manufacturing." *Micro-and Nanotechnology Sensors, Systems, and Applications IX*. Vol. 10194. International Society for Optics and Photonics, 2017.
- [17] Tibbits, Skylar. "4D printing: multi-material shape change." *Architectural Design* 84.1 (2014): 116-121.
- [18] Leigh, Simon J., et al. "A simple, low-cost conductive composite material for 3D printing of electronic sensors." *PloS one* 7.11 (2012): e49365.
- [19] Saari, Matt, et al. "Fabrication and Analysis of a Composite 3D Printed Capacitive Force Sensor." *3D Printing and Additive Manufacturing* 3.3 (2016): 136-141.
- [20] Cox, Bryan, et al. "Fiber Encapsulation Additive Manufacturing: Technology and Applications Update." *3D Printing and Additive Manufacturing* 4.2 (2017): 116-119.

- [21] Saari, Matt, et al. "Additive Manufacturing of Soft Parts from Thermoplastic Elastomers."
- [22] Xia B, Saari M, Cox B, Richer E, Krueger PS, Cohen AL, (2016). "Fiber Encapsulation Additive Manufacturing: Materials for Electrical Junction Fabrication," Solid Freeform Fabrication Symposium. 2016. Austin, TX, Austin, TX: University of Texas at Austin; 2015, 1345-1358.
- [23] Clay, Collin. Electrically conductive thermoplastic elastomers in application to additive manufacturing. Diss. Southern Methodist University, 2014.
- [24] Einstein, Albert "Investigations on the Theory of the Brownian Movement: DoverPublications. com." New York 58 (1956).
- [25] Jeffrey, Duncan James, and Andreas Acrivos. "The rheological properties of suspensions of rigid particles." *AIChE Journal* 22.3 (1976): 417-432.
- [26] Guth, Eugene, and R. Simha. "Untersuchungen über die viskosität von suspensionen und lösungen. 3. über die viskosität von kugelsuspensionen." *Colloid & Polymer Science* 74.3 (1936): 266-275.
- [27] Vand, Vladimir. "Viscosity of solutions and suspensions. I. Theory." *The Journal of Physical Chemistry* 52.2 (1948): 277-299.
- [28] Mooney, Melvin. "The viscosity of a concentrated suspension of spherical particles." *Journal of colloid science* 6.2 (1951): 162-170.
- [29] Simha, Robert. "A treatment of the viscosity of concentrated suspensions." *Journal of Applied physics* 23.9 (1952): 1020-1024.
- [30] Brinkman, H. C. "The viscosity of concentrated suspensions and solutions." *The Journal of Chemical Physics* 20.4 (1952): 571-571.

- [31] Krieger, Irvin M., and Thomas J. Dougherty. "A mechanism for non-Newtonian flow in suspensions of rigid spheres." *Transactions of the Society of Rheology* 3.1 (1959): 137-152.
- [32] Ford, T. F. "Viscosity-concentration and fluidity-concentration relationships for suspensions of spherical particles in Newtonian liquids." *The Journal of Physical Chemistry* 64.9 (1960): 1168-1174.
- [33] Thomas, David G. "Transport characteristics of suspension: VIII. A note on the viscosity of Newtonian suspensions of uniform spherical particles." *Journal of Colloid Science* 20.3 (1965): 267-277.
- [34] Batchelor, G. K. "The effect of Brownian motion on the bulk stress in a suspension of spherical particles." *Journal of fluid mechanics* 83.1 (1977): 97-117.
- [35] Quemada, D. "Rheology of concentrated disperse systems II. A model for non-Newtonian shear viscosity in steady flows." *Rheologica Acta* 17.6 (1978): 632-642.
- [36] Wildemuth, C. R., and M. C. Williams. "Viscosity of suspensions modeled with a shear-dependent maximum packing fraction." *Rheologica acta* 23.6 (1984): 627-635.
- [37] Bournonville, B., and A. Nzihou. "Rheology of non-Newtonian suspensions of fly ash: effect of concentration, yield stress and hydrodynamic interactions." *Powder technology* 128.2-3 (2002): 148-158.
- [38] Senapati, P. K., B. K. Mishra, and A. Parida. "Modeling of viscosity for power plant ash slurry at higher concentrations: Effect of solids volume fraction, particle size and hydrodynamic interactions." *Powder Technology* 197.1-2 (2010): 1-8.
- [39] Blissett, R. S., and N. A. Rowson. "An empirical model for the prediction of the viscosity of slurries of coal fly ash with varying concentration and shear rate at room temperature." *Fuel* 111 (2013): 555-563.

- [40] Kitano, T., T. Kataoka, and T. Shirota. "An empirical equation of the relative viscosity of polymer melts filled with various inorganic fillers." *Rheologica Acta* 20.2 (1981): 207-209.
- [41] Cross, M. M. "Viscosity-concentration-shear rate relations for suspensions." *Rheologica Acta* 14.5 (1975): 402-403.
- [42] Kataoka, T., et al. "Viscosity of particle filled polymer melts." *Rheologica Acta* 17.2 (1978): 149-155.
- [43] Kataoka, T., et al. "Viscous properties of calcium carbonate filled polymer melts." *Rheologica Acta* 18.5 (1979): 635-639.
- [44] Kitano, T., and T. Kataoka. "The effect of the mixing methods on viscous properties of polyethylene melts filled with fibers." *Rheologica Acta* 19.6 (1980): 753-763.
- [45] Hasegawa, Ryuichi, Yuji Aoki, and Masao Doi. "Optimum graft density for dispersing particles in polymer melts." *Macromolecules* 29.20 (1996): 6656-6662.
- [46] Lin, Li, et al. "Modified resistivity–strain behavior through the incorporation of metallic particles in conductive polymer composite fibers containing carbon nanotubes." *Polymer International* 62.1 (2013): 134-140.
- [47] García-Macías, Enrique, et al. "Micromechanics modeling of the uniaxial strain-sensing property of carbon nanotube cement-matrix composites for SHM applications." *Composite Structures* 163 (2017): 195-215.
- [48] Deng, Hua, et al. "Towards tunable resistivity–strain behavior through construction of oriented and selectively distributed conductive networks in conductive polymer composites." *Journal of Materials Chemistry A* 2.26 (2014): 10048-10058.
- [49] Zhang, Rui, Mark Baxendale, and Ton Peijs. "Universal resistivity–strain dependence of carbon nanotube/polymer composites." *Physical Review B* 76.19 (2007): 195433.

- [50] Duan, Lingyan, et al. "The resistivity–strain behavior of conductive polymer composites: stability and sensitivity." *Journal of Materials Chemistry A* 2.40 (2014): 17085-17098.
- [51] Wang, Luheng, et al. "Study on compressive resistance creep and recovery of flexible pressure sensitive material based on carbon black filled silicone rubber composite." *Sensors and Actuators A: Physical* 165.2 (2011): 207-215.
- [52] Ruschau, G. R., S. Yoshikawa, and R. E. Newnham. "Resistivities of conductive composites." *Journal of applied physics* 72.3 (1992): 953-959.
- [53] Kost, J., A. Foux, and M. Narkis. "Quantitative model relating electrical resistance, strain, and time for carbon black loaded silicone rubber." *Polymer Engineering & Science* 34.21 (1994): 1628-1634.
- [54] Yamaguchi, K., J. J. C. Busfield, and A. G. Thomas. "Electrical and mechanical behavior of filled elastomers. I. The effect of strain." *Journal of Polymer Science Part B: Polymer Physics* 41.17 (2003): 2079-2089.
- [55] Roland, C. M., and K. L. Peng. "Electrical conductivity in rubber double networks." *Rubber chemistry and technology* 64.5 (1991): 790-800.
- [56] Cho, Jae Whan, and Jun Sik Choi. "Relationship between electrical resistance and strain of carbon fibers upon loading." *Journal of applied polymer science* 77.9 (2000): 2082-2087.
- [57] Ranade, Ravi, et al. "Influence of micro-cracking on the composite resistivity of engineered cementitious composites." *Cement and Concrete Research* 58 (2014): 1-12.
- [58] Liang, Xiaoyi, et al. "Resistivity of carbon fibers/ABS resin composites." *Materials letters* 43.3 (2000): 144-147.
- [59] Aharoni, Shaul M. "Electrical resistivity of a composite of conducting particles in an insulating matrix." *Journal of Applied Physics* 43.5 (1972): 2463-2465.

- [60] Ding, Siqi, et al. "Pressure-sensitive behaviors, mechanisms and model of field assisted quantum tunneling composites." *Polymer* 113 (2017): 105-118.
- [61] Knite, Maris, et al. "Polyisoprene-carbon black nanocomposites as tensile strain and pressure sensor materials." *Sensors and Actuators A: Physical* 110.1-3 (2004): 142-149.
- [62] Panozzo, Francesco, Michele Zappalorto, and Marino Quaresimin. "Analytical model for the prediction of the piezoresistive behavior of CNT modified polymers." *Composites Part B: Engineering* 109 (2017): 53-63.
- [63] Lantada, Andrés Díaz, et al. "Quantum tunnelling composites: Characterisation and modelling to promote their applications as sensors." *Sensors and Actuators A: Physical* 164.1-2 (2010): 46-57.
- [64] Kuronuma, Yu, et al. "Electrical resistance-based strain sensing in carbon nanotube/polymer composites under tension: Analytical modeling and experiments." *Composites Science and Technology* 72.14 (2012): 1678-1682.
- [65] Bilodeau, R. Adam, et al. "Evolution of nano-junctions in piezoresistive nanostrand composites." *Composites Part B: Engineering* 72 (2015): 45-52.
- [66] Jing, X., W. Zhao, and L. Lan. "The effect of particle size on electric conducting percolation threshold in polymer/conducting particle composites." *Journal of materials science letters* 19.5 (2000): 377-379.
- [67] Zhang, Xiang-Wu, et al. "Time dependence of piezoresistance for the conductor-filled polymer composites." *Journal of Polymer Science part B: polymer physics* 38.21 (2000): 2739-2749.

- [68] Paredes-Madrid, Leonel, et al. "Underlying physics of conductive polymer composites and force sensing resistors (FSRs). A study on creep response and dynamic loading." *Materials* 10.11 (2017): 1334.
- [69] Johnson, Oliver K., et al. "Multiscale model for the extreme piezoresistivity in silicone/nickel nanostrand nanocomposites." *Metallurgical and Materials Transactions A* 42.13 (2011): 3898-3906.
- [70] Dhote, Sharvari, Kamran Behdinin, and Jia Bian. "Characterization of the Repeatability and Sensitivity of the Quantum Tunneling Composites." 2018 International Flexible Electronics Technology Conference (IFETC). IEEE, 2018.
- [71] Johnson, Oliver K., et al. "The colossal piezoresistive effect in nickel nanostrand polymer composites and a quantum tunneling model." *Computers, Materials, & Continua* 15.2 (2010): 87-112.
- [72] Koecher, Michael C., et al. "Piezoresistive in-situ strain sensing of composite laminate structures." *Composites Part B: Engineering* 69 (2015): 534-541.
- [73] Qian, Zhe, et al. "Inverse Piezoresistive Nanocomposite Sensors for Identifying Human Sitting Posture." *Sensors* 18.6 (2018): 1745.
- [74] Enelund, Mikael, et al. "Formulation and integration of the standard linear viscoelastic solid with fractional order rate laws." *International Journal of Solids and Structures* 36.16 (1999): 2417-2442.
- [75] Haffner, Benjamin, Yacine Khidas, and Olivier Pitois. "Flow and jamming of granular suspensions in foams." *Soft matter* 10.18 (2014): 3277-3283.

- [76] Lerner, Edan, Gustavo Düring, and Matthieu Wyart. "A unified framework for non-Brownian suspension flows and soft amorphous solids." *Proceedings of the National Academy of Sciences* (2012).
- [77] Mills, Pierre, and Patrick Snabre. "Apparent viscosity and particle pressure of a concentrated suspension of non-Brownian hard spheres near the jamming transition." *The European Physical Journal E* 30.3 (2009): 309.
- [78] Bertrand, Emanuel, Jerome Bibette, and Véronique Schmitt. "From shear thickening to shear-induced jamming." *Physical review E* 66.6 (2002): 060401.
- [79] Waitukaitis, Scott R., and Heinrich M. Jaeger. "Impact-activated solidification of dense suspensions via dynamic jamming fronts." *Nature* 487.7406 (2012): 205.
- [80] Cates, M. E., et al. "Jamming, force chains, and fragile matter." *Physical review letters* 81.9 (1998): 1841.
- [81] Lootens, Didier, Henri Van Damme, and Pascal Hébraud. "Giant stress fluctuations at the jamming transition." *Physical review letters* 90.17 (2003): 178301.
- [82] Haw, M. D. "Jamming, two-fluid behavior, and "self-filtration" in concentrated particulate suspensions." *Physical review letters* 92.18 (2004): 185506.
- [83] Fall, Abdoulaye, et al. "Shear thickening of cornstarch suspensions as a reentrant jamming transition." *Physical Review Letters* 100.1 (2008): 018301.
- [84] Nordstrom, Kerstin N., et al. "Microfluidic rheology of soft colloids above and below jamming." *Physical review letters* 105.17 (2010): 175701.
- [85] Boyer, François, Élisabeth Guazzelli, and Olivier Pouliquen. "Unifying suspension and granular rheology." *Physical Review Letters* 107.18 (2011): 188301.

- [86] Oh, Sangwon, et al. "Pressure-driven suspension flow near jamming." *Physical review letters* 114.8 (2015): 088301.
- [87] Holmes, Colin B., Matthias Fuchs, and Michael E. Cates. "Jamming transitions in a schematic model of suspension rheology." *EPL (Europhysics Letters)* 63.2 (2003): 240.
- [88] Chhabra, Raj P., and John Francis Richardson. *Non-Newtonian flow and applied rheology: engineering applications*. Butterworth-Heinemann, 2011.
- [89] Donev, Aleksandar. *Jammed packings of hard particles*. Diss. Princeton University, 2006.
- [90] Xia, Bin, and Paul S. Krueger. "Rheology and Applications of Particulate Composites in Additive Manufacturing." In *Proceedings of the 29th Annual International Solid Freeform Fabrication Symposium (Vol. 1345, p. 1358)*
- [91] Cohen, Adam, et al. "Additive manufacturing of active devices using dielectric, conductive and magnetic materials." U.S. Patent No. 10,254,499. 9 Apr. 2019.
- [92] Cohen, Adam, et al. "Additive manufacturing of active devices using dielectric, conductive and magnetic materials." U.S. Patent No. 10,571,642. 25 Feb. 2020.
- [93] Saari, Matt, "Design and Control of Fiber Encapsulation Additive Manufacturing" (2019). *Mechanical Engineering Research Theses and Dissertations*. 15.
- [94] Greaves, George Neville, et al. "Poisson's ratio and modern materials." *Nature materials* 10.11 (2011): 823-837.
- [95] Lakes, Roderic S. "The time-dependent Poisson's ratio of viscoelastic materials can increase or decrease." *Cell. Polym* 11.1 (1992).
- [96] Fu, Shao-Yun, et al. "Effects of particle size, particle/matrix interface adhesion and particle loading on mechanical properties of particulate-polymer composites." *Composites Part B: Engineering* 39.6 (2008): 933-961.

- [97] Grand view research. "3D Printing Market Size, Share & Trends Analysis Report By Material, By Component (Hardware, Services), By Printer Type (Desktop, Industrial), By Technology, By Software, By Application, By Vertical, And Segment Forecasts, 2020 – 2027"
- [98] Lakes, Roderic S., and Alan Wineman. "On Poisson's ratio in linearly viscoelastic solids." *Journal of Elasticity* 85.1 (2006): 45-63.
- [99] Tschoegl, Nicholas W., Wolfgang G. Knauss, and Igor Emri. "Poisson's ratio in linear viscoelasticity—a critical review." *Mechanics of Time-Dependent Materials* 6.1 (2002): 3-51.
- [100] Charpin, Laurent, and Julien Sanahuja. "Creep and relaxation Poisson's ratio: Back to the foundations of linear viscoelasticity. Application to concrete." *International Journal of Solids and Structures* 110 (2017): 2-14.
- [101] Shah, Subhash N., and David L. Lord. "Hydraulic fracturing slurry transport in horizontal pipes." *SPE drilling engineering* 5.03 (1990): 225-232.
- [102] Fangary, Y. S., et al. "The effect of fine particles on slurry transport processes." *Minerals engineering* 10.4 (1997): 427-439.
- [103] Lakshmi, KL Krupa, et al. "Effects of diffusion-thermo and thermo-diffusion on two-phase boundary layer flow past a stretching sheet with fluid-particle suspension and chemical reaction: A numerical study." *Journal of the Nigerian Mathematical Society* 35.1 (2016): 66-81.
- [104] Boger, David V. "Rheology of slurries and environmental impacts in the mining industry." *Annual review of chemical and biomolecular engineering* 4 (2013): 239-257.
- [105] Bergman, Theodore L., et al. *Introduction to heat transfer*. John Wiley & Sons, 2011.

[106] Efron, Bradley, and Charles Stein. "The jackknife estimate of variance." *The Annals of Statistics* (1981): 586-596.